DEVELOPMENT OF PHONON-MEDIATED TRANSITION-EDGE-SENSOR X-RAY DETECTORS FOR USE IN ASTRONOMY

A DISSERTATION
SUBMITTED TO THE DEPARTMENT OF PHYSICS
AND THE COMMITTEE ON GRADUATE STUDIES
OF STANFORD UNIVERSITY
IN PARTIAL FULFILLMENT OF THE REQUIREMENTS
FOR THE DEGREE OF
DOCTOR OF PHILOSOPHY

Steven W. Leman
September 2006

I certify that I have read this dissertation and that, in my opinion, it is fully adequate in scope and quality as a dissertation for the degree of Doctor of Philosophy.

Blas Cabrera Principal Adviser

I certify that I have read this dissertation and that, in my opinion, it is fully adequate in scope and quality as a dissertation for the degree of Doctor of Philosophy.

Sarah Church

I certify that I have read this dissertation and that, in my opinion, it is fully adequate in scope and quality as a dissertation for the degree of Doctor of Philosophy.

Steven Kahn

Approved for the University Committee on Graduate Studies.

Abstract

Low temperature detectors have grown in popularity over the years for a variety of reasons. The reduced thermal noise that they offer and the associated reduction in statistical fluctuations improve signal to noise. Novel material properties at low temperature such as superconductivity can be exploited. And let us not forget easier access to cryogenic techniques. For example industry made, and sold, refrigerators eliminating the need for graduate students to make their own.

In this thesis I discuss the development of a novel phonon-mediated distributed transition-edge-sensor X-ray detector which would be useful for astrophysical studies such as magnetic recombination in the solar corona, the warm-hot intergalactic medium and surveys of clusters and groups of galaxies.

The detector uses a large semiconductor absorber and Transition-Edge-Sensors (TESs) to readout the absorbed energy. Calorimetry is performed on individual photons and a partitioning of the energy between various TESs allows for position determination. Hence time varying astronomical sources can be spectroscopically studied and imaged.

I will conclude with a discussion of the detector's performance and propose a next generation detector which could make significant improvements on the design discussed in this thesis.

Preface

It seems odd to me that in 2006 I should make such a warning...

Much of this thesis assumes that the reader will have a color version. I realize that most department owned copiers and printers are black and white so I offer some apology. Fortunately, most people own color printers at home...

If someone passed on a black and white version to you, feel free to email me at swleman@yahoo.com. I keep this as a permanent address even if I check it only occasionally. I will be happy to send the original, color version in pdf format.

Acknowledgement

This section is both the most fun yet most difficult to write.

Hey Blas! Whether discussing physics, bike racing or beer you always seems able to produce time out of a busy schedule for your students. When the projects are going bad you never failed to reassure me and point out all the stuff that was going well and always proclaimed that we must be close to a success. Whenever I completely screwed something up, either due to inexperience or complete stupidity, you gently suggested what should be done to correct the problem and then it was forgotten. Cheers!

Sarah, Steve, Georgio and Daniel... Thanks so much for being on my reading committee and / or defense committee. I realize that you have many other obligations. I hope reading my thesis is not so much of a chore and provides some useful information.

Betty, you were crucial to my initial understanding of cryogenic techniques. You taught me how to use the KO-15 and whenever something went wrong you would be in lab at the drop of a hat to help out. If I was proficient in using the wirebonder, I might have never realized how generous you are with your time. I will never forget the time that you came in on a Saturday for no other reason than to help me wirebond a detector. Also you always could lend an ear for personal problems or professional career advice. Thanks also for all the cookies and bagels.

Paul, you are an interesting character. Your only real fault is that you are British but overall you are cool so that can be quickly forgiven. You were always available for lab help at a moment's notice. I appreciate all the time you spent answering questions regarding conceptual understanding of the detector. My eternal apologies

for throwing you into the chair on the cruise ship in Tokyo... Thanks also for the professional career advice.

In lab, Paul and Betty balance themselves out. When one of them thinks that a problem is dire, the other one finds a way out of it. If you are an incoming student, get to know them well...

Maria, you have become a great friend and confidant in my last year here. I truly appreciate how much you have encouraged me to chase my dreams and never get too down on myself.

Pat and Astrid, of course you guys were instrumental in most of the detector fabrication. Thanks so much for your efforts in making them and your patience in teaching me the various fabrication processes in CIS.

Pat, it is always great getting a beer with you. The coolness that you and Dawn kept after that one gin-induced night was awesome. (Ask Dawn, she likes telling the story :-[) Sometimes you find out how cool people are in the most embarrassing of ways. Fortunately, your encouragement in the pool hall didn't land me in jail, but that is a story best left known to only a few people.

Pat and T.J., you guys have become great beer brewing buds. Lots of great beer and experimentation. I think homebrewing is illegal in Japan, so if you come by we will have to drink at a bar.

Astrid, you have become a great confidant and encourager. I am forever indebted to you for you patient ear and encouragement.

Deep... what can I say that is fit for print??? Not much! :D.

Walter, thanks for encouraging and helping me to learn dancing. A true shame that you have been too busy to join me more. I hope you always keep your laces untied. One more ride on the mechanical bull before we leave!

Swag, you've become one of my best friends. Thanks for all the help dancing. I would be *a really* lousy dancer (instead of *just a* lousy dancer) without you. Sorry again for dropping you... Yikes!

Matt, you are a nut. I am never cc'ing you on an email that I don't want in Blas's inbox!!! Come to Tokyo some time... we will "KAN PAI!" in whatever language you want.

Arito, thanks for all your help (past and future) with Japanese and telling me about the culture. See you soon.

P.T. and Joey, darts were always lot of fun. I will never forget the look on your face when I told you, “I’ve got it all figured out... I bought some maps on the internet.” You were right... I almost did die!

Hey Boissicats... You have always been there for me, whatever and whenever. I don’t hear the word “family” without thinking of y’all. Wayne, thanks for all the help and fun in lab. We’ve gotta peel out in parking lots more often!

Ice cream girl... I think most of the things I will be thankful for will come in the next couple years. Thanks for encouraging me to chase this crazy dream. Every time I was flipping out and discouraged you quickly put things in perspective and kept me optimistic. Truly, this wouldn’t be happening without you. The first round is on me... see you soon.

A, you encouraged me so much and kept me on my feet whenever I was getting beaten down. I wouldn’t even have started this is it wasn’t for you. Only the best memories; always.

Invariably, many people have been left out... I owe you all a drink!

Contents

List of Tables

List of Figures

Chapter 1

Introduction

1.1 Types of Astrophysical Observations

For centuries, astrophysical objects have been studied by observing visible light both with the naked eye and through a telescope. Visible light is now understood to be electromagnetic radiation; electromagnetic radiation also includes other wavelengths (or equivalently frequencies or energies): radio, infrared, optical, ultraviolet, X-ray and gamma ray radiation. I will generically use the term light to include *all* electromagnetic radiation. Other types of radiation have been identified and studied in recent times.

Photos acknowledgments:
http://www.eurocosm.com/Application/images/telescopes/675-telescope-lg.jpg
http://www.physlink.com/News/Images/Super-Kamiokande1_lg.jpg
http://www.aldebaran.cz/bulletin/2005_16/auger_design.jpg
http://www.pparc.ac.uk/Nw/Md/Artcl/gravity.jpg

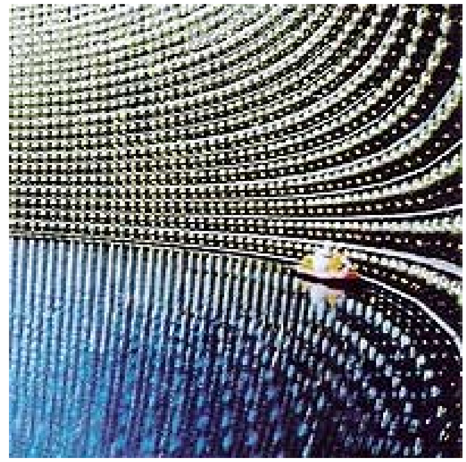

Neutrinos are a product of beta decay processes, such as nuclear fusion which occurs in the sun and can be studied at neutrino observatories such as Sudbury Neutrino Observatory and Super Kamiokande. Neutrinos interact with either deuterium or pure water (in SNO and Super-K respectively) or electrons. In both detectors, the reactions produce high energy charged particles which move faster than the speed of light of the detector's medium. Cherenkov radiation is produced as the high energy charged particles slow down. This Cherenkov radiation is then absorbed in large photomultiplier tubes on the edge of the detector.

Cosmic rays are charged particles, such as protons and alpha particles, produced by astrophysical sources and are observed at observatories such as Pierre Auger Cosmic Ray Observatory. High energy cosmic rays interact with nuclei in the earth's upper atmosphere. There is a subsequent cascade that produces billions of particles which eventually fall on a large (up to ten square mile) area of earth. These high energy particles can be detected with a Cherenkov detector. Additionally, the cosmic rays excite atmospheric nitrogen which then fluoresces at ultraviolet energies and can be detected.

Gravitational radiation has been detected indirectly through the slowing of binary pulsar rotation. Future direct observation of gravitational radiation will (hopefully) be performed on earth by the Laser Interferometer Gravitational-Wave Observatory (LIGO), and in space by the Laser Interferometer Space Antenna (LISA). Both function by measuring the effect that a passing gravitational wave has on local space-time. LIGO will be able to measure a change of 10^{-18} meters over its 4 kilometer laser beam length. The discovery will further validate Einstein's general theory of relativity.

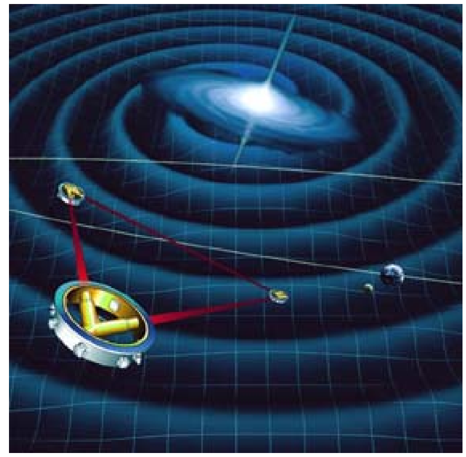

1.2 Light Detector Technologies

Observations of light still dominate astrophysical studies. Light detection methods have a long history and are becoming increasingly advanced as new technologies are developed. I will briefly discuss a few light detecting technologies to lead into the reasons for a new design discussed in this thesis.

Photos acknowledgments:
http://artfiles.art.com/images/-/Fabrizio-Cacciatore/Close-Up-of-Womans-Eye-Photographic-Print-C11979061.jpeg
http://xray.optics.rochester.edu:8080/workgroups/cml/opt307/spr04/jidong/film.jpg
http://www.kolumbus.fi/michael.fletcher/pmt_1.jpg
http://www.watch.impress.co.jp/av/docs/20030729/ccd.jpg
http://www.yale.edu/proberlab/DiffusionJunction.jpg
http://www.nist.gov/public_affairs/images/05EEEL020_TES_Sensor_LR.jpg

The most common light detector technology is of course the eye. It has served man and woman well with good spatial resolution and color resolution ability. Unfortunately it is limited to the optical band of the electromagnetic spectra, and due to a low quantum efficiency of a few percent, requires relatively high fluxes. As an astrophysical tool, it receives a boost when the observer makes a sketch of the observation with paper and pen!

Photographic film is familiar light detection technology although it is rapidly being replaced by digital technologies. Film has excellent spatial resolution and can be made in large sheets. It is sensitive to infrared and higher energies. However, like the eye, it also has a poor quantum efficiency on order of a few percent, requiring it either observe a high flux source of have long exposure times. Long exposure times of course reduce time resolution. Film has no intrinsic energy resolving capability and requires filtering to provide color information further limiting its quantum efficiency.

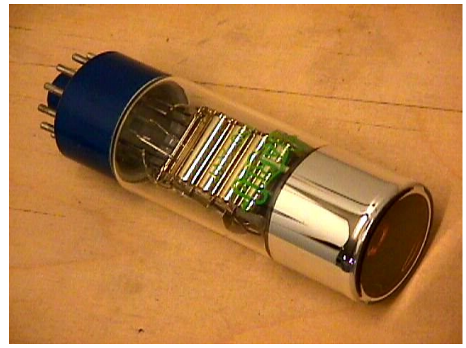

Electronic light detectors have a more recent history. Photomultiplier Tubes (PMTs) have excellent time resolution on order of picoseconds. However they also have no intrinsic energy resolving capability. Their large size, from as small as a light ball to as large as a beach ball makes them impractical as imaging devices. The larger sized PMTs being used in experiments such as SNO and Super-K and the Pierre Auger Observatory to detect Cherenkov radiation.

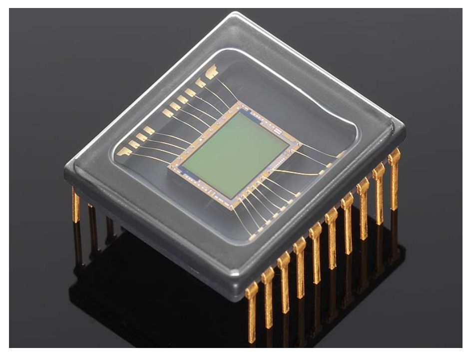

Semiconductor devices such as the Charge-Coupled Device (CCD) and Complementary Metal Oxide Semiconductor (CMOS) based detectors are common in today's digital cameras and have been used in numerous astronomy detectors. They can be fabricated into imaging arrays with tens of mega-pixels. Absorbed light must be at or above semiconductor physics energy scales, on order of an electron volt (infrared light); quantum efficiency can be over 90% for high energy photons. Unfortunately, both CCDs and CMOS devices also lack intrinsic energy resolution. Also time resolution is generally limited to tens of microsecond. When light is absorbed in a CCD, it produces at least one electron-hole pair. The charge can be confined by electrodes during the exposure. Afterwards, it can be transported to readout gates and processed.

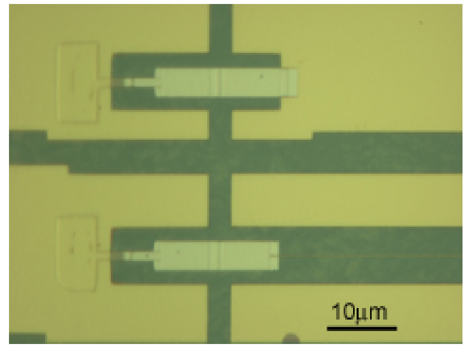

Superconducting devices are the newest types of light detectors. Superconducting Tunneling Junctions (STJs) are able to resolve individual photons and have excellent energy resolution and time resolution. They also can be fabricated into arrays, but a uniform magnetic field is required for their operation; researchers are working on increasing array size. Their operation is similar to that of a CCD. However, they benefit from the reduced quantization energy of the superconducting gap, roughly three orders of magnitude lower than the semiconducting gap in CCDs. This reduced quantization energy increases the number of charge carriers and decreased the associated statistical fluctuations.

Transition Edge Sensors (TESs) are another type of superconducting detector and are used in the work described in this thesis. The also have excellent energy and time resolution. Their advantage over STJs is that they are not as sensitive to a magnetic field environment.

1.3 Scientific Motivation

Photos acknowledgments:
http://imagine.gsfc.nasa.gov/Images/news/chandra_big.gif
http://imagine.gsfc.nasa.gov/Images/satellites/xmm.jpg
http://space.mit.edu/HETG/Reports/HETG_Report_Jul02_files/image002.jpg
http://www.spacedaily.com/images/galaxy-cluster-abell1689-desk-1280.jpg
http://map.gsfc.nasa.gov/m_ig/060913/CMB_ILC_Map75.jpg
Scientific motivation acknowledgment:
"Cryogenic detectors for wide-field soft X-ray surveys" proposal submitted by Steven Deiker 22Apr2005.

Astrophysical X-ray observations have already begun with Chandra X-ray Observatory and XMM-Newton Observatory. Both observatories provide high spatial resolution, high statistics images of supernova remnants, isolated galaxies and galaxy clusters. Also both have dispersive grating spectrometers to perform spectroscopy. Their insights guide current theoretical astrophysics.

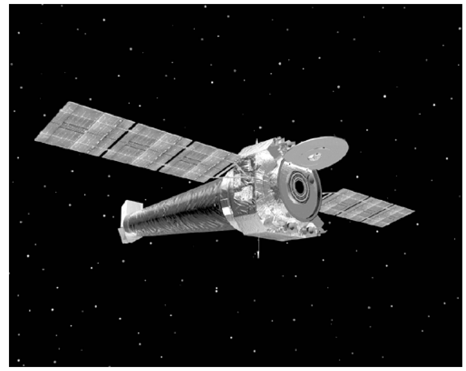

Unfortunately, a cryogenic leak led to the failure of Astro E-2's XRS detector which would have made it the first cryogenic X-ray observatory in space. Astro E-2's XRS detector had a $\Delta E/E = 6$ eV at 6 keV and a 6×6 imaging array allowing for simultaneous spectroscopy and imaging. All three of these missions are 'pointed' X-ray observatories designed to observe individual sources over some small angular extent.

However, there are issues more suited to a broader angle survey missions which still require high spectral and position resolution. Studies of the Warm Hot Intergalactic Medium (WHIM) and a survey of galaxy clusters are two examples. For these survey missions, the telescopes etendue ($A \times \Omega$ where A is the detector's area and Ω is the telescopes field of view) is of importance. In this thesis we will be developing a large area detector suitable for such studies.

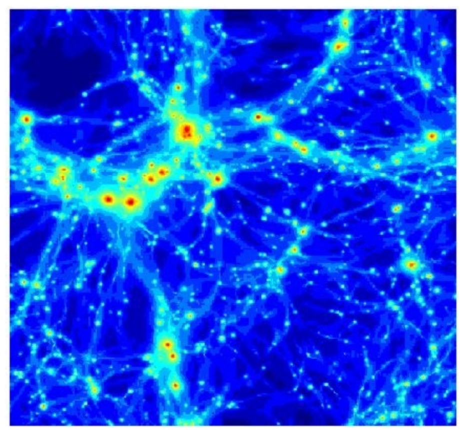

It is believed that on order of one half of baryonic matter lies in a low density ($\sim 2 - 6 \times 10^{-6}$ cm^{-3}) intergalactic medium comprised mostly of ionized hydrogen. Recent high resolution large-area simulations of galaxy formation [1] and nuclear-synthesis theories of element production [2] both however suggest its existence. The electron temperature is believed to be $\sim 2 - 4 \times 10^6$ K ensuring that the medium is ionized; being ionized, it will not absorb at its characteristic lines. However, bremsstrahlung radiation is produced as the charged particles deflect off of one another. Bremsstrahlung radiation has a continuous spectra but the WHIM is expected to have a peak around 0.1 keV; unfortunately, it will be quite faint.

The emission line from ionized oxygen could provide a solution due to its relatively high population and the associated discrete line. A detector with high energy resolution is required to distinguish the oxygen line from the diffuse foreground and background. Redshifting would allow the WHIM mapping to be performed in three dimensions; high spectral resolution is necessary to obtain fine resolution in the radial direction. Background rates from a diffuse background have been calculated and predict a 0.59 A counts s^{-1} keV^{-1} count rate. Similarly, a count rate from the desired oxygen line is calculated to be 0.0024 A counts s^{-1} keV^{-1}. The signal to noise ratio is roughly $5.6\times\sqrt{At\Delta E}$ where t is the observation time in units of 10^7 s and ΔE is the energy bin width in units of eV. It is necessary to produce a detector with large area A of roughly 10 cm^2.

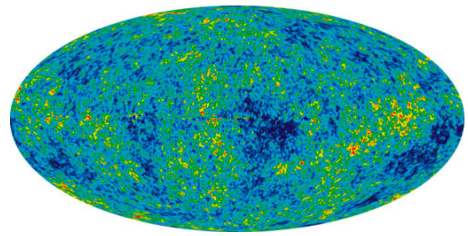

Recent observations of the cosmic microwave background by the Wilkinson Microwave Anisotropy Probe (WMAP) have shown that roughly 70% of the universe is comprised of *dark energy* [3]. Numerous theories have been presented to explain this dark energy, yet observational astrophysics is not presently able to distinguish between them. Improved measurements of $H(a)$, where H is the Hubble constant and a is the universe scale factor, are necessary.

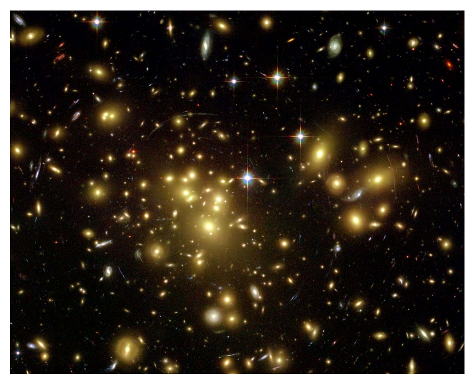

Growth of structure, particularly related to clusters of galaxies, provide an excellent study of $H(a)$. This growth of structure correlates with galaxy cluster mass which correlates with temperature and luminosity. X-ray surveys are good at measuring this temperature and luminosity. An analysis similar to that shown in the previous WHIM discussion shows that a large area detector would be able to provide good measurement of the Fe_L line features, which in turn, are good measures of temperature. In fact the requirments for a galaxy cluster survey are less restrictive than that for a WHIM mission. In the rest of this thesis, I discuss work towards developing detectors for these missions.

1.4 Thesis Layout

This thesis starts in Chapter 2 by explaining basic detector principles. The concept of calorimetry and the energy systems in the detector are laid out. TES operation and fundamental energy resolution is discussed.

Phonon and TES simulations are discussed in Chapters 2 and 3 respectively. They are critical in discussions on energy resolution (see Chapter 8) and phase separation (see Appendix B) respectively.

Experimental work begins with Chapter 5 and progresses through Chapters 6 and 7 as more sophisticated detectors are developed.

In Chapter 8 I discuss possible reasons for the degradation in the detector's energy resolution along with a simple solution.

In Chapter 9 I provide a sketch of a next generation detector. It could lead to improved energy resolution even over that proposed in Chapter 8.

The variations in the refrigerator's base stage temperature could lead to energy resolution degradation and is discussed in Appendix A. The effect is quantified and ultimately ruled out.

Another consideration for energy degradation is phase separation in the TES and is discussed in Appendix B. Ultimately this was also ruled out but the study took on a life of its own. The discussion does not fit naturally into the context of the rest of the thesis and was put into the appendix. However the reader should not consider this to lessen its importance. This phase-separation study was performed in two dimensions while previous studies in our group were restricted to one dimension. We notice that in two dimensions that phase separation is not suppressed along the current flow direction. It is however avoided in the direction perpendicular to current flow.

Appendix C contains software that I wrote for the National Instrument PCI-6115 data acquisition card.

Chapter 2

Basic Detector Design Considerations

2.1 Calorimetry

The basic concept behind making energy measurements is simple. Many people reading this thesis will have performed calorimetry experiments in high school.

Assuming that we have some energy source (E) that we want to measure, we just need an absorber, with heat capacity (C), to collect the energy and a thermometer to read out the temperature change $\Delta T = E/C$, where I have assumed the thermometer has negligible heat capacity (see Figure 2.1).

For our detectors the concept is fundamentally similar but the difference is noteworthy. Our detector has a silicon or germanium absorber. These are coupled to tungsten Transition-Edge-Sensor (TES) thermometers. X-rays are absorbed in the silicon or germanium absorber via the photoelectric effect and therefore produce a photoelectron. This photoelectron is generally high energy and moving faster than the crystal's speed of sound. This electron then rapidly scatters off nearby electrons producing a cascade of high energy electrons. This cascade process ceases when the electrons have an energy characteristic of condensed matter processes on order of a few electron volts. In silicon, the average energy required to produce an electron-hole pair is 3.81 eV [4]. In a process analogous to Cherenkov radiation, the electron-hole pairs emit athermal phonons until their velocity is less than or equal to the speed of sound [5] at which point their gap energy ∼1.2 eV dominates. These athermal phonons are then either absorbed into the TES or escape to the environment. Since the phonons are athermal, the crystals heat capacity does not contribute to the energy resolution. Instead, the heat capacity of the TES is relevant. We can exploit this effect and make large area absorbers despite their increased mass.

2.2 Negative Electrothermal-Feedback Transition-Edge-Sensors

Superconductors exhibit the remarkable property of passing limited, non-varying electric current without any resistance [6, 7, 8]. The transition between the superconducting and ohmic states can be tuned during the fabrication process [9] and the transition occurs over a few millikelvin temperature change. While the transition is fairly sharp, it is continuous. Therefore, the transition can be used as a very sensitive thermometer. Figure 2.2 shows a plot of resistance versus temperature for a tungsten TES that we are presently using in our X-ray detector endeavor.

There are two issues of temperature regulation that must be addressed. The first issue is keeping the TES stable in its superconducting to normal transition. Second, after absorbing the X-ray energy, the TES must be cooled to relax the detector in order to prepare it for the next event. Voltage biasing (see Figure 2.3) the TES satisfies both of these requirements [10]. The $P = V^2/R$ Joule heating associated with any resistive device provides a convenient electrothermal feedback (ETF) mechanism that keeps the TES temperature stable. As energy is absorbed in the TES electron system, the TES temperature increases and therefore the resistance increases. Since the device is voltage biased, the increased resistance reduces the current and there is a corresponding reduction in Joule heating.

Due to the phonon coupling between the substrate and the TES, there is an

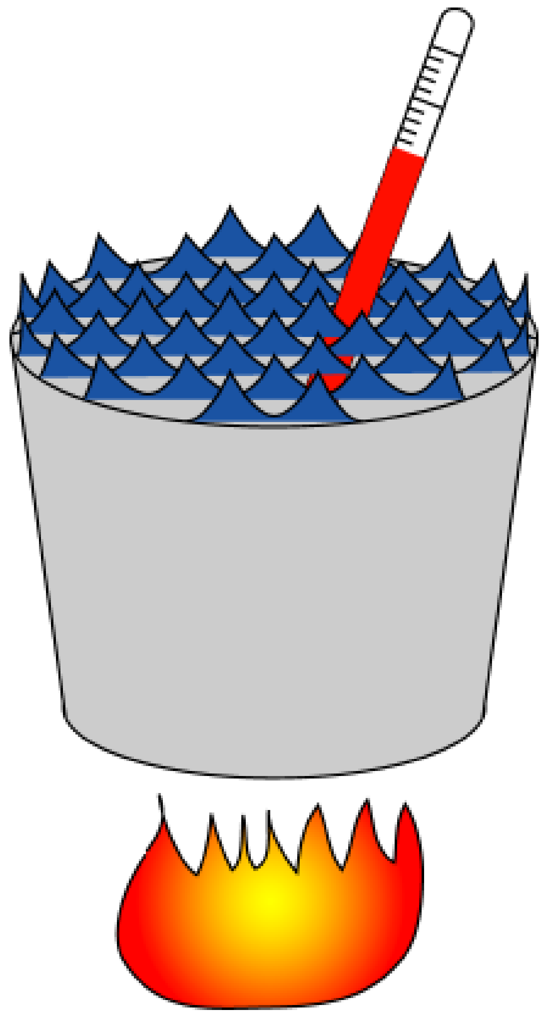

Figure 2.1: Basic Calorimetry involved an energy source (E), absorber with heat capacity (C) and thermometer. The thermometer reads a temperature change $\Delta T = E/C$.

associated phonon noise in the TES. In our devices, $\alpha/n \gg 1$ and $T_c^n \gg T_s^n$, where

$$\alpha = \frac{T_o}{R_o}\frac{dR}{dT}$$

is a unit-less measure of the steepness of the transition, T_c is the superconducting temperature of the TES, T_s is the silicon substrate temperature, and n is an integer related to the coupling between the TES electron and phonon systems, which significantly simplifies the formula that describes this noise (and is discussed shortly). We operate in an electron-phonon decoupled regime [11], where $n = 5$. These statistical variations in electron-phonon coupling lead to a fundamental noise source (a more detailed analysis on the sources of this noise will be given in Section 5.3.1, but the following approximation is close enough for this discussion) which can be characterized by the energy resolution whose energy full-width-half-maximum given by

$$\Delta E_{FWHM} = 2\sqrt{2\ln 2}\sqrt{4k_bT_cE_{sat}\sqrt{\frac{n}{2}}} \text{ [12]}, \tag{2.1}$$

where k_b is the Boltzmann constant, and E_{sat} is the detector saturation energy. Unfortunately, even the best detectors are not quite able to reach this limit. Colleagues in the field have been battling position dependence in absorbers and so called "excess noise" in the TES itself [13, 14, 15, 16, 17, 18]. Given a T_c ~90 mK and saturation energy of ~6 keV we would expect ΔE_{FWHM} ~1.3 eV.

While Equation 2.1 represents a fundamental noise source that afflicts any TES based detector, it is not the dominant noise source in our detectors. It is important to consider however, since it will help to motivate some aspects of our detector design.

2.2.1 TES resistance measurements and SQUIDS

Since the TES is voltage biased, we only need to measure the current through the TES to determine its resistance. Furthermore, ETF not only provides temperature regulations, but the reduction in Joule heating can be integrated over time to give the total energy E that was absorbed in the TES electron system, without any free

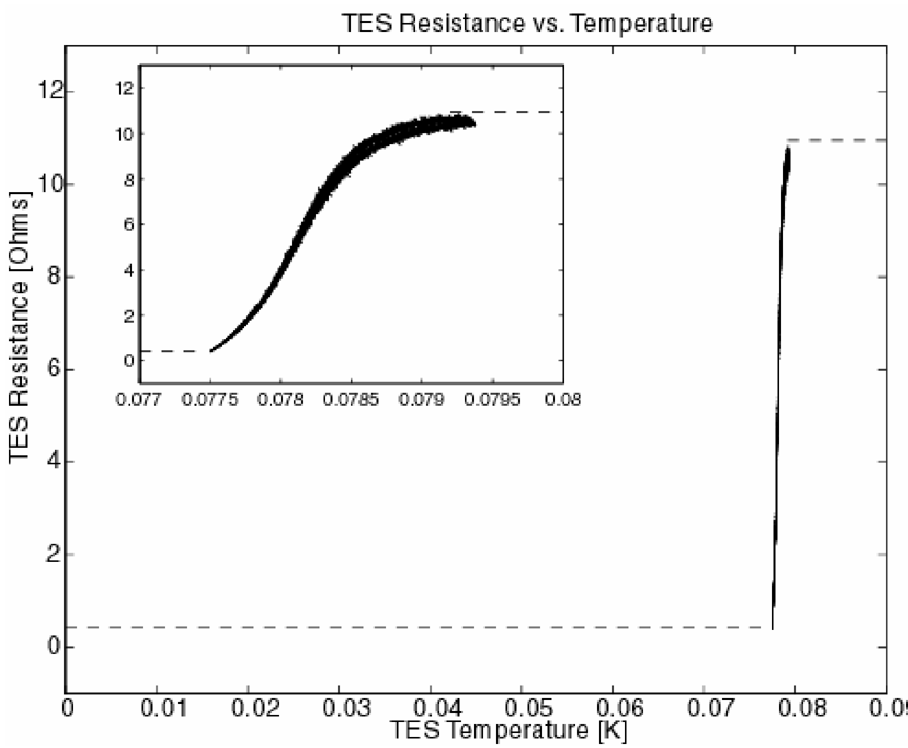

Figure 2.2: TES superconducting transition. The main graph shows the sharpness of the transition. The inset shows a close up of the transition. This measurement was performed on a TES biased with high current density. See reference [19] for a description of this scheme.

parameters [10] :

$$E = \int \Delta P_{ETF} dt = V_{bias} \int \Delta I dt \ .$$

In practice we never need to make an actual measurement on the TES's temperature or resistance. We do, however, need to know the biasing voltage and quiescent current through the TES. We use Superconducting QUantum Interference Device (SQUID) amplifiers as low-noise, low-impedance preamplifiers to measure the current through the TES. We inductively couple each TES to a SQUID array [20], and operate the SQUID array in a flux-locked loop (see Figure 2.3).When current biased, the SQUID has a periodic response to the magnetic flux which passes through it. The op-amp detects any voltage change across the SQUID (due to the changing magnetic flux) and adjusts the current through the feedback coil to eliminate the current change. This changing current can be measured as a voltage change across the feedback resistor; the absolute value of current cannot however be measured. This SQUID feedback circuit linearizes the SQUID response. In our setup the SQUIDs, fabricated at the National Institute of Standards and Technology at Boulder, are operated at 1.4 K.

Finally, like all amplifiers, the SQUID amplifier system has an associated bandwidth. Our SQUID amplifier system has roughly a 1 MHz bandwidth which is more than sufficient to track the pulse *decay* time ($\sim 10-100\mu s$) of the X-ray events in our detectors. It should be noted however that the time constant $\tau = L/R_{TES}$ given by the SQUID input coil inductance ($L = 250$ nH) and the TES resistance ($R_{TES} \sim 1\ \Omega$). The $\sim 1\ \mu$s time constant imposed by both the SQUID electronics and L/R time constant are both similar in magnitude and limits our ability to accurately determine the pulse *rise* time.

2.3 Detector Design

X-rays are absorbed in a silicon absorber, generating a photoelectron. This photoelectron cascades, producing a shower of electron-hole pairs. These electron-hole pairs rapidly shed phonons until their velocity is less than the speed of sound in the crystal. Then the electron-hole pairs diffuse until they either recombine or are

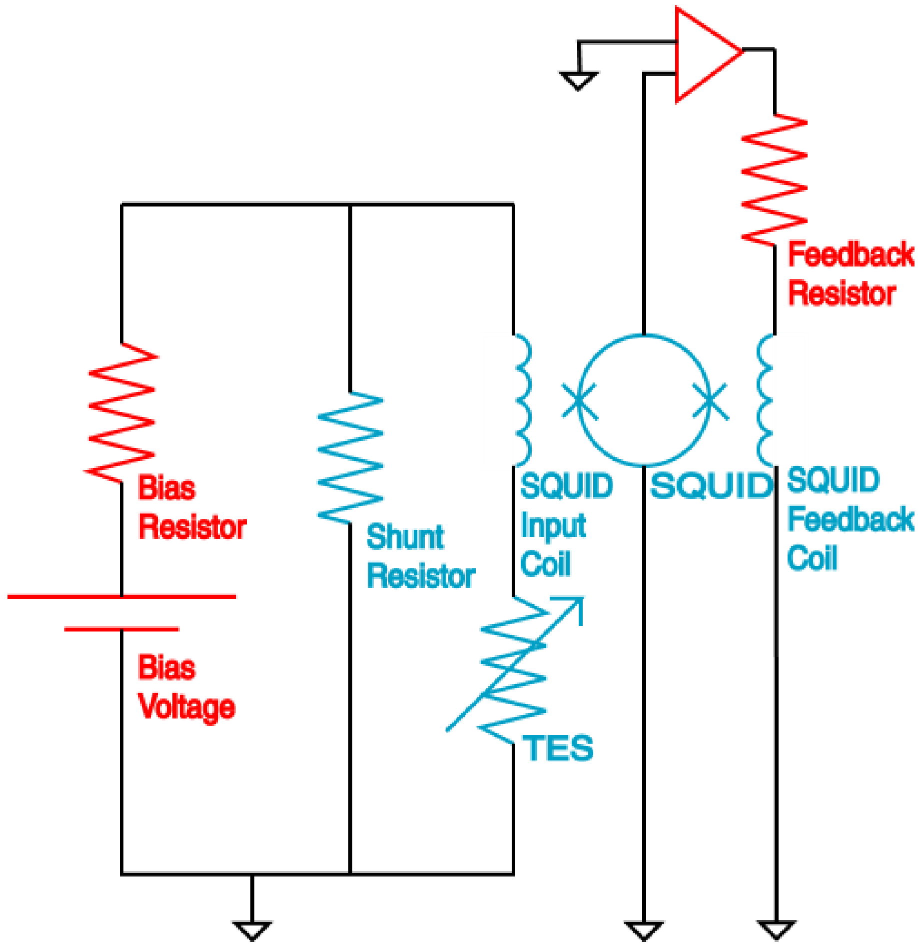

Figure 2.3: TES with SQUID amplifier and SQUID feedback circuit. The bias voltage source and bias resistor effectively produce a current supply as the bias resistor is much larger than either the shunt resistor or TES resistance. The shunt resistor is much smaller than the TES operating resistance which voltage biases the TES. When current biased, the SQUID has a periodic response to the magnetic flux which passes through it. The op-amp detects any voltage change across the SQUID (due to the changing magnetic flux) and adjusts the current through the feedback coil to eliminate the current change. This changing current can be measured as a voltage change across the feedback resistor; the absolute value of current cannot however be measured. This SQUID feedback circuit linearizes the SQUID response. Red elements are at room temperature whereas blue elements are at cryogenic temperatures.

trapped on impurities. As they recombine then they will release their gap energy as phonons. If however, they are trapped on impurities then the energy is effectively lost [21, 22, 23]. Statistical variations in this lost energy can have quite a detrimental effect on energy resolution. Either way, phonons are generated and propagate quasi-diffusively throughout the crystal. There is some probability of phonons transmitting through the silicon-tungsten interface and being absorbed in the W electron system. Phonons that fail to be absorbed into the W electron system on their first attempt will either be absorbed on a subsequent attempt or eventually escape to the environment. When absorbed, the temperature of the TES increases.

2.4 Position Measurements

2.4.1 1-d Position Measurements

Measuring where the X-ray initially was absorbed in the crystal can be made by placing more than one TES on the crystal surface and analyzing how the detected energy is partitioned between the TESs.

Figure 2.4 shows a simplest case, in which we place two TESs on the surface and can resolve the incident X-ray position in one dimension.

Figure 2.5 shows a slightly more complicated extension of the previous design, in which the blue (yellow) TESs are wired in parallel and hence function as a single TES. This scheme allows the detector's position response to be linearized. Also, by spreading the TESs across the surface, they more readily absorb phonon energy, thus decreasing the energy that escapes to the environment and reducing the dead-time in the detector.

2.4.2 1-d Position Measurement Linearization

It is important that the detector's position response is single valued if it is to be used for imaging. Fortunately, the detector's position measurement can be linearized, or at least made close to linear. To demonstrate this effect, I used some simple simulations in which the phonons are generated and bounce around in a box that was 1 mm deep,

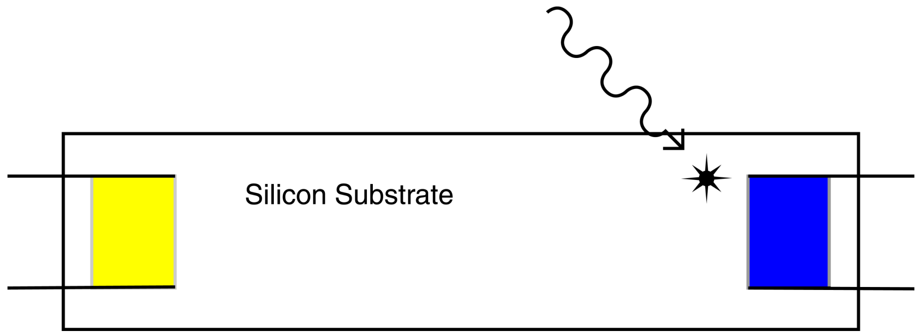

Figure 2.4: 1-d resolving detector. The position of the absorbed X-ray can be determined by analyzing how the detected energy is partitioned between the left and right TESs.

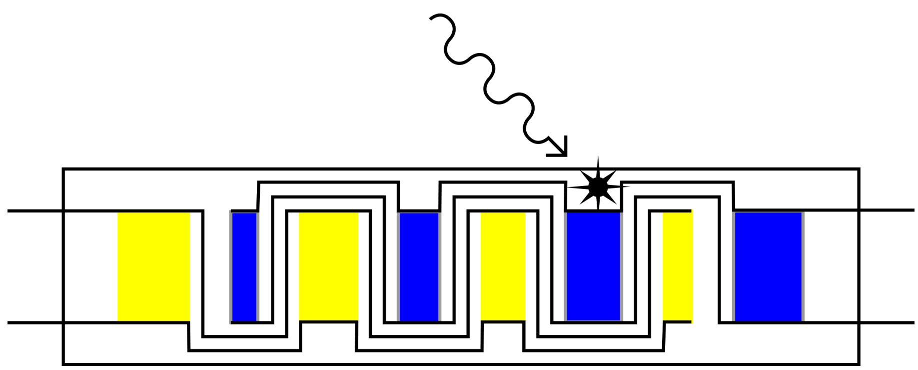

Figure 2.5: 1-d resolving detector. The position of the absorbed X-ray can be determined by analyzing how the detected energy is partitioned between the left and right TESs. The TES sizes can be adjusted to linearize the detector's position response. Additionally, spreading the TES across the surface improves the phonon-TES coupling.

4 mm wide and 0.2 mm tall. The phonons start on the bottom surface of the box, but their x and y position is randomized. The top surface of the box has 25% TES coverage and 9.25% aluminum wire coverage. The probability of being absorbed into a TES is $P_{\phi \to TES} = 0.3$. The probability of being absorbed into the aluminum wire is $P_{\phi \to Al} = 0.3$ and represents an energy loss mechanism. Phonons that were not absorbed either reflected off of the metal-deposited surface or scattered isotropically off of non-metal surfaces. For each X-ray event, 3000 phonons are generated at some random (x_n, y_n); where n refers to the particular X-ray event. Each of these phonons is given an initial, random, isotropically distributed wave vector $\overrightarrow{k}_i$. They then propagate as described above. Both the initial X-ray position and the position of the phonons absorbed in the TESs are recorded. Two thousand initial X-ray positions (x_n, y_n) are used.

The metal surface is parsed into four sections: the left-outer (green), left-inner (yellow), right-inner (blue) and right-outer section (red) (see Figure 2.6). Position can be determined by subtracting the energy collected in the left outer section from that collected in the right outer section (see Figure 2.7). Alternatively, the inner sections could be used (see Figure 2.8).

The position response can be linearized in a least-squares sense by a relatively simple process. We let $d_{1,n}$ be the outer-difference values (see Figure 2.7) and $d_{2,n}$ be the inner-difference values (see Figure 2.8). x_n is the horizontal component of the start position as stated before. It is trivial to set up Equation 2.2 and solve for the α_i (the α_i are defined indirectly through Equations 2.3 and 2.4).

$$\begin{pmatrix} d_{1,1} & d_{2,1} \\ d_{1,2} & d_{2,2} \\ d_{1,3} & d_{2,3} \\ \vdots & \vdots \\ d_{1,N} & d_{2,N} \end{pmatrix} \begin{pmatrix} \alpha_1 \\ \alpha_2 \end{pmatrix} = \begin{pmatrix} x_1 \\ x_2 \\ x_3 \\ \vdots \\ x_N \end{pmatrix} \tag{2.2}$$

The α_i are then normalized so that

$$\alpha_1 = 1$$

(which represents the outer cell). Next, the TESs in a cell are given area ratios of

$$area_{left,i} = (\alpha_i + 1)/2 \tag{2.3}$$

and

$$area_{right,i} = (\alpha_i - 1)/2. \tag{2.4}$$

The reader will notice that we are computing area ratios for four cells, yet in Equation 2.2 we only solve for two α's and hence in Equations 2.3 and 2.4 only supply two $left/right$ cell ratios. These two cell ratios can be considered appropriate for the two left most cells; the two rightmost cells are then mirror images of the two leftmost cells like shown in Figure 2.4.

Using this method for determining the relative TES sizes in each cell, a position response can be determined for this 1 $\times$ 4 detector (see Figure 2.9). The position response is simply the energy detected in the *left* cells subtracted from the energy detected in the *right* cells.

The linearization can be improved dramatically by increasing the number of cells from four to eight. In this simulation I used a box that was 8 mm wide, 8 mm deep and 0.15 mm tall. The surface coverage and absorbtion probabilities were the same as before. Again I used 2000 randomly generated initial positions, but increased the amount of phonons to 10,000 for each start event. Solving for the relative sizes of the TESs in each cell, Equation 2.2 is trivially modified to Equation 2.5.

$$\begin{pmatrix} d_{1,1} & d_{2,1} & d_{3,1} & d_{4,1} \\ d_{1,2} & d_{2,2} & d_{3,2} & d_{4,2} \\ d_{1,3} & d_{2,3} & d_{3,3} & d_{4,3} \\ \vdots & \vdots & \vdots & \vdots \\ d_{1,N} & d_{2,N} & d_{3,N} & d_{4,N} \end{pmatrix} \begin{pmatrix} \alpha_1 \\ \alpha_2 \\ \alpha_3 \\ \alpha_4 \end{pmatrix} = \begin{pmatrix} x_1 \\ x_2 \\ x_3 \\ \vdots \\ x_N \end{pmatrix} \tag{2.5}$$

The process to convert from the α_i to the relative TES sizes is the same as described after Equation 2.2. The linearization is obviously much improved (see Figure 2.10). The detector's position response remains poor however in the outer half cells. The response can be improved by masking this region and recalculating the

Figure 2.6: Cartoon of detector geometry used in a simple simulation to show that the detector's position response can be linearized. The metal surface is parsed into four sections: the left-outer (green), left-inner (yellow), right-inner (blue) and right-outer section (red).

TES size ratios (see Figure 2.11).

2.4.3 2-d Position Measurements

The extension to two dimensions follows naturally. When distributed properly, only four TESs are required to linearize the detector's position response in the x and y direction (see Figure 2.12). As discussed before (see Section 2.4.2) the position response in the outer half cells is difficult to linearize. This effect is unfortunately also seen in the 2-d case, but again a mask can be used to block off this region of the detector.

2.5 Absorber

An absorber is necessary because photons cannot be effectively absorbed into the tungsten TES. The optical depth scales like

$$\tau \sim Z^5/E_\gamma^{3.5} \quad [24],$$

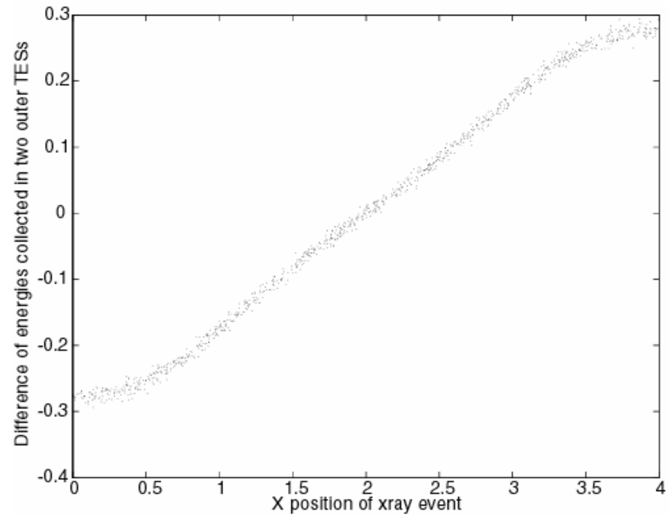

Figure 2.7: Difference in energy collected between the right-outer and left-outer TESs.

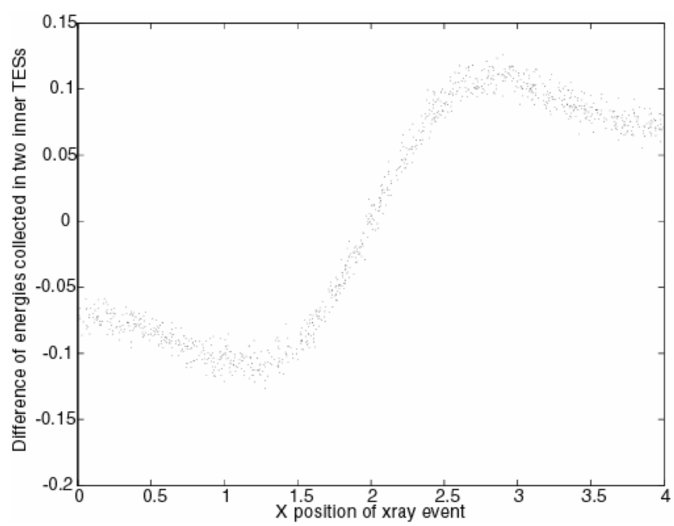

Figure 2.8: Difference in energy collected between the right-inner and left-inner TESs.

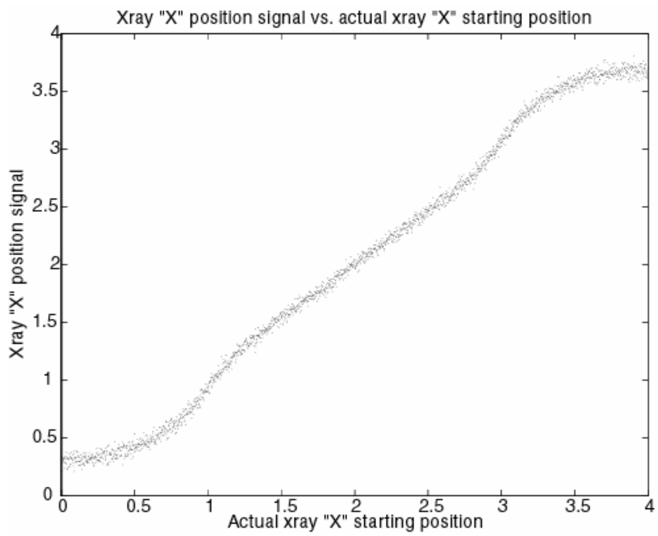

Figure 2.9: Linearized position response using the right-outer, right-inner, left-inner and left-outer TESs.

where Z is the atomic number and E_γ is the photon energy. While the high Z suggests that it would be effective, it is deposited as a thin ∼40 nm films and only ∼2.5% of X-rays would be absorbed.

Instead, a thick (∼300μm) silicon or germanium crystal can be used. X-rays of energy 2–10 keV are 99% stopped (5 'e' foldings) by 90–700 μm of silicon (see Figure 2.13). X-rays of the same energy are stopped by 3.6–200 μm of germanium (see Figure 2.14). The shorter attenuation in germanium should have advantages in reducing the detector's position dependence in the direction of absorption.

Bismuth is a popular absorber material. It is generally sandwiched with layers of high conducting metals such as copper [25]. This setup allows the absorber to rapidly thermalize before the energy is absorbed and readout by the TESs. For bismuth and other materials, the absorber's heat capacity is generally an important consideration. The lattice heat capacity per volume is given by

$$c_{v,lattice} = 234 \left(\frac{T}{\Theta_D}\right)^3 nk_b$$

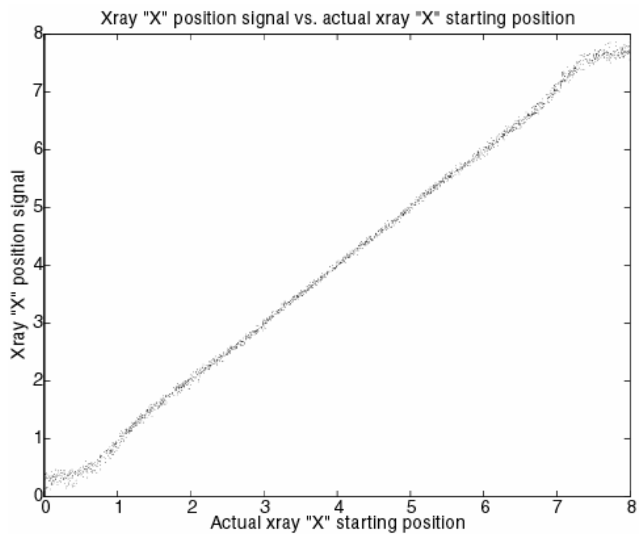

Figure 2.10: Linearized position response using eight cells.

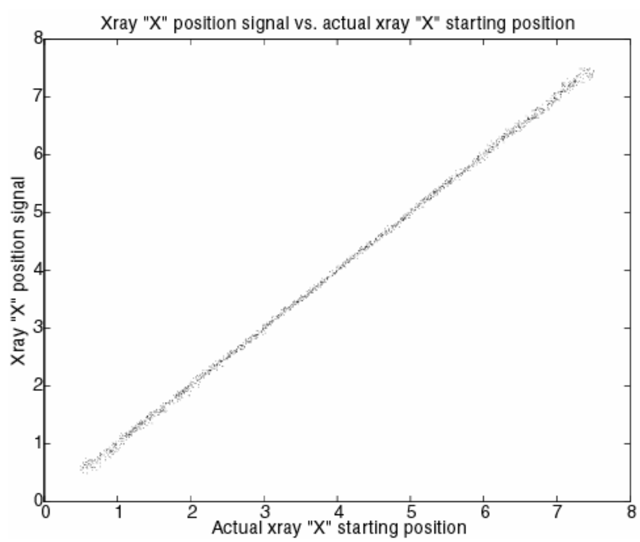

Figure 2.11: Linearized position response using eight cells but ignoring events in the outer half cells.

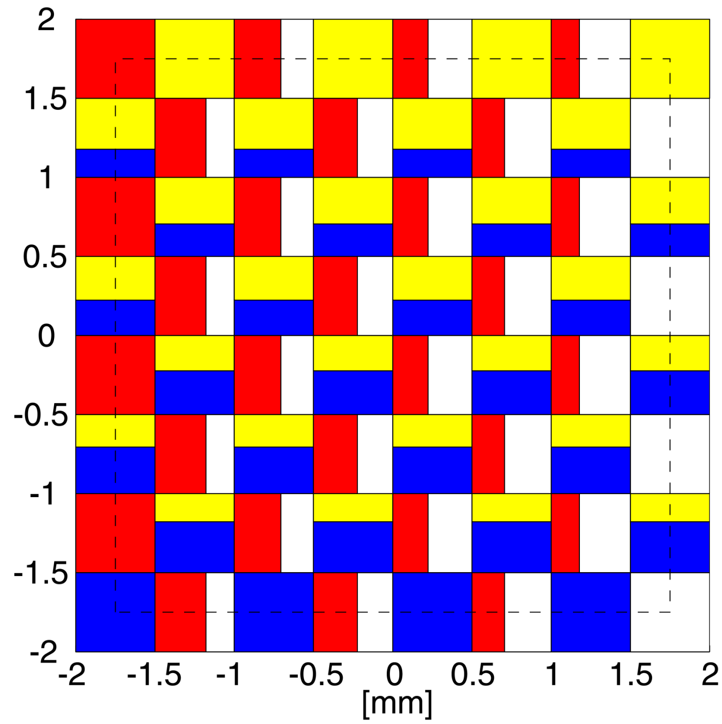

Figure 2.12: Cartoon of a four-distributed-TES detector. The correct distribution of TESs will result in a linearized position response. However, linearization is not possible for events in the outer half cell. The dashed line represents a mask that would block X-ray events from occurring in the outer half cell.

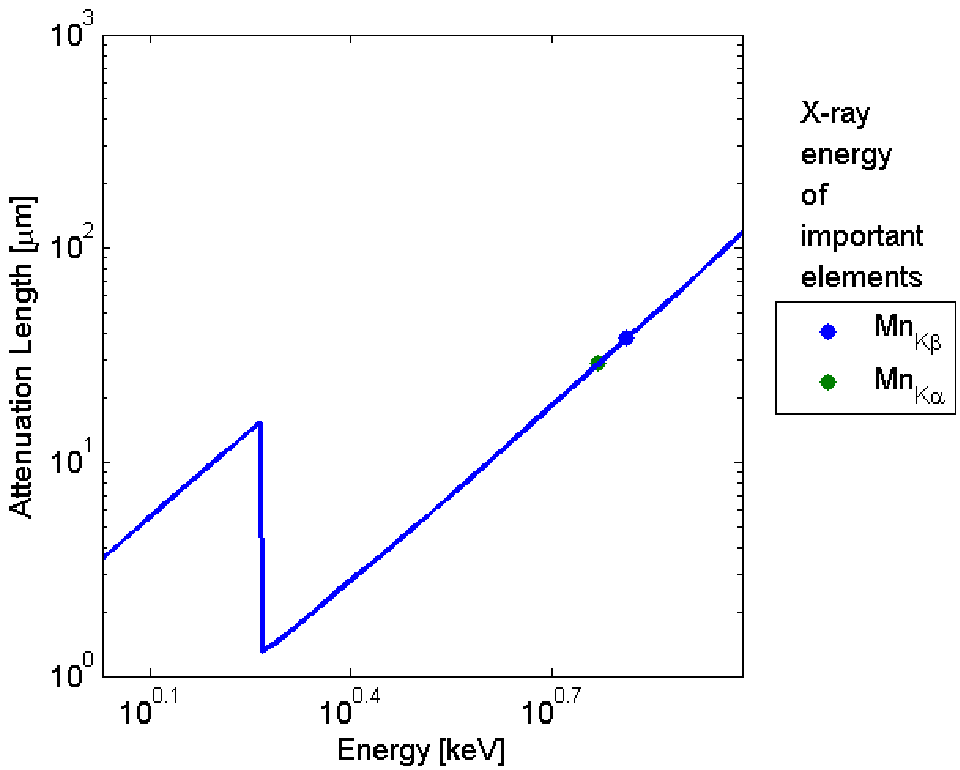

Figure 2.13: X-ray attenuation length in silicon. X-rays of energy 2–10 keV are 99% stopped (5 'e' foldings) by 90–700 μm of silicon. The dip at 1.7 eV is due to the silicon K_α and K_β photoelectric K-edge.

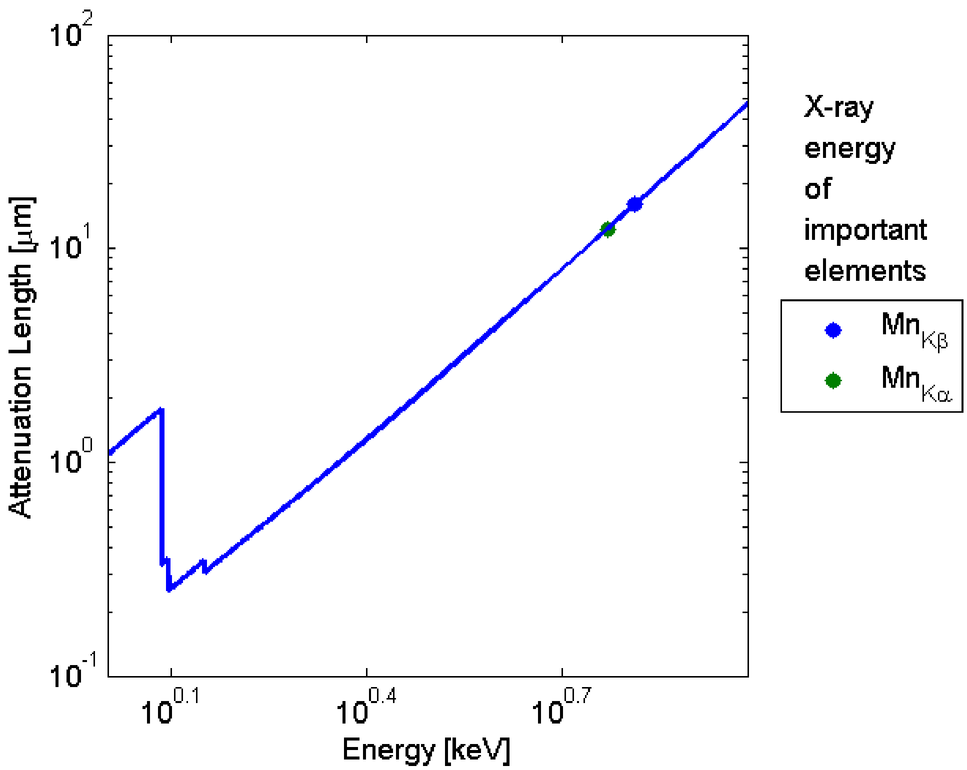

Figure 2.14: X-ray attenuation length in germanium. X-rays of energy 2–10 keV are 99% stopped (5 'e' foldings) by 3.6–200 μm of germanium. The dips at 1.2 eV is due to the germanium L_{α} and L_{β} photoelectric K-edge.

where T is the temperature, Θ_D is the Debye temperature, n is the number of atoms per volume and k_b is the Boltzmann constant [7]. I calculate the heat capacity for silicon, germanium since these are materials that we can fabricate in CIS along with bismuth. Bismuth, being a metal, also has an electronic heat capacity of

$$c_{v,electron} = \frac{\pi^2}{2}\frac{T}{\epsilon_f} n {k_b}^2$$

where ϵ_f is the Fermi energy. Quartz is another CIS compatible substrate, but it's 8.4 eV bandgap makes it less appealing than either silicon or germanium. For two reasons silicon and germanium are preferable to bismuth. First, as stated before, the phonons are athermal and therefore its heat capacity is unimportant. While bismuth is an effective absorber, its large heat capacity makes it impractical for our large absorber design.

Material	Density	Atomic Mass	Θ_D	$c_{v,lattice}$ (40 mK, 1 mm^3)	$c_{v,electron}$ (40 mK, 1 mm^3)
	g cm^{-3}	g mol^{-1}	K	keV mK^{-1}	keV mK^{-1}
Silicon	2.33	28.1	625	0.26	n/a
Germanium	5.32	72.6	360	1.2	n/a
Bismuth	9.8	209	120	21	3800

2.6 Energy Systems

The X-rays are absorbed directly into the crystal via the photoelectric effect (see Figure 2.16). This primary photoelectron's kinetic energy dominates and is on order of thousands of electron-volts. This hot electron then scatters off of nearby electrons producing a cascade of additional electrons. This process proceeds until the electrons' energies approach that of condensed matter physics which is on order of a few electron-volts. In this regime it is now appropriate to think of electron-hole pairs. Next, in a process analogous to Cherenkov radiation, the electrons scatter off of phonons, shedding phonons which are at or near the Debye frequency. This process is completed when the electron-hole pairs have a velocity at or below the velocity of sound in the crystal, at which point the gap energy dominates. At this point, these gap energy electron-hole pairs either are trapped on shallow impurity traps or recombine on surfaces. They generally do not directly recombine since silicon and germanium are indirect gap semiconductors, making it difficult to satisfy conservation of energy and momentum in a direct recombination. As the electron-hole pairs recombine on surfaces, their gap energy is released as phonons. The resulting phonons propagate quasidiffusively through the crystal due to their high frequency. Eventually they will either be absorbed by the TES's electron system or escape to the environment.

Having some of the initial electron-hole energy trapped by charge impurities would degrade the detector's energy resolution (see Section 8.1). Fortunately, this effect has been previously investigated and the traps can be filled by radiation exposure or LED flashing [21, 26, 27]. These researchers have seen mode-shifts in their detector's operation. The so called mode-1 (see Figures 2.17 and 2.18) exists immediately after cool down. In this mode there are a large number of impurity traps in the crystal. These traps energies are close to the conduction / valence bands. Therefore energy is effectively lost when the electron-hole pairs are trapped. Mode-2 exists after some period of radiation exposure. After some period, the traps are filled by the electron-hole pairs and unable to further trap charge carriers. It should be noted that the modes are distinct: as the population of mode-1 decreases, the population of mode-2 increases.

Dougherty noticed that a 4 mm$\times$2 mm$\times$300 μm silicon detector took $\sim$15 hours to shift from mode-1 to mode-2. Using an ^{241}Am source he exposed his detector to a 10 s^{-1} event rate. Furthermore, the source was mounted externally to the refrigerator allowing it to be placed and removed as he liked. Going through the numbers, we require $\sim$ 20 eV μm^{-3} exposure to neutralize the detector.

I have a much smaller detector of dimension 500 μm$\times$500 μm$\times$350 μm which will help neutralization to occur quickly. However I am using a ^{55}Fe source that exposes the detector to 5.9 keV gamma rays. The two factors (reduced size and reduced power) conspire to largely cancel out. We would expect a detector made from the same materials as Dougherty's but with size and exposure like ours to neutralize in roughly half the time ∼7–8 hours, if it contained the same amount of impurities. My setup is slightly different and the source is mounted to the detector for the duration of the run. Generally speaking, I allow the refrigerator to cool and stabilize overnight. Therefore, we might expect the detector to be neutralized before we ever operate it. Additionally, before we fully understood Dougherty's work, we used an LED flashing scheme (see Figure 2.15) that applied several orders of magnitude more energy on the detector and never saw a conclusive mode shift.

Unfortunately, the crystal that Dougherty and I used are not the same. We used test wafers from CIS that had a resistance of ∼10 Ω cm while Dougherty used higher resistance ∼8 kΩ cm crystals. Conductance in a semiconductor is caused by the motion of free electrons (in n-type crystals) or holes (in p-type crystals). An increased amount of dopants (or impurities) increases the number of electrons or holes. Assuming there is no *compensation*, in which both types of impurities are increased to reduce the resistance, the Drude model the conductance is given by

$$\sigma = \frac{ne^2\tau}{m}$$

where, n is the charge carrier density,
e is the charge quanta,
τ is an effective scattering time and,
m is the charge carrier's effective mass, which is not necessarily its mass when isolated [6].
While the Drude model is generally not applicable to a semiconductor due to the temperature dependence of charge carriers, we note the effect that charge carrier density has on conductivity.

If we further assume that the number of charge carriers increases linearly with the number of dopants then we conclude that the resistance scales like the number of impurities. An 8 kΩ cm crystal has roughly 10^{12} traps cm^{-3} trap density and our 10 Ω cm crystal contains a much higher 10^{15} traps cm^{-3} trap density [28]. We are forced to conclude that the crystal is not neutralized during cool down. Unfortunately, the details here were not fully understood until recently and it was incorrectly believed that the detector was neutralizing during cool down. I did use an LED flashing scheme to try to neutralize the crystal Its setup and effects will be discussed later.

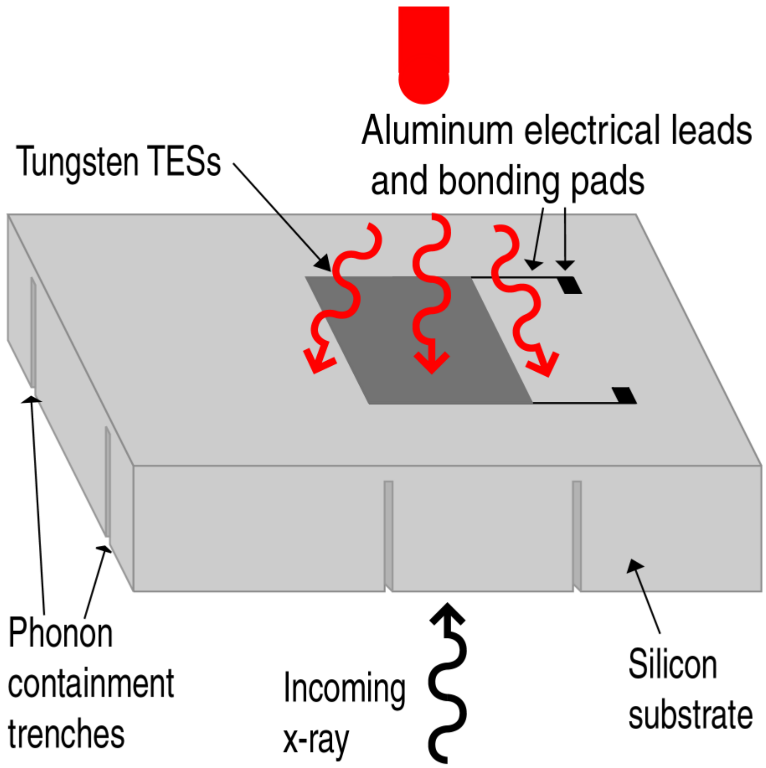

Figure 2.15: Single TES detector with LED flashing. This scheme can apply several orders of magnitude more photon energy than then X-ray source alone. However, the illumination is inefficient as much of the light is incident on the TES which does not create electron-hole pairs. When the light is absorbed properly, it must first diffuse through the bridges into the active part of the detector, slowly neutralizing layers that approach the thin $\sim 30\mu$m region where the X-rays are absorbed.

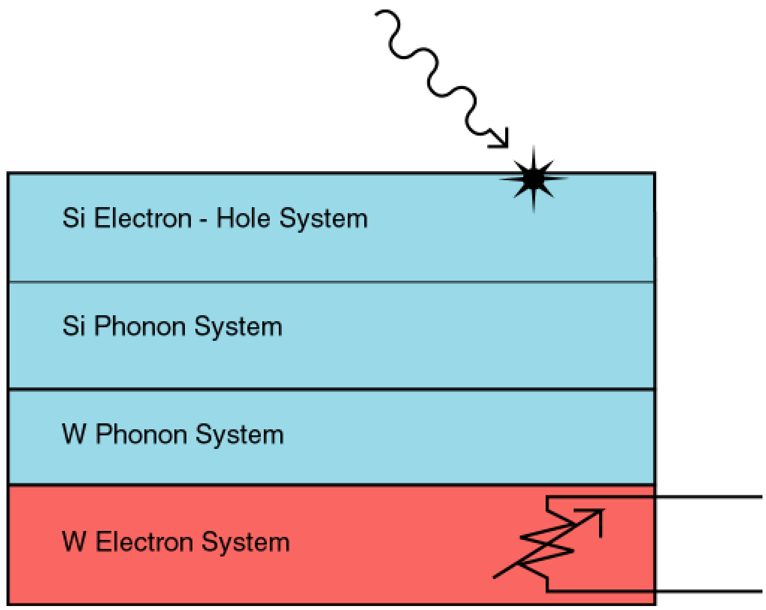

Figure 2.16: X-rays are absorbed via the photoelectric effect into the crystals electron system. They eventually emit phonons which propagate quasidiffusively through the crystal and are either absorbed by the TES's electron system or escape to the environment.

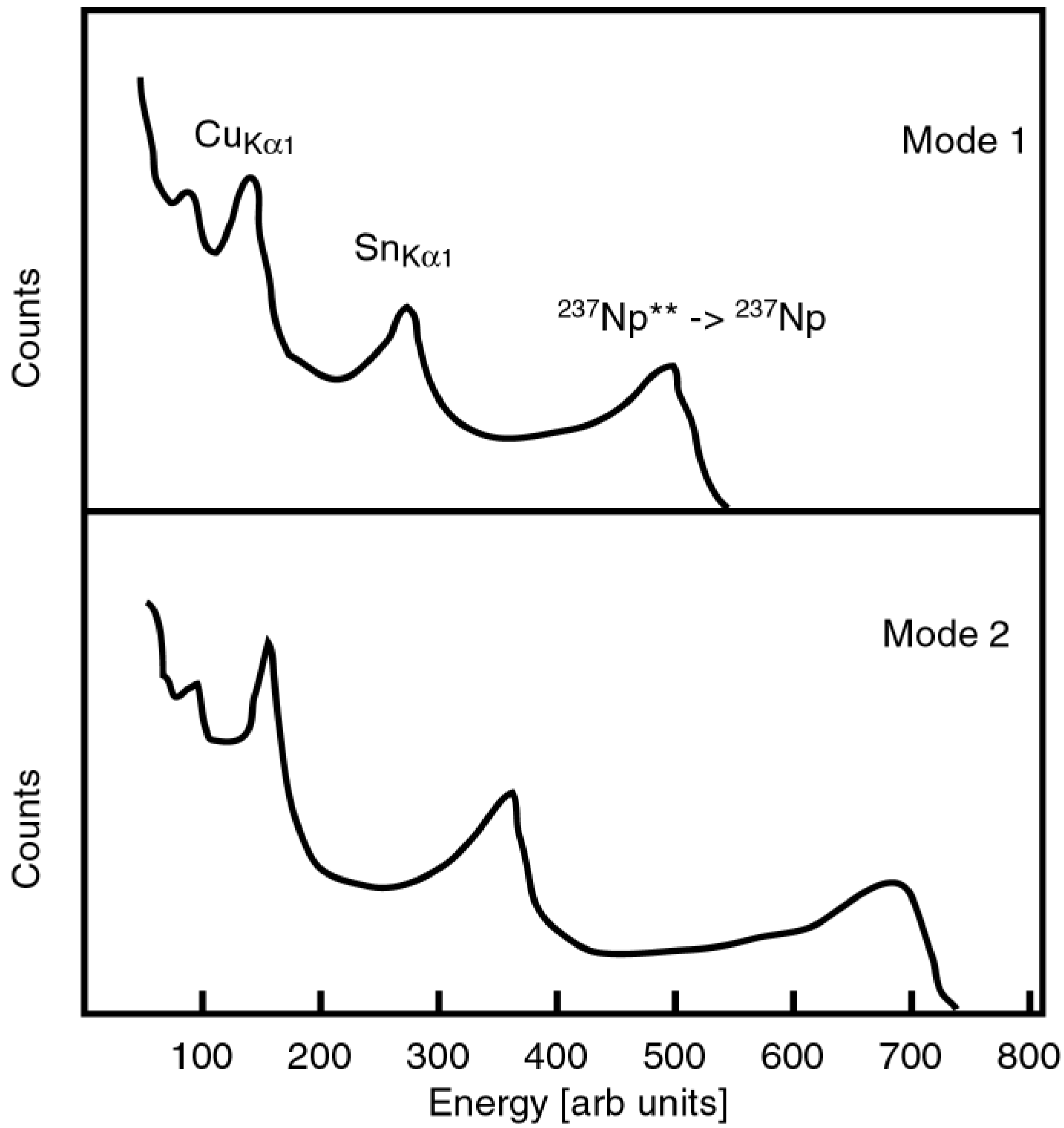

Figure 2.17: Comparison of mode-shifted-spectra for a silicon phonon detector. Shown is the spectra obtained initially after cool-down when the detector is in mode-1. After some sufficient radiation exposure, charge traps are neutralized and the detector operates in the so called mode-2. Once the traps are filled, the electron-hole pairs recombine and release their gap energy as phonons, enhancing the detector's phonon signal. Figure adapted from references [21] and [26].

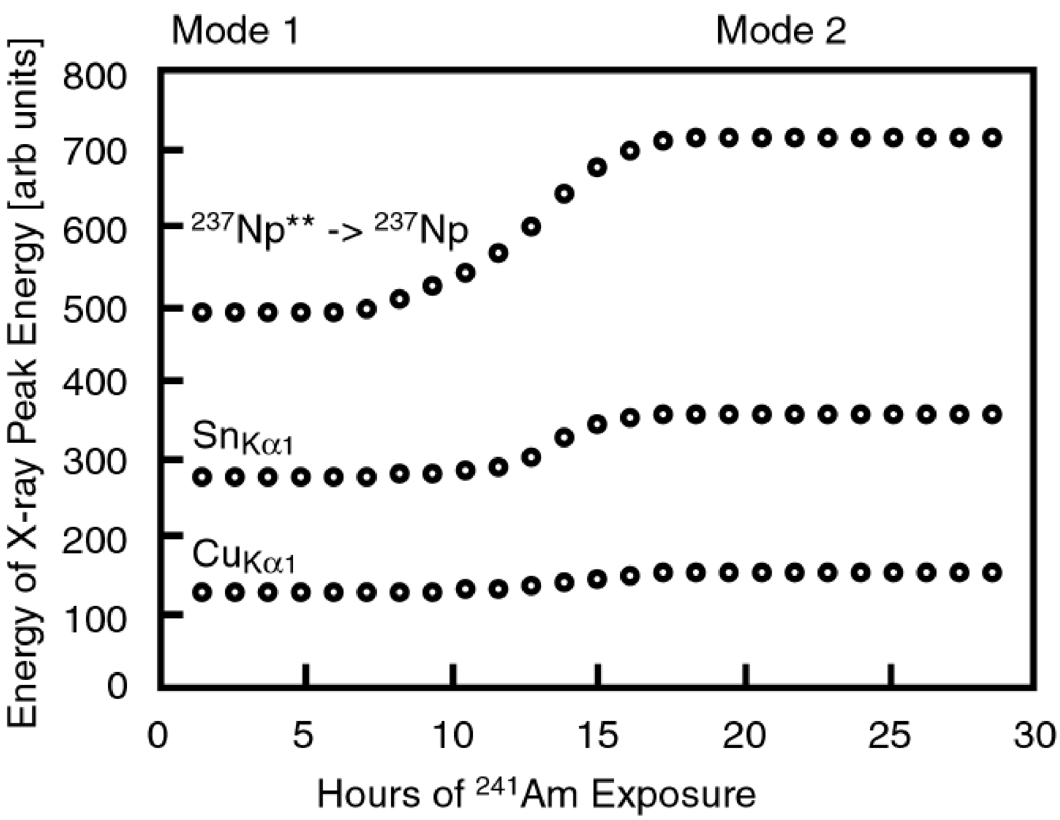

Figure 2.18: Spectra mode shift in time. Shown is the change in the detector's phonon signal as a function of ^{241}Am exposure. The detector shifts from mode-1 (empty traps) to mode-2 (filled traps). The exposure fills charge traps which then allows electron-hole pairs to recombine releasing their gap energy as phonons. Figure adapted from references [21] and [26].

Chapter 3

Phonon Simulations

3.1 Introduction

Phonon simulations provide perhaps the most valuable tool for modeling this detector. Most importantly, the simulations will allow us to determine the effect that phonons escaping to the environment will have on the energy resolution (see Section 8.2). They would also allow us to set up a position-linearization scheme as described in Section 2.4.2.

Originally, the simulations started very simply, essentially modeling billiard balls bouncing around a box. Soon, they included three different propagation modes (longitudinal, slow transverse and fast transverse), anisotropic group velocities, isotope scattering, an isotropic approximation to anharmonic decay, more complex physical modeling of the detector, frequency dependent absorption into the TES and, electron-hole diffusion before the actual phonon propagation. I will now provide an explanation of each component. Numerical constants for the simulation are not listed individually, but rather are given in Table 3.1.

3.2 Simple Modeling

Initial modeling was quite simple and was previously discussed in Section 2.4.2. Another version of modeling included sides of the boxes representing the environment,

Figure 3.1: Cartoon of detector geometry used in a simple simulation. The metal surface (the top face) is colored red.

where phonons can be lost with some probability $P_{\phi\rightarrow environment} \sim 0.1$. Phonons that were not absorbed were either reflected off of the metal surface or scattered isotropically off of non-metal surfaces.

3.3 Electron-Hole Diffusion

The simulation starts by spatially distributing the initial X-ray energy, which is done through a computational trick. I model the initial electron-hole energy as phonons of appropriate (large) energy. In one simulation version, they diffuse isotropically $\sim$ 200 μm [21] with $\sim$ 10 μm step sizes. In another version, they ballistically propagate isotropically until they are stopped by a wall. After this process, the simulation starts with very high energy phonons. To ensure they down convert below the Debye frequency before being absorbed in the TESs (as some of the charge carriers would have stopped on the metal surfaces), the TES absorption probability is set to zero above the Debye frequency (see Figure 3.10). I refer to this technique as a "trick" since the nature of the energy carriers is really the same in the simulation, I just change their isotope scattering and decay times to infinity and the propagation dynamics are isotropic. Nowhere in the simulation do I consider electrical interactions. The parameters are changed when the energy carriers are switched to phonons as discussed before.

3.4 Slowness Surfaces / Phase Velocities and Polarization Vectors

The so called slowness surfaces represent the direction dependent phonon phase velocity $\vec{v}_p = \vec{v}_p(\theta, \phi)$. In general they are given by the eigenvalue Equation 3.1.

$$\rho\omega^2\epsilon_\mu = \sum_\tau \left(\sum_{\sigma\nu} c_{\mu\sigma\nu\tau} k_\sigma k_n u \right) \epsilon_\tau, \tag{3.1}$$

where ρ is the crystal's mass density,
ω is the phonon frequency,
ϵ_μ is a component of the polarization vector ϵ,
$c_{\mu\sigma\nu\tau}$ is the elastic constant tensor and,
k_σ is a component of the phase velocity vector $\mathbf{k}$ [6].

In a cubic crystal the elastic constants are reduced to $C_{\alpha\beta} = c_{\alpha\alpha\beta\beta}$ which simplifies Equation 3.1 significantly [6]. We are left solving matrix 3.2 for its eigenvectors and eigenvalues.

$$\begin{pmatrix} C_{11}k_xk_x + C_{44}(k_yk_y + k_zk_z) & (C_{12}+C_{44})k_xk_y & (C_{12}+C_{44})k_xk_z \\ (C_{12}+C_{44})k_xk_y & C_{44}(k_xk_x + k_zk_z) + C_{11}k_yk_y & (C_{12}+C_{44})k_yk_z \\ (C_{12}+C_{44})k_xk_z & (C_{12}+C_{44})k_yk_z & C_{44}(k_xk_x + k_yk_y) + C_{11}k_zk_z \end{pmatrix} \tag{3.2}$$

The eigenvectors represent the three polarization vector directions and the three eigenvalues equal $\rho\omega^2$ for the longitudinal, slow-transverse and fast-transverse modes. The anisotropy in the cubic silicon crystal leads to the slowness surfaces being non-spherical (see Figure 3.2). The slowness surfaces are used to determine both the group velocities (Section 3.5) and also the isotope scattering rates.

3.5 Group Velocities

Phonon group velocities are found by solving

$$\vec{v}_g(\theta, \phi) = \frac{\partial \omega(\theta, \phi)}{\partial \vec{k}}.$$

The slight lack of sphericity in the slowness surfaces (see Figure 3.2) has a very dramatic effect on the transverse phonon group velocities [29, 30, 31, 32] (see Figure 3.3). The longitudinal phonon's group velocity is only mildly affected. Energy is focused in the direction of heavy banding and leads to the term "phonon focusing". The distance from the origin represents the speed that phonon energy is carried through the crystal.

The point density in the plots is misleading as the three modes are shown to be equally populated. Isotope scattering (see Section 3.6) leads to the phonon modes being populated as follows: slow-transverse (55%), fast-transverse (35%) and longitudinal (10%).

3.6 Anisotropic Isotope Scattering

Phonons scatter off mass defects in the crystal (see Figure 3.4). Additionally, they can change modes. The bulk scattering rate is given by

$$\Gamma_I = B\nu^4[s^3],$$

where ν is the phonon frequency and B is a scattering rate constant [30, 32, 33, 34, 35] (see Section 3.1). The scattering rate for individual phonons is given by

$$\gamma \sim \frac{|\vec{e}_\lambda \cdot \vec{e}_{\lambda'}|^2}{\nu_{\lambda'}^3},$$

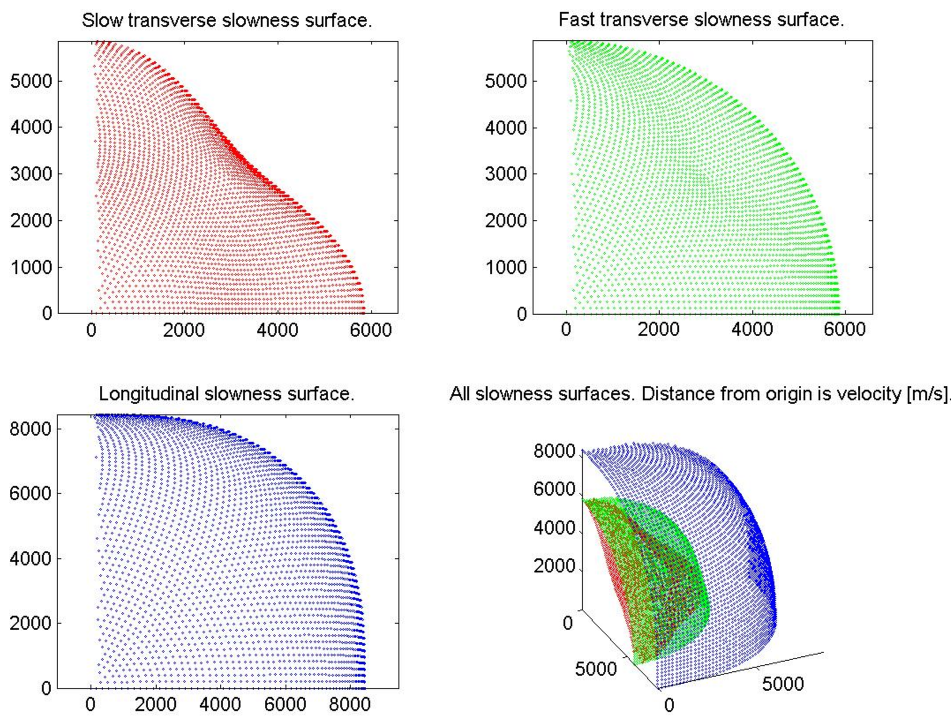

Figure 3.2: Slowness surfaces in silicon. These are found by solving for the eigenvalues in Equation 3.1. The distance from the origin represents the phase velocity speed (in m/s). Silicon's cubic crystal geometry leads to them being non-spherical. The first three plots are views from the north pole. The fourth view containing all three surfaces is offset from the north pole. In the plots all modes are equally populated, which does not reflect the actual mode populations.

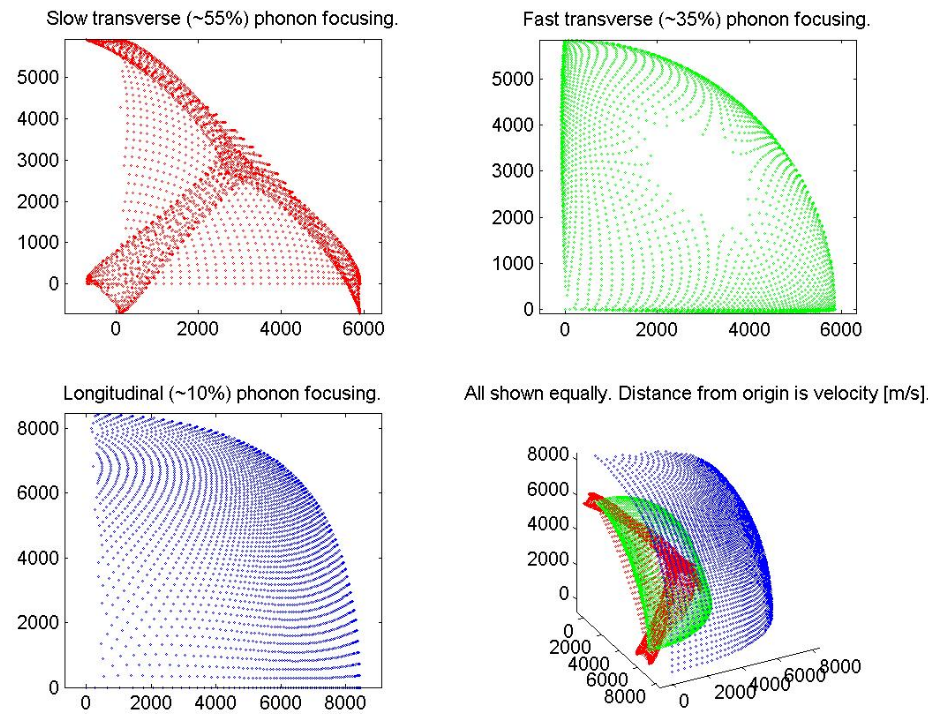

Figure 3.3: Group velocities in silicon. The slight lack of sphericity in the slowness surfaces (see Sigure 3.2) has a very dramatic effect on the transverse phonon group velocities. The longitudinal phonon group velocity is only mildly impacted. Energy is focused in the direction of heavy banding and leads to the term “phonon focusing”. The distance from the origin represents the speed that phonon energy is carried through the crystal (in m/s). In the plots all modes are equally populated, which does not reflect the actual mode populations.

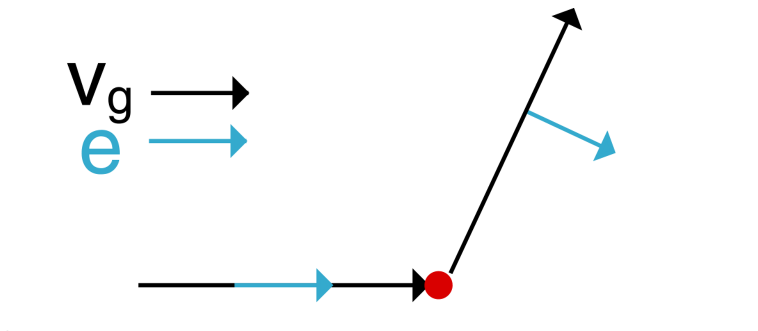

Figure 3.4: Phonons isotope scatter off mass defects in the crystal. Equation 3.6 gives the individual phonon scatter rates. $\vec{v_g}$ is the group velocity and $\vec{e}$ is the polarization vector.

where ν is the phonon frequency in Hz, $\vec{e}$ is the polarization vector, λ represents the initial phonon and λ' represents the outgoing phonon [32, 35]. It is the dot product in Equation 3.6 which allows mode mixing and the denominator which ensures the correct populations in the ratios slow-transverse (55%), fast-transverse (35%) and longitudinal (10%). After the initial anharmonic decay has settled down, isotope scattering dominates.

This process is unfortunately computationally expensive. In the future, if simulations need to be sped up, one could consider isotropic scattering for individual phonons.

3.7 Anharmonic Decay

3.7.1 General Case

Nonlinear terms in the elastic coupling constants cause a longitudinal phonon to down convert to two lower energy phonons (see Figure 3.5). The bulk decay rate is given by

$$\Gamma_A = A\nu^5[s^4],$$

where ν is the phonon frequency and A is a decay rate constant [32, 33, 34, 35] (see Section 3.1). The decay rate for transverse phonons is negligible [36]. The three body

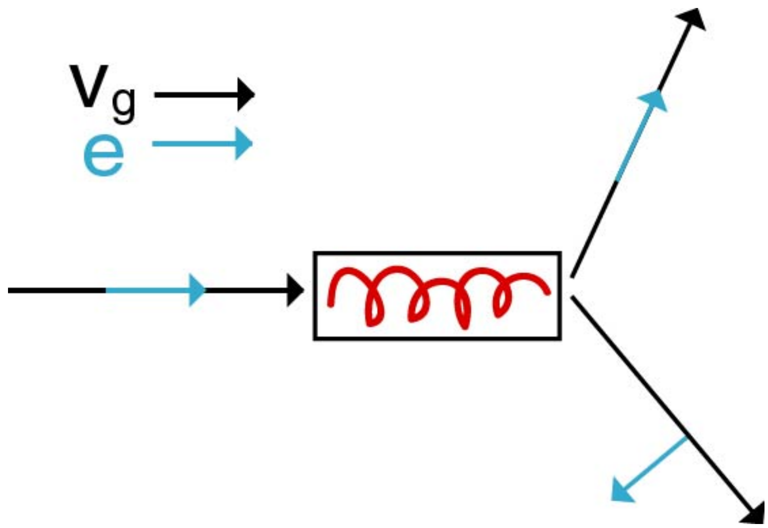

Figure 3.5: Longitudinal phonons decay due to nonlinear terms in the elastic coupling constants. $\vec{v_g}$ is the group velocity and $\vec{e}$ is the polarization vector.

problem requires that both energy and momentum are conserved. These conditions make an exact solution computationally prohibitive for large amounts of phonons.

3.7.2 Isotropic Approximation

To allow computations to proceed in a finite time, an exact solution to anharmonic decay was abandoned and an isotropic approximation is used. The energy distribution calculations are still difficult but fortunately have already been carried out [37, 38]. Once the energies have been determined, calculating the resultant scattering angles based on energy and momentum conservation is fairly straight forward. The $L \rightarrow L' + T'$ energy distribution is given by

$$\Gamma_{L\rightarrow L'+T'} \sim \frac{1}{x^2}\left(1-x^2\right)^2\left[(1+x)^2-\delta^2(1-x)^2\right]\left[1+x^2-\delta^2(1-x)^2\right]^2,$$

where $x = E_{L'}/E_L$,
$\delta = \frac{v_l}{v_t}$ and,
$\frac{\delta-1}{\delta+1} < x < 1$.

This approximation results in the outgoing phonons having an angular displacement from the initial phonon given by

$$\cos(\theta_{L'}) = \frac{1 + x^2 - \delta^2(1-x)^2}{2x},$$

$$\cos(\theta_{T'}) = \frac{1 - x^2 + \delta^2(1-x)^2}{2\delta(1-x)}.$$

The $L \to T' + T'$ energy distribution is given

$$\Gamma_{L \to T'_1 + T'_2} \sim \left(A + B\delta x - Bx^2\right)^2 + \left[Cx(\delta - x) - \frac{D}{\delta - x}\left(x - \delta - \frac{1-\delta^2}{4x}\right)\right]^2,$$

where $x = \delta \frac{E_{T'_1}}{E_L}$,
$\delta = \frac{v_l}{v_t}$,
$\frac{\delta - 1}{2} < x < \frac{\delta + 1}{2}$,
$A = \frac{1}{2}(1-\delta^2)[\beta + \lambda + (1+\delta^2)(\gamma + \mu)]$,
$B = \beta + \lambda + 2\delta^2(\gamma + \mu)$,
$C = \beta + \lambda + 2(\gamma + \mu)$ and,
$D = (1-\delta^2)(2\beta + 4\gamma + \lambda + 3\mu)$.

This approximation results in the outgoing phonons having an angular displacement from the initial phonon given by Equations 3.3 and 3.4.

$$\cos(\theta_{T'_1}) = \frac{1 - \delta^2(1-x)^2 + \delta^2 x^2}{2\delta x}, \tag{3.3}$$

$$\cos(\theta_{T'_2}) = \frac{1 - \delta^2 x^2 + \delta^2(1-x)^2}{2\delta(1-x)}. \tag{3.4}$$

Where I make the trivial substitution $x \to 1 - x$ for the second phonon.

With these closed-form energy densities and scattering angles, plots can be generated to aid understanding of these events (see Figures 3.6, 3.7, 3.8 and 3.9).

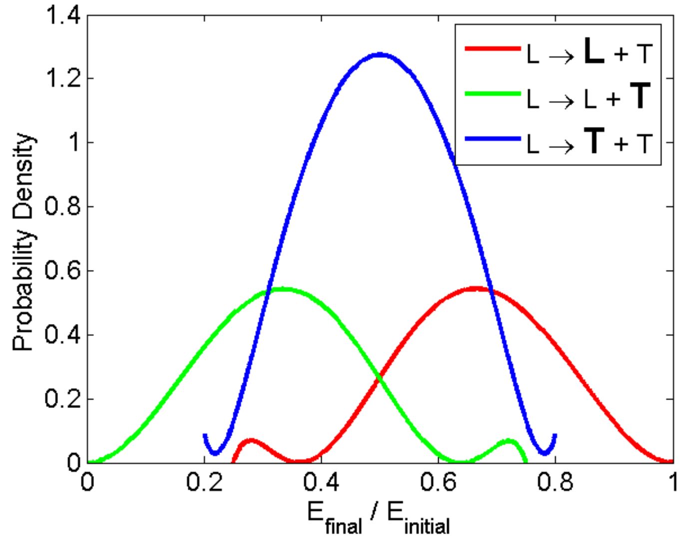

Figure 3.6: Resultant energies in longitudinal phonon decay in silicon. The two branches $L \rightarrow L + T$ and $L \rightarrow T + T$ are shown.

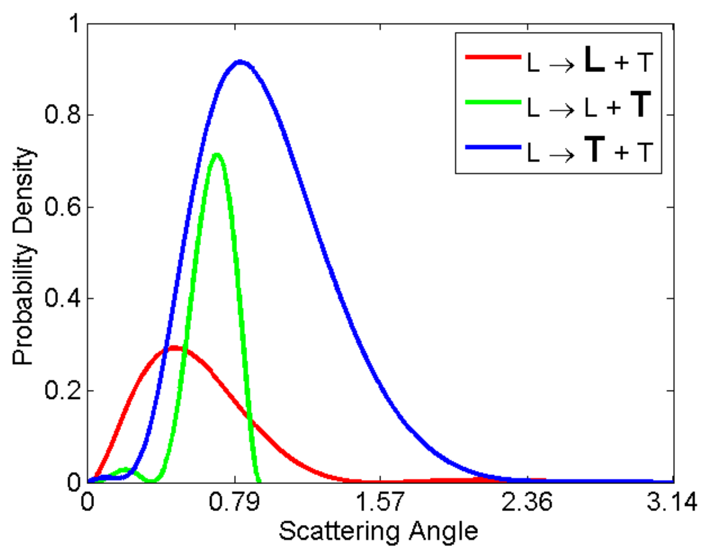

Figure 3.7: Resultant angles in longitudinal phonon decay in silicon. The two branches $L \rightarrow L + T$ and $L \rightarrow T + T$ are shown.

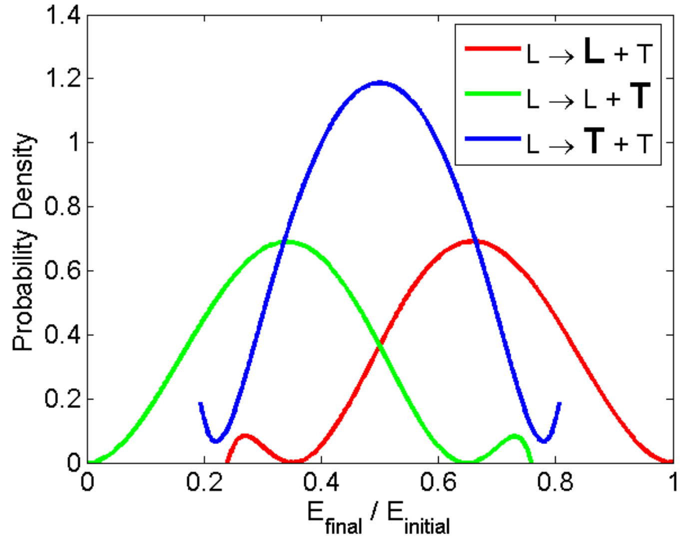

Figure 3.8: Resultant energies in longitudinal phonon decay in germanium. The two branches $L \rightarrow L + T$ and $L \rightarrow T + T$ are shown.

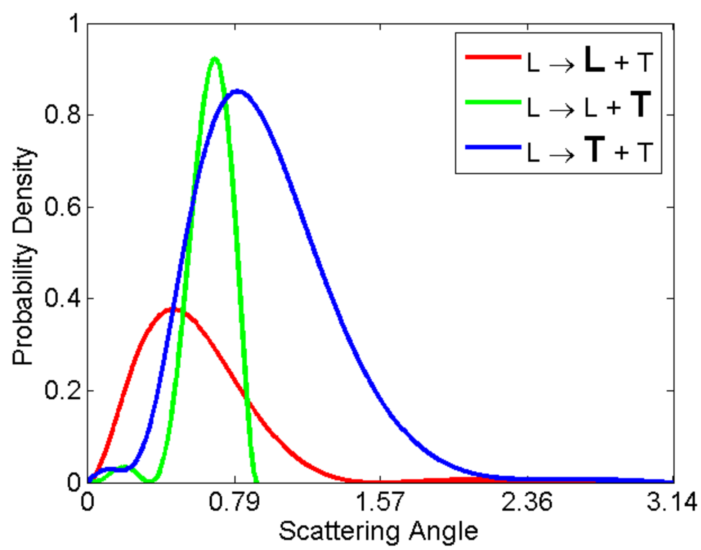

Figure 3.9: Resultant angles in longitudinal phonon decay in germanium. The two branches $L \rightarrow L + T$ and $L \rightarrow T + T$ are shown.

3.8 TES Absorption Probability

Absorption of silicon phonons into the tungsten electron system is a two step process first involving transmission of phonons through the silicon-tungsten interface and then absorption of tungsten phonons into the tungsten electron system.

3.8.1 Tungsten Phonon to Tungsten Electron Transmission

Calculating the probability of phonons being absorbed in the tungsten electron system ($\Gamma_{\phi_W \to e^-}$) is aided by knowledge of the bulk energy transport

$$P_{e^- \to substrate} = \Sigma(T^n_{electron} - T^n_{substrate}), \tag{3.5}$$

where Σ and n are constants. We operate in an electron-phonon decoupled regime [11], where $n = 5$.

In Equation 3.5 we consider the second term which goes like T^5_ϕ. We know that individual phonons have energy $E_\phi = C_\phi(T)T_\phi$ where $C_\phi(T) \sim T^3_\phi$. The power then goes like energy per phonon (E_ϕ) times a rate ($\Gamma_{\phi \to e^-}$). This scaling will satisfy the macroscopic power if the rate goes like $\Gamma_{\phi \to e^-} \sim T_\phi$ (see Figure 3.10).

As an exercise, we can consider the first term, which represents energy transport from the electron system to the phonon system. In this case, $C_{e^-}(T) \sim T_{e^-}$. It is simple enough to see that $\Gamma_{e^- \to \phi} \sim T^3_{e^-}$. The rates are then balanced when $T_\phi = T_{e^-}$. These results can also be found in the literature [39].

Furthermore, the distance that the phonon travels in the tungsten $d \sim 1/\cos(\theta)$ is also considered as phonons that spend more time in the TES should have an increased likelihood of being absorbed.

3.8.2 Silicon Phonon to Tungsten Phonon Transmission

Transmission of phonons between the silicon-tungsten interface is complicated by acoustic mismatch of the two mediums. A decent approximation could be made by including a linearly decreasing absorption probability. This approximation would

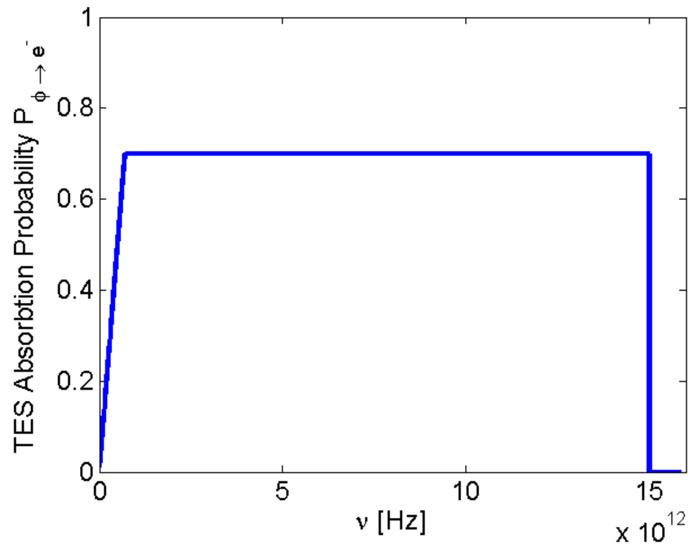

Figure 3.10: TES absorption probability density $P_{\phi \to e^-}$ for phonons that are normally incident on the TES. There is a linearly increasing probability density at low frequencies, which represents the rate of transmitting tungsten phonons into the tungsten electron system. I approximate acoustic mismatch by the maximum allowed probability (here shown to be 0.7). Also, the probability is zero above the Debye frequency as these phonons shouldn't even exist.

include two free parameters. To simplify fitting, I introduced only one free parameter, a maximum value for the absorption probability P_{max} (see Figure 3.10).

3.8.3 Absorbtion Fits

In addition to the TES absorption slope and TES absorption maximum (see Figure 3.10), I introduced a frequency independent absorption into the walls. It is physically motivated by possible down conversion at the walls; the subsequent lower energy phonons would be less likely to absorb into the TESs, and more likely to escape into the environment. So, this loss is a shortcut step. I will allow this probability to go to zero if that fit is better.

I will try to fit these three parameters using three different detector geometries. Two of the geometries are a single-pixels (see Figure 3.13) detector with 220 and

315 μm deep trenches, the third is a four-pixel detector (see Figure 3.14) with 220 μm deep trenches. For all detectors, the crystal is 350 μm thick. For the single-pixel devices there is a single 500 $\times$ 500 μm metal surface. For the four-pixel devices there are four 300 $\times$ 300 μm metal surfaces. The four pixels are separated by 50 μm trenches.

With the single-pixel devices, we can consider energy partitioning between the left and right TESs as X-rays are incident at various spots across the crystal surface. Partitioning is defined as $E_{right}/(E_{left} + E_{right})$ for X-ray events incident as far to the right on the detector before wrapping occurs (see Figure 5.17 to see this effect). Alternatively we could have defined partitioning for X-rays incident on the left side of the detector.

For the four-pixel devices we can consider the total energy absorbed when the X-ray is absorbed in the central trench region between all four of the pixels. Also we can consider energy partitioning and total energy collection when the X-ray hits one of the pixels.

Found from experiment, the 220 μm single-pixel partitioning and total energy are P_{220} =0.65 and E_{220} =49%. The 315 μm single-pixel partitioning and total energy are P_{315} =0.84 and E_{315} =73%.

The four-pixel absorption when the events are absorbed in the center of the cross is 1 keV (see Figure 3.11) in one of the four pixels. When absorbed in a one of the four pixels the energies are partitioned 2280, 490 and 235 eV (see Figure 3.12) in the TES above the absorption pixel, each of the TESs adjacent to the absorption pixel and diagonal to the absorption pixel.

The fit parameters would be adjusted by hand and simulation rerun. I satisfied enough to stop when P_{220} =0.72, E_{220} =51%, P_{315} =0.79, E_{315} =80%, the four-pixel center absorption was 710 eV per pixel and the four-pixel, pixel hit absorptions were 2263, 411 and 185 eV.

The simulation parameters that produced these results follow. The TES absorption probability was $P_{\varphi\rightarrow TES} = 10.0 \times \nu/\cos(\phi)$, where ν is the phonon frequency in THz and ϕ is the phonon incident angle. The maximum absorption probability was $P_{max} = 1.0$ and the wall loss was $P_{loss} = 0.01$. This fit is sufficient to understand the

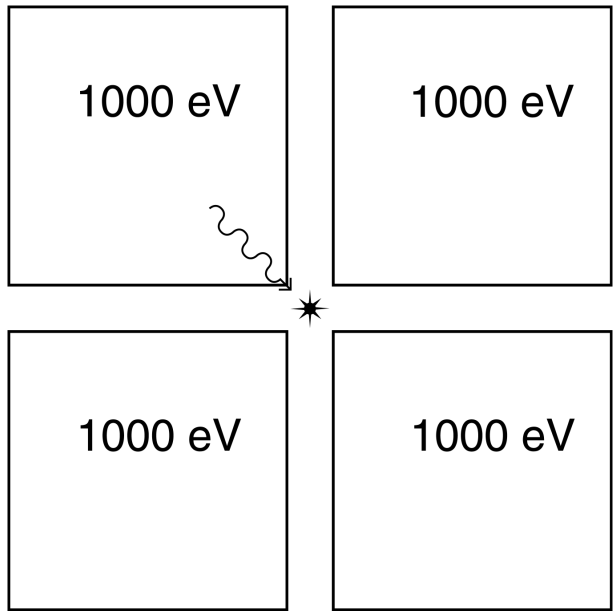

Figure 3.11: 4 pixel energy partitioning for center hits. Shown is the energy absorbed in each pixel as seen in experiment.

effects of phonon fluctuations on energy resolution.

3.9 Detector Geometry

During the course of this thesis, the detector geometry used in the simulation has evolved beyond the simple geometry discussed in Section 3.2. The detector can now be represented by any number of surfaces that are aligned parallel to the $x-y$, $y-z$ or, $z-x$ planes (see Figures 3.13 and 3.14). While any surface can have a variety a characteristics the following are generally true: 1) The outer (front, back, left and right) walls represent the environment where phonons can be lost. 2) Other green walls represent the crystal boundary where phonons are scattered according to Lambert's rule $P \sim \cos(\theta)$. 3) The red surfaces represent TESs into which phonons are absorbed or reflect with angle $\theta_{final} = \theta_{initial}$. Modeling the detector geometry with even a modest amount of surfaces (~ 50) is computationally expensive. If simulations need to be sped up, one could consider a simpler geometry with macroscopic

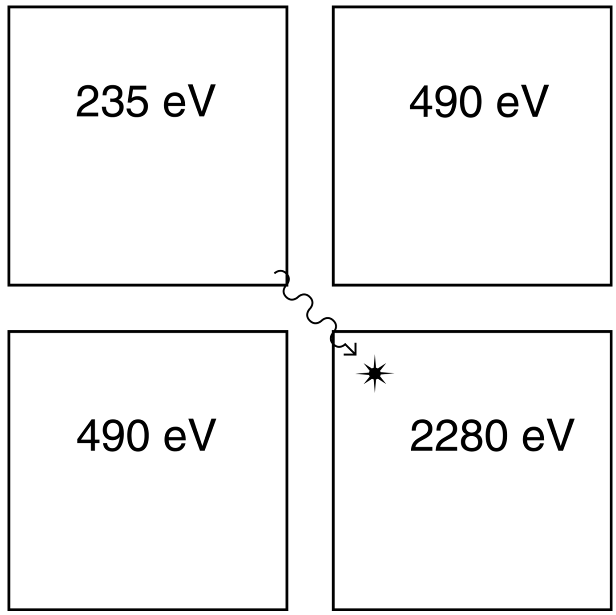

Figure 3.12: 4 pixel energy partitioning for pixel hits. Shown is the energy absorbed in each pixel as seen in experiment.

parameters controlling absorption into and scattering off of the connecting bridges.

3.10 Time Steps

It would be grossly inefficient to run all phonons with the same time step. Therefore we generate scattering times according to the distributions in Sections 3.6 and 3.7. Since the scattering and decay probabilities go like $P \sim \exp(-t/\tau)$. We can follow the procedure $y(x) = F^{-1}(x)$ where x is a uniform distributed random number and F^{-1} is the inverse of $F = \int P(t)dt$ [40]. The result is the randomly generated scattering time and is given by

$$t_{scatter} = -ln(x)/\Gamma.$$

Of course this scattering time has to be compared with the time that the phonon will take to interact with a surface and the event that occurs soonest will be chosen for each individual phonon. If it is determined to be a scattering or decay then it must

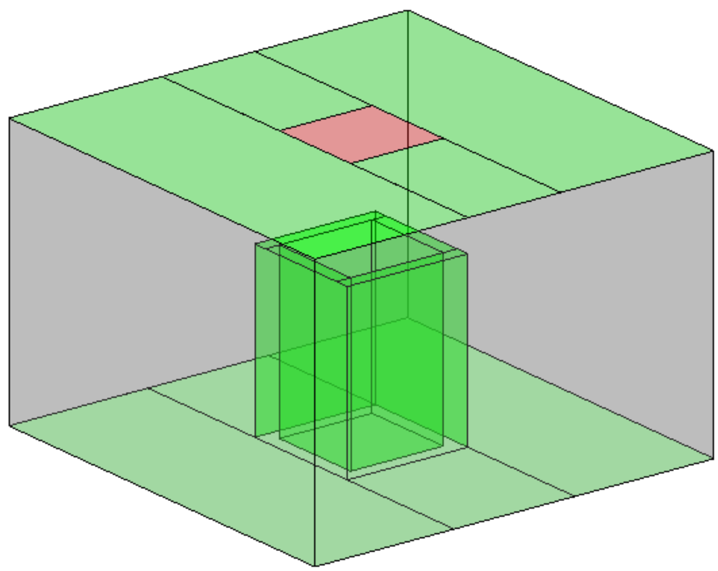

Figure 3.13: Single-pixel simulated detector geometry. The axes are *not* equal; this view in which the z-axis is stretched is an aid in seeing the detector features. The green walls scatter phonons. The outer walls represent the environment into which phonons are lost. The red surfaces represent TESs into which phonons are either absorbed or reflect. Absorption position is recorded and in analysis the red surface can be parsed into however many individual TESs that we desire (usually four in this case). Notice also the trenches which help to confine phonons to an area where they can be absorbed by the TESs.

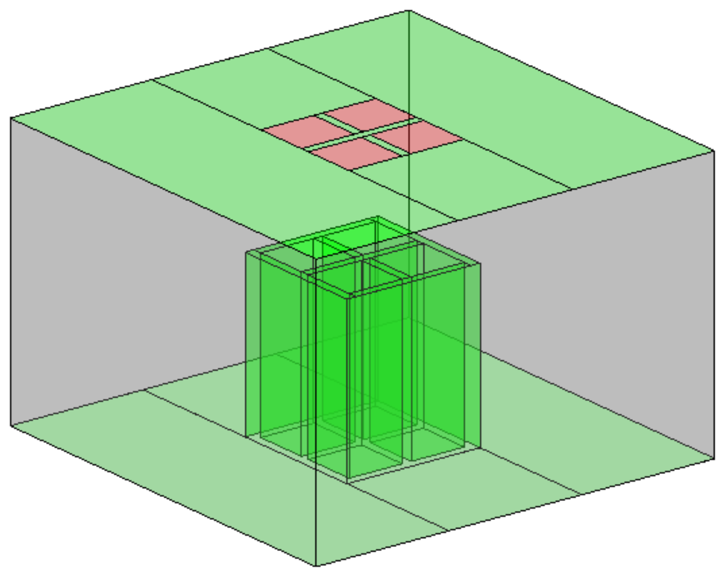

Figure 3.14: Four-pixel simulated detector geometry. The axes are *not* equal; this view in which the z-axis is stretched is an aid in seeing the detector features. The green walls scatter phonons. The outer walls represent the environment into which phonons are lost. The red surfaces represent TESs into which phonons are either absorbed or reflect. Absorption position is recorded and in analysis the red surface can be parsed into however many individual TESs that we desire (usually one in this case). Notice also the trenches which help to confine phonons to an area where they can be absorbed by the TESs.

Table 3.1: Numerical Constants for Phonon Simulations

Parameter Description	Symbol	Units	Silicon	Germanium	Reference
Isotope Scatter Rate	(B)	[s^3]	2.43×10^{-42}	3.67×10^{-41}	[37]
Anharmonic Decay Rate	(A)	[s^4]	7.41×10^{-56}	6.43×10^{-55}	[37]
Longitudinal Velocity	(v_l)	[m/s]	9000	5310	[37]
Transverse Velocity	(v_t)	[m/s]	5400	3250	[37]
Decay Rate Constant	(β)		-0.429	-0.732	[37]
Decay Rate Constant	(γ)		-0.945	-0.708	[37]
Decay Rate Constant	(λ)		0.524	0.376	[37]
Decay Rate Constant	(ν)		0.680	0.561	[37]
Density	(ρ)	[g/cm^3]	2.33	5.32	[37]
Decaying Ratio $\frac{L \to L+T}{\textit{All Longitudinal Decays}}$			0.204	0.260	[37]
Lattice Constant	(C_{11})		1.66	1.29	[7]
Lattice Constant	(C_{12})		0.64	0.48	[7]
Lattice Constant	(C_{44})		0.80	0.67	[7]
Debye Frequency	(ν_D)	[1/s]	1.5×10^{13}	0.864×10^{13}	[7]
Electron-Hole Energy		[eV]	1.17	0.75	[7]
Mean Electron-Hole Creation Energy		[eV]	3.81	2.96	[4]

be determined which event occurs based on their relative, frequency dependent rates.

3.11 Numerical Constants for Phonon Simulations

Table 3.11 lists numerous constants that are used in the phonon simulations. They define the propagation dynamics, scattering and decay rates and energy carrier statistics.

Chapter 4

Transition Edge Sensor Simulations

4.1 Introduction

Compared to the phonon simulations, the TES simulations are a bit simpler; most of the physical processes that make up the simulation are likely to be more obvious to the reader. There are, however, tricky numerical issues in solving for the TES voltages. A description of the process follows, and a flowchart (see Figure 4.1) helps in understanding it.

First, the biasing conditions have to be determined. When the TES is run as an X-ray detector the bias voltage is held constant. However, so called IbIs (bias current vs. sensor current) characterization plots are often studied in which the bias current is swept through a range of values. The biasing circuitry and TES resistance $R = R(T, I)$, where T is temperature and I is current across some physical extent are modeled. The TES electron temperature is affected by three processes: 1) Joule heating warms the TES; 2) Conduction into the substrate cools it; 3) Diffusion through the TES spreads heat. It is of course the goal to run the simulation quickly and accurately.

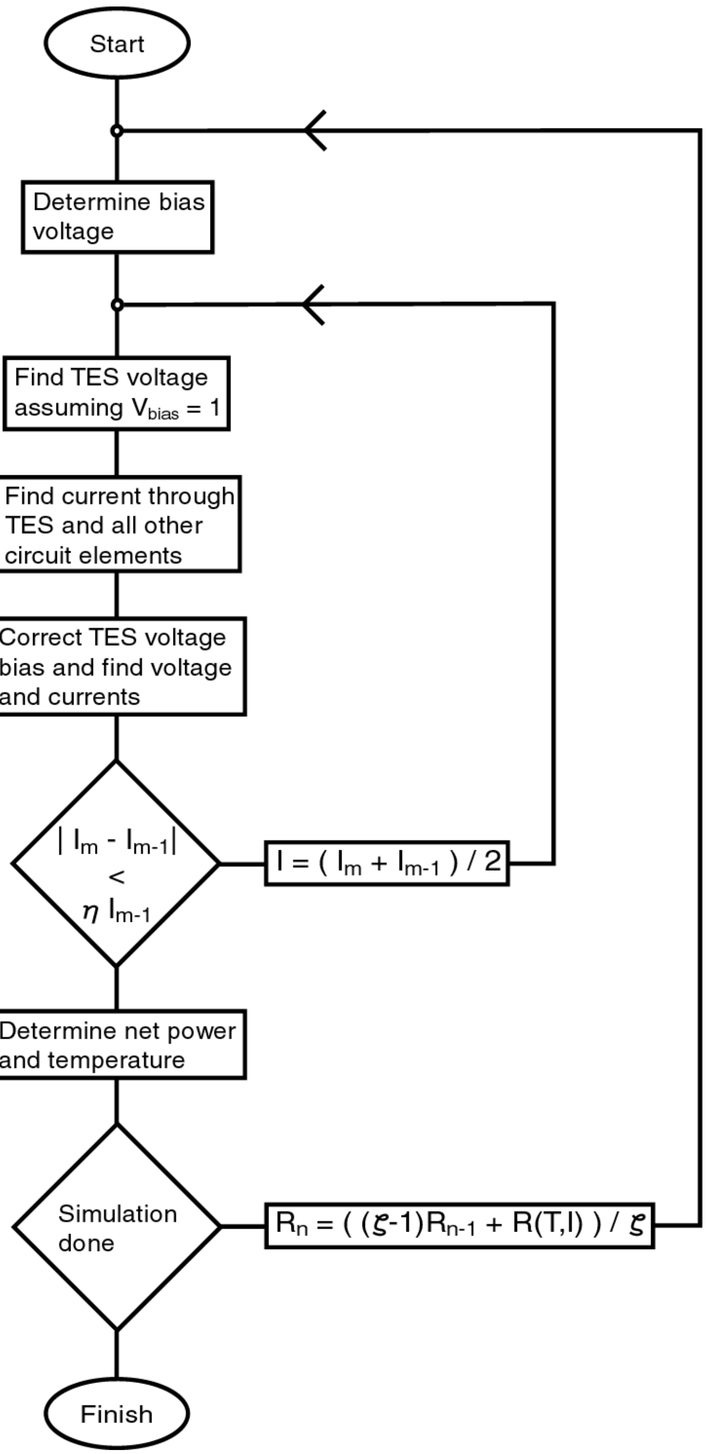

Figure 4.1: TES simulation flowchart.

4.2 Electrical Circuit Modeling

Modeling of the TES and biasing circuitry (see Figure 4.2) is complicated by our desire to be able to create so called IbIs curves in which the bias voltage (V_{bias}) is swept from zero to some large value and back to zero again. This difficulty comes about from the resistance's current dependence and also due to the sharp change in current that occurs during the transition from superconducting to ohmic states.

The TES itself is modeled using a finite element approximation (see Figure 4.3). Generally, the TES is modeled with a few hundred nodes; that is, the TES is broken up into a few hundred individual resistors. The functional form of the resistance at each node is given by

$$R_{i,j} = \frac{R_{max} - R_{min}}{2} \tanh\left[\frac{T_{i,j} - T_c}{T_w} + \left(\frac{|I_{i,j}|}{I_w}\right)^{n_{sc}}\right] + \frac{R_{max} + R_{min}}{2}$$

where R_{max} is the TES's resistance in the normal state,
R_{min} is the superconducting resistance (numerically it is best to not set R_{min} to zero but rather some small value $\sim 10^{-8}\Omega$),
T_c is the midpoint temperature of the superconducting transition,
T_w is the temperature width of the superconducting transition,
I_w is a current-weight,
and $n_{sc} \sim 2/3$ is motivated by [8, 41].

To first determine the TES resistance at step n we let

$$R_n = \frac{(\zeta - 1)R_{n-1} + R(T, I)}{\zeta}$$

where ζ is a stabilization constant whose value ~ 5 is found by trial and error. Picking a large value makes current transitions numerically stable, but requires slower step sizes dt to retain accuracy.

Next, we solve for the voltages at each TES node (to be discussed below) and determine the resulting voltages and currents. We also model the inductor as discussed below. It is likely that the currents that we solve for differ from those that we originally used to compute $R = R(T, I)$. I keep evaluating $R_m(T, I_m)$, V and I

letting

$$I_m = \frac{I_{m-1} + I_{m-2}}{2}$$

until

$$|I_m - I_{m-1}| < \eta I_{m-1}$$

where $\eta \sim 10^{-3}$ is satisfied for all nodes, ensuring a self consistent answer. I have enumerated the individual steps m here to prevent confusing them with the steps n that involve simulation time steps dt (again, see Figure 4.1).

The rest of the circuit, including the inductor, is modeled by finding the macroscopic current through the TES I_n. A simple circuit analysis reveals that it is given by

$$I_n = \frac{\frac{V_{bias} R_{shunt}}{R_{bias} + R_{shunt}} + \frac{L I_{n-1}}{dt}}{\frac{R_{bias} R_{shunt}}{R_{bias} + R_{shunt}} + R_{true} + R_{parasitic} + \frac{L}{dt}}.$$

4.2.1 TES Voltage Modeling

In the simulation, temperature, and therefore resistance, is modeled at each node. However for the purpose of modeling the electrical circuit the interconnects need to have a resistance which is given by averaging the resistance of the two nodes that they connect.

We will now set up the system of equations $\mathbf{G}V = B$ where $\mathbf{G}$ is a sparse, square matrix of size mn. I will explain the process for creating the matrix $\mathbf{G}$ and the vector B. We then solve for V.

Nodes either are voltage biased / grounded or are not. Those that are not biased or grounded impose current conservation requirements. In general, from Kirchhoff's current law, the equation to be satisfied for nodes that have four adjacent nodes is

$$\frac{V_{left} - V}{R_{left}} + \frac{V_{right} - V}{R_{right}} + \frac{V_{top} - V}{R_{top}} + \frac{V_{bottom} - V}{R_{bottom}} = 0.$$

Nodes without four adjacent nodes will result in the appropriate terms being removed, for example a node with a top, left and right neighbors is given by

$$\frac{V_{left} - V}{R_{left}} + \frac{V_{right} - V}{R_{right}} + \frac{V_{top} - V}{R_{top}} = 0.$$

The result on the **G** matrix is straightforward. The diagonal elements are given by

$$\mathbf{G}_{ii} = -\frac{1}{R_{left}} - \frac{1}{R_{right}} - \frac{1}{R_{top}} - \frac{1}{R_{bottom}}.$$

The non-diagonal elements that couple adjacent nodes are given by

$$\mathbf{G}_{terms\ which\ couple\ adjacent\ nodes} = \frac{1}{R_{adjacent}}.$$

Nodes that have their voltage fixed either through voltage biasing or grounding satisfy the equation $V = V_{bias}$. They are given the coupling terms

$$\mathbf{G}_{ii} = 1,$$

the other terms in the row are

$$\mathbf{G}_{ij} = 0,$$

where $j \neq i$.

By now it is should be obvious how to set up B and complete Kirchhoff's current law. For the rows in **G** that describe current conservation,

$$B_i = 0.$$

Whereas the rows in **G** that describe voltage biasing,

$$B_i = V_{bias}.$$

We can then solve

$$V = \mathbf{G}^{-1}B,$$

to find the voltages at all TES nodes.

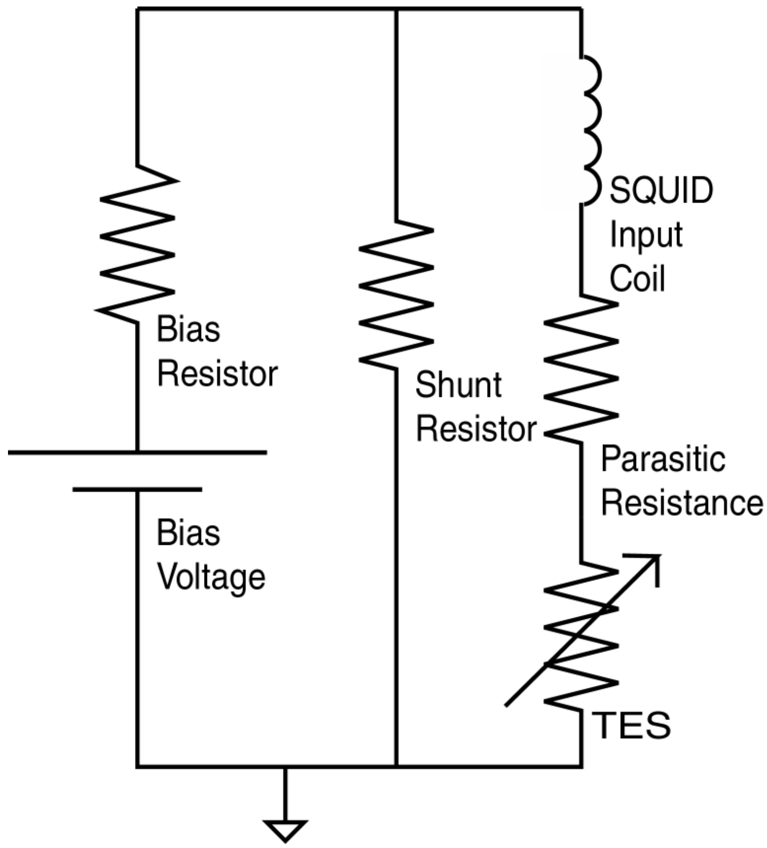

Figure 4.2: TES simulation biasing circuitry. Modeling accurately reflects the real biasing circuitry shown in Figure 2.3.

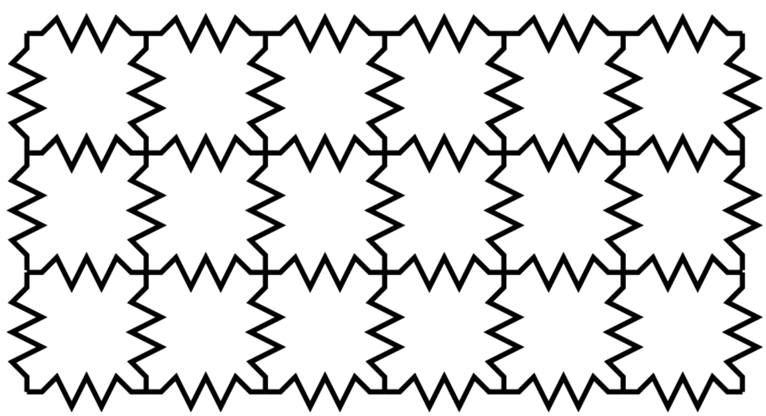

Figure 4.3: TES resistor interconnects as modeled using a finite element approximation.

4.3 Thermal Processes

After determining the voltages at each node, Joule heating is calculated by

$$P_J = \frac{V^2}{R}.$$

Power into the substrate is given by

$$P_S = -\Sigma\left(T^n_{TES} - T^n_{substrate}\right).$$

Thermal diffusion is a little more complicated to implement numerically but its physical process is given by

$$\frac{\partial T}{\partial t} = D\triangle T,$$

where

$$\triangle T = \nabla \cdot \nabla T = \frac{\partial^2 T}{\partial x^2} + \frac{\partial^2 T}{\partial y^2}$$

and D is given by K/C_V where K is the thermal conductivity and C_V is the heat capacity per unit volume [6].

For non-boundary nodes, $\triangle T$ can be approximated by considering the midpoint and two adjoining points. To see this let us first consider just one dimension, specifically the term $\frac{\partial^2 T}{\partial x^2}$. First we compute $\frac{\partial T}{\partial x}$. In the discrete approximation we can consider some point T_i and either its right neighbor or left neighbor T_{i+1} or T_{i-1}, where i represents the position of some node in the x direction. We obtain either

$$\left.\frac{\partial T}{\partial x}\right|_{right} \to \frac{T_{i+1} - T_i}{\delta x}$$

or

$$\left.\frac{\partial T}{\partial x}\right|_{left} \to \frac{T_i - T_{i-1}}{\delta x},$$

where $\rightarrow$ denotes the move from continuous to discrete space. Next we compute

$$\frac{\partial}{\partial x}\frac{\partial T}{\partial x} \rightarrow \frac{\frac{\partial T}{\partial x}\Big|_{right} - \frac{\partial^2 T}{\partial x^2}\Big|_{left}}{\delta x}$$

$$= \frac{T_{i-1} - 2T_i + T_{i+1}}{(\delta x)^2}. \tag{4.1}$$

Boundary nodes are computed differently. To conserve energy we impose the Neumann boundary condition

$$\nabla T|_{boundary} = 0.$$

Making the discrete approximation is simple, we compute

$$T_i - T_{i-1} = 0 \tag{4.2}$$

for boundary nodes.

T will be the temperature matrix of size $n \times m$ where n and m represents the nodes in the y and x directions respectively. It would be nice to convert the following procedures for computing $\triangle T$ into a matrix operation which considering Equations 4.1 and 4.2 is fortunately is quite simple. The matrices $\tilde{\triangle}_x$ and $\tilde{\triangle}_y$ (see Equation 4.3), of sizes $m \times m$ and $n \times n$ respectively, allow finite calculations of $\triangle T$. Specifically,

$$\frac{\partial^2 T}{\partial x^2} \rightarrow \frac{T\tilde{\triangle}_x}{(\delta x)^2}$$

and

$$\frac{\partial^2 T}{\partial y^2} \rightarrow \frac{\tilde{\triangle}_y T}{(\delta y)^2}$$

where $\tilde{\triangle}_x$ and $\tilde{\triangle}_y$ both have the form

$$\begin{pmatrix} -1 & 1 & 0 & 0 & \cdots & 0 & 0 & 0 \\ 1 & -2 & 1 & 0 & \cdots & 0 & 0 & 0 \\ 0 & 1 & -2 & 1 & \cdots & 0 & 0 & 0 \\ & & & & \ddots & & & \\ 0 & 0 & 0 & 0 & \cdots & 1 & -2 & 1 \\ 0 & 0 & 0 & 0 & \cdots & 0 & 1 & -1 \end{pmatrix}. \tag{4.3}$$

The reader is encouraged to verify that this is equivalent to Equations 4.1 and 4.2 and that the signs are correct for the boundary nodes to ensure heat moves from hot to cold nodes.

The diffusion algorithm is then given by

$$T_{n+1} = T_n + D\ \delta t \left(\frac{T\triangle_x}{(\delta x)^2} + \frac{\triangle_y T}{(\delta y)^2} \right).$$

The algorithm should be stable as long as

$$\delta t < \frac{(\delta x)^2}{2D}$$

is satisfied [42] but I find in practice that a slightly smaller value of dt guarantees convergence. The reader is again advised to experiment a little and ensure that the convergence is accurate.

Chapter 5

1-d Detector

5.1 Introduction

Experimental work on this project began with a simple detector that could resolve position in one direction. This setup allowed simple position cuts to be performed. All devices were run in a commercially available dilution refrigerator, a Kelvinox-15 (KO-15) made by Oxford Instruments. The KO-15's $\sim$37 mK base temperature can be held stable for $\sim$2–3 weeks with the help of an Linear Resistance LR-130 temperature controller.

The detector is mounted as usual on a G-10 board with a collimator and an ^{55}Fe gamma source (see Figure 5.1). This setup is then connected to the KO-15's mixing chamber and the LED is added (see Figure 5.2). The pictures shown are for a 2-d device, but the setup is similar to that used for the 1-d device.

5.2 Corner Biased Detector

The first detector that I (ever) ran was in pretty bad shape as the biasing leads were broken. So, I ran wirebonds to the corners of the TES in order to bias the device (see Figure 5.3). This biasing method has the ill effect of causing inherent phase separation in the device as huge current densities are located near the wirebonds causing this region to be hot. Further away, the current densities are lower and the

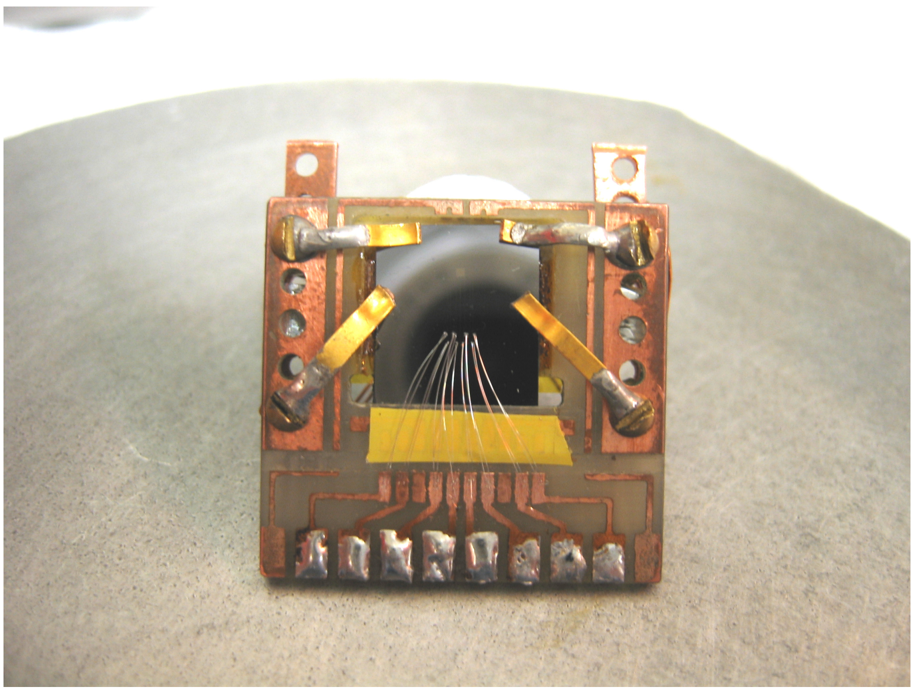

Figure 5.1: 2×2 TES detector picture. The four TESs are barely resolvable (but not distinguishable) half way between the wirebonds and crystal edge. Also shown are gold "fingers" to improve thermal coupling to the mixing chamber. And finally the ^{55}Fe source is the circular, bright object protruding from behind the detector.

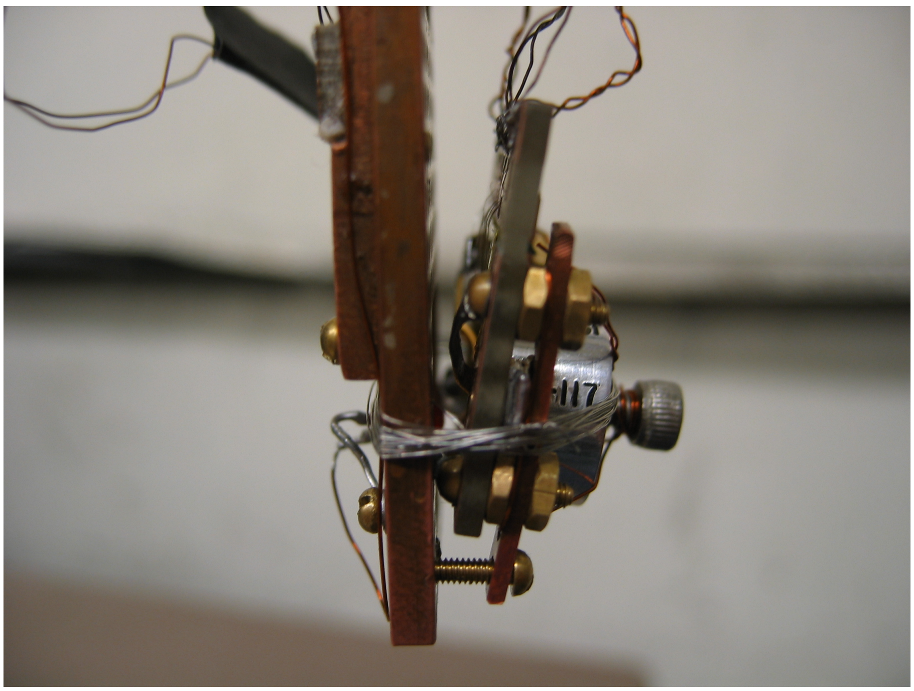

Figure 5.2: 2×2 TES detector on mixing chamber sample stage picture. The mixing chamber is shown on the left. The detector's G-10 mounting frame is in the center. The X-ray source is the object stamped with "117" on the right. Also shown (but likely not obvious to the reader) is the LED which is grounded by the screw on the left side of the mixing chamber. It is grounded by the screw in the left side of the mixing chamber. Also shown is wire wrapping around the mixing chamber and source to improve thermal coupling.

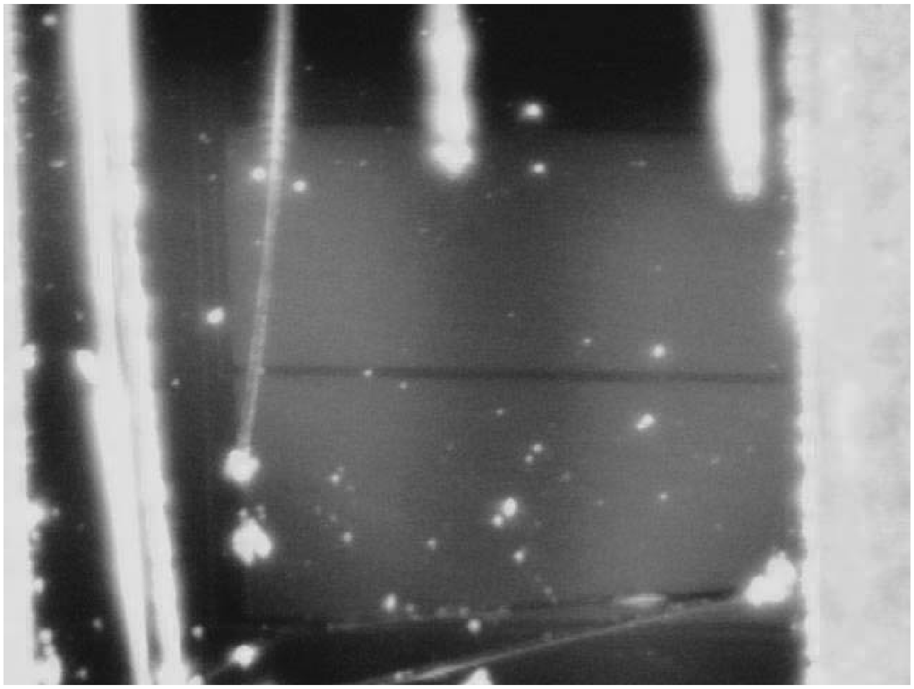

Figure 5.3: Corner biased TES. The photolithographically patterned leads were broken so I wire-bonded directly to the device to bias it. The random white dots are dust that rained down when new air conditioning ducts were installed in the lab.

device is superconducting. The device still had a narrow 1 mK transition width at 78 mK (see Figure 5.4). The narrow width conveys that the TESs are "healthy"; perhaps current is quickly making its way along the aluminum (which superconduct at 1 K) biasing rails and spread more uniformly than I just suggested. Regardless, it would have been better to run devices that were not so badly damaged.

As bad as this detector sounds it is almost amazing that we obtained modest results. The total energy is partitioned between the two TESs (see Figure 5.5). The TES gains are adjusted so that the lines are on a 45° line. The events are then binned according to energy and a histogram is produced. The K_α and K_β lines are resolvable and a $\sim$300 eV at 5.9 keV is determined (see Figure 5.6).

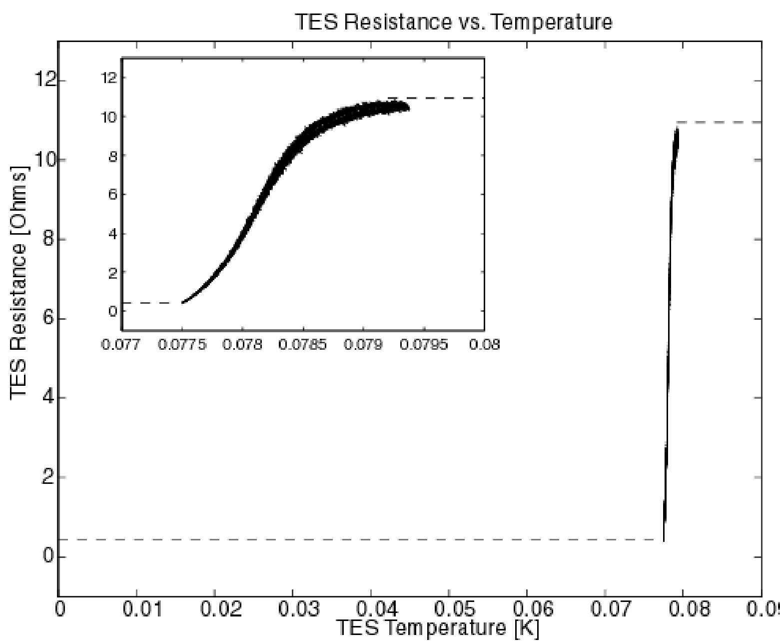

Figure 5.4: Corner biased TES resistance vs. temperature shown for one of the TESs in the device. The temperature is varied by changing the current density. The device shows a nice 1 mK transition width at 78 mK.

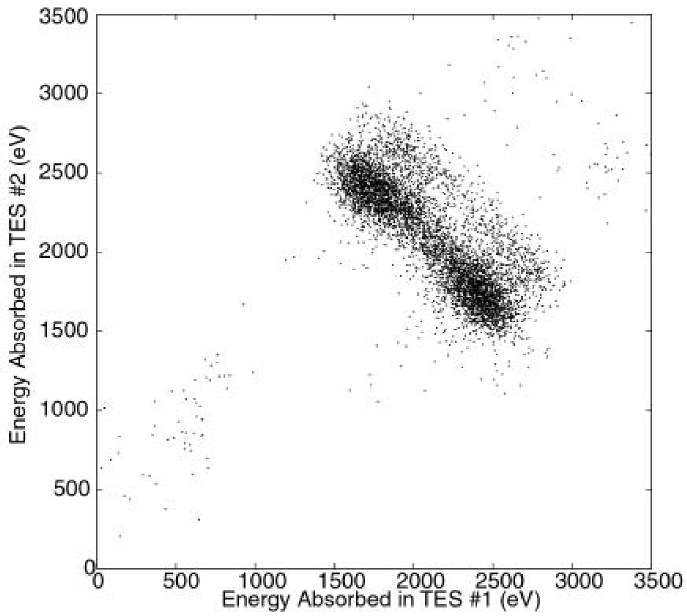

Figure 5.5: Energy partitioning plot. The total collected energy is partitioned between the two TESs. The TES gains are adjusted so that the lines are on a 45° line. However, the overall 49% energy collection is not adjusted in this plot. Here the K_α and K_β lines are clearly resolvable.

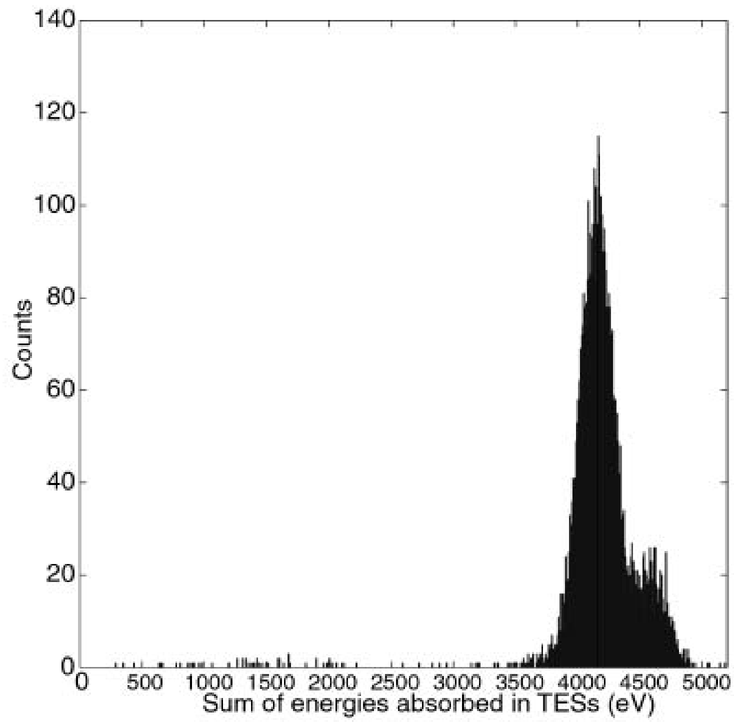

Figure 5.6: Energy histogram. The events are binned according to energy. The K_α and K_β lines are resolvable and a ∼300 eV FWHM at 5.9 keV is determined.

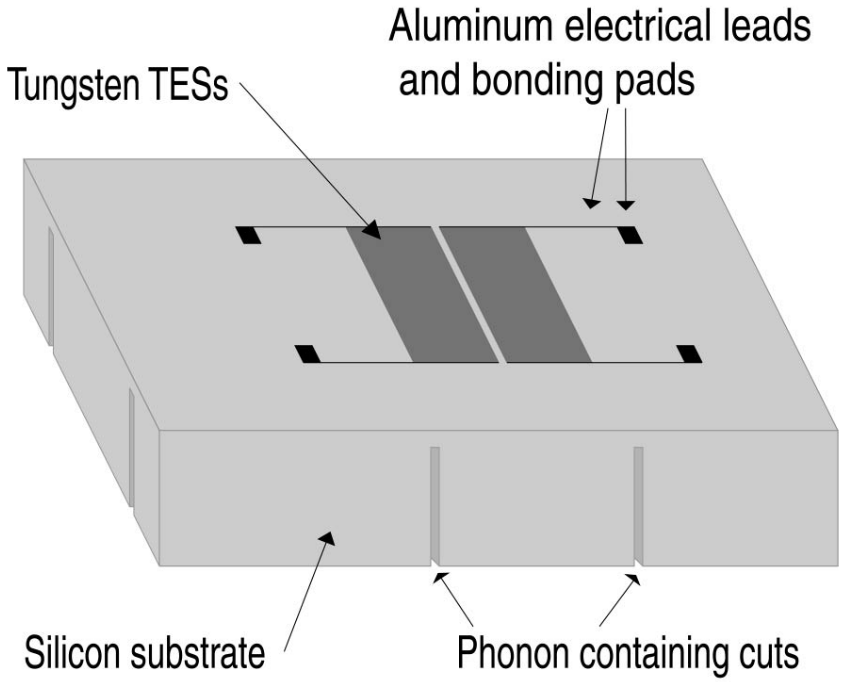

Figure 5.7: 1×2 TES cartoon. X-rays are absorbed on the "backside" of the detector via the photoelectric effect. These either recombine producing phonons which propagate to the TESs or are absorbed on the crystal surface. The trenches keep the phonons in a region where they can be absorbed by the TESs. The two TESs allow position cuts and corrections to be made in the resolvable direction.

5.3 Regularly Biased Detector

The next step is obviously to make detectors that can be biased along uniform rails on opposite sides of the TES. Additionally, we can include trenches in the backside of the detector which will help confine phonons to a region where they can be absorbed by the TESs. The TES in this detector each have dimensions 250 μm×500 μm and are ∼40 nm thick. The backside has ∼50 μm wide and ∼220 μm deep trenches surrounding the active TES region, and the crystal is ∼350 μm thick.

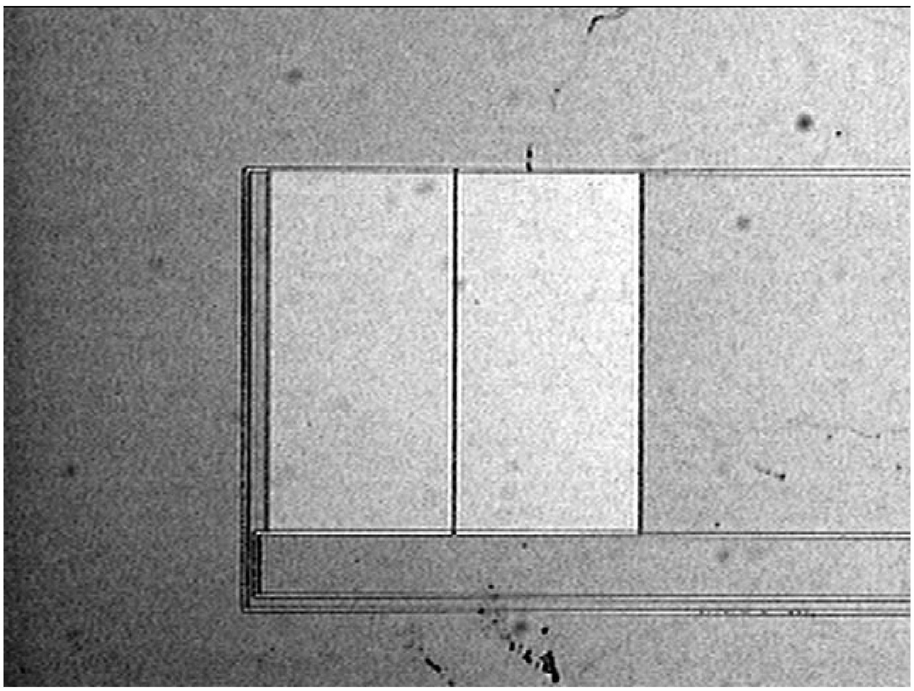

Figure 5.8: 1×2 TES picture. Shown are the two TESs and biasing leads. The wire-bonding pads are not shown. The TESs have dimension 250 μm×500 μm and are ∼40 nm thick. The silicon crystal is ∼250 μm thick.

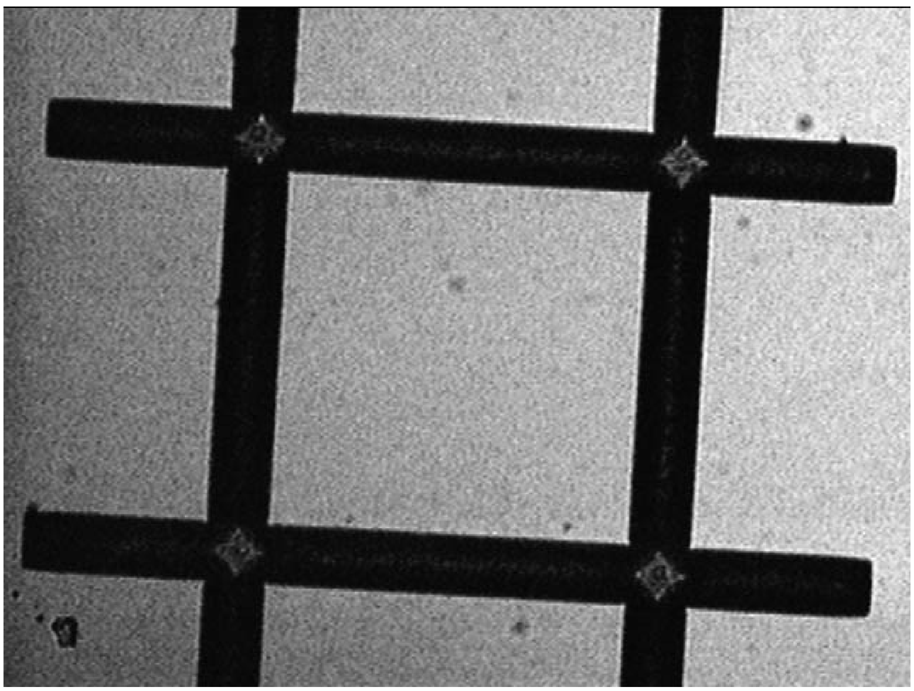

Figure 5.9: 1$\times$2 TES backside trenches. The trenches are $\sim$50 μm wide and $\sim$220 μm deep. They help to confine the phonons to a region where they will interact with the TESs. The diamond shapes where the horizontal and vertical trenches intersect results from a few micron increase in etching in this region.

5.3.1 Actual Noise

A Noise Equivalent Current (NEC) spectrum can be determined by triggering the DAQ with a function generator and removing any X-ray events that slip in (see Figures 5.10 and 5.11). We find, like other groups, that there is excess noise that is identifiable as increased Johnson noise (see Figures 5.12 and 5.13) [16]. There is still however a bump at ~180 kHz and ~110 kHz that is not explained by the model. Recent work in the CDMS collaboration has attributed this bump to a resonance in the SQUID [43, 44]. The NEC can then be integrated $I_{noise} = \int NEC^2 df$ to find a characteristic value of current noise that spoils X-ray traces. Given knowledge of the TES's resistance, it is then trivial to determine the uncertainty in the FWHM. The individual channel contributions are ~22 eV and ~35 eV. A total contribution between the two channels of ~42 eV to the FWHM is estimated.

The traces used to produce the noise spectrum can be analyzed just like X-ray pulses can and we can directly find this static-noise contribution to the FWHM (see Figure 5.14). An ~42 eV contribution is found. This contribution is slightly different than the previous analysis. In the previous analysis, the entire noise pulse is used for baseline subtraction, hence the zero-frequency Fourier component is set to zero. Obviously this technique is not reasonable when analyzing X-ray pulses. Instead, the DAQ pretrigger is set such that the first ~18% of trace is before the X-ray event. Also, in the first method the frequency components are considered to be independent both within each channel and between channels. Of course, this assumption is not necessarily justified and certain frequencies could be canceling out between the two channels.

5.3.2 Theoretical Noise

The theoretical noise spectrum in the extreme electrothermal feedback limit is given by [22].

$$\left\langle |\Delta I_{tot}(\omega)|^2 \right\rangle = \left\langle |\Delta I_{tn}(\omega)|^2 \right\rangle + \left\langle |\Delta I_{dn}(\omega)|^2 \right\rangle$$

where the thermal noise is given by

$$\left\langle |\Delta I_{tn}(\omega)|^2 \right\rangle = \frac{P_{tn}(\omega)^2}{V^2} \frac{1}{1+\omega^2 \tau_{eff}^2}$$

and the detector noise is given by,

$$\left\langle |\Delta I_{dn}(\omega)|^2 \right\rangle = \frac{V_{dn}(\omega)^2}{(R+\imath\omega L)^2} \frac{\left(\frac{TG}{\alpha P_j}\right)^2 + \omega^2 \tau_{eff}^2}{1+\omega^2 \tau_{eff}^2}.$$

The effective recovery time constant is

$$\tau_{eff} = \tau_o \frac{TG}{\alpha P}.$$

The non-ETF recovery time constant is

$$\tau_o = C/G,$$

where C is the TES's heat capacity.

The steepness of the transition is characterized by the dimensionless quantity

$$\alpha = \frac{T}{R}\frac{dR}{dT}. \tag{5.1}$$

The thermal conductivity between the TES's electron and phonon systems is

$$G = KnT^{n-1}. \tag{5.2}$$

The TESs resistance is known along with the shunt resistor and bias current values, from which we can solve for the voltage drop across the TES,

$$V_{TES} = \frac{R_{TES}}{R_{TES}+R_{shunt}} I_{bias} R_{shunt}.$$

The Joule power is

$$P_j = \frac{V_{TES}^2}{R_{TES}}.$$

Table 5.1: Numerical Constants for 1×2 TES Noise

Noise Fit Parameters		
Fixed Variables		
I_{bias} [μAmps]	152	150
R_{shunt} [mΩ]	5	5
$L_{\otimes}$ [nH]	250	250
Adjustable Variables		
Heat capacity [J/K]	1.4×10^{-13}	1.4×10^{-13}
Conductivity [W/K]	1.2×10^{-10}	1.2×10^{-10}
α	530	530
Resistance [Ω]	0.19	0.24
T_{bath} [mK]	60	60

The Joule power also allows us to solve for K

$$P_j = K(T^n_{electron} - T^n_{phonon}).$$

The voltage across the TES is

$$V = \sqrt{P_j R}.$$

The thermal noise power is given by

$$P_{tn} = \sqrt{2k_b(T^2_{electron} + T^2_{phonon})G}.$$

The TES's voltage noise (Johnson noise) is given by

$$V_{dn} = \sqrt{4k_b T R}.$$

If using SI units, the result $(\langle|\Delta I_{tot}(\omega)|^2\rangle)^{1/2}$ will be given in A Hz$^{-1/2}$.

The actual noise is fit to theory with the fixed and adjustable variables shown in Table 5.1.

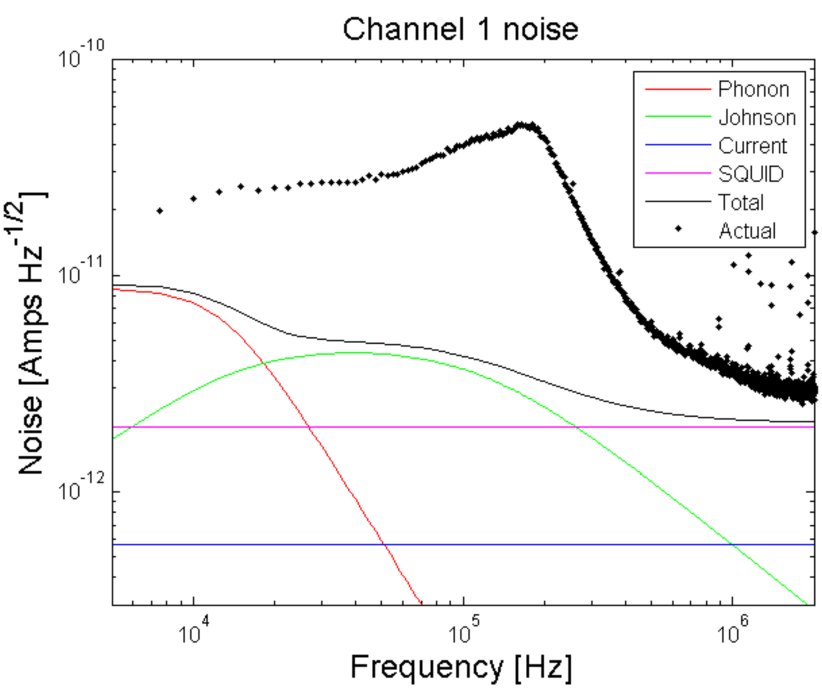

Figure 5.10: 1×2 TES, channel 1 noise. Noise (dots) shows poor agreement with model (solid line), including sensor phonon and Johnson noises, SQUID noise and bias current noise

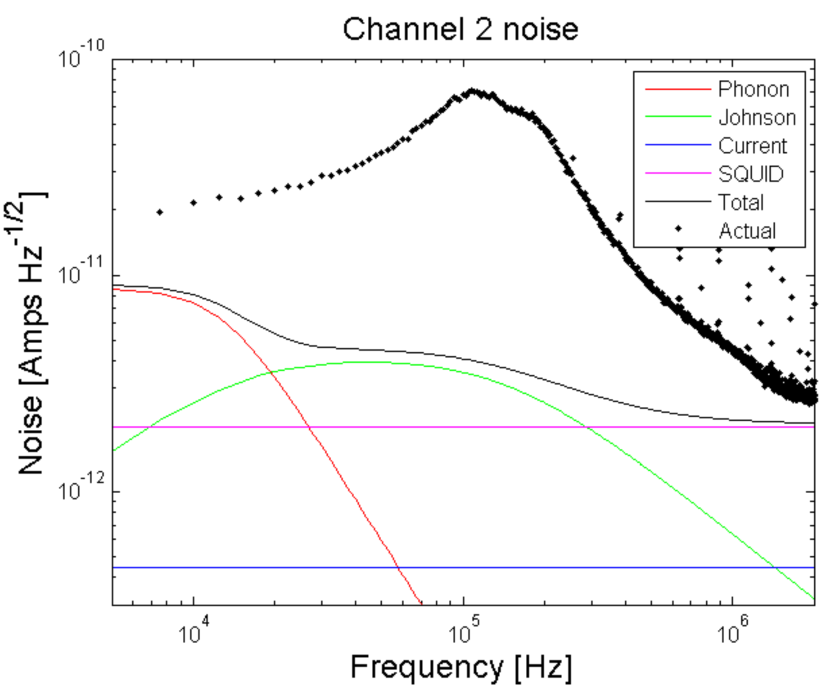

Figure 5.11: 1×2 TES, channel 2 noise. Noise (dots) shows poor agreement with model (solid line), including sensor phonon and Johnson noises, SQUID noise and bias current noise

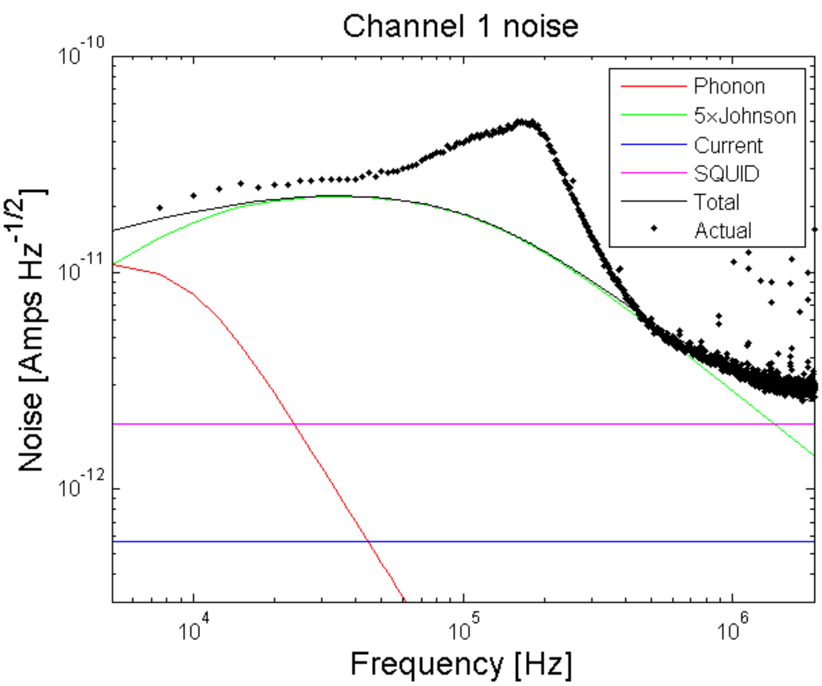

Figure 5.12: 1×2 TES, channel 1 noise with excess Johnson noise. There is better agreement when a 5×Johnson noise term is used. The bump at ∼180 kHz is believed to be due to resonances in the SQUID. Re-biasing the SQUID could eliminate or reduce this feature, but was not done.

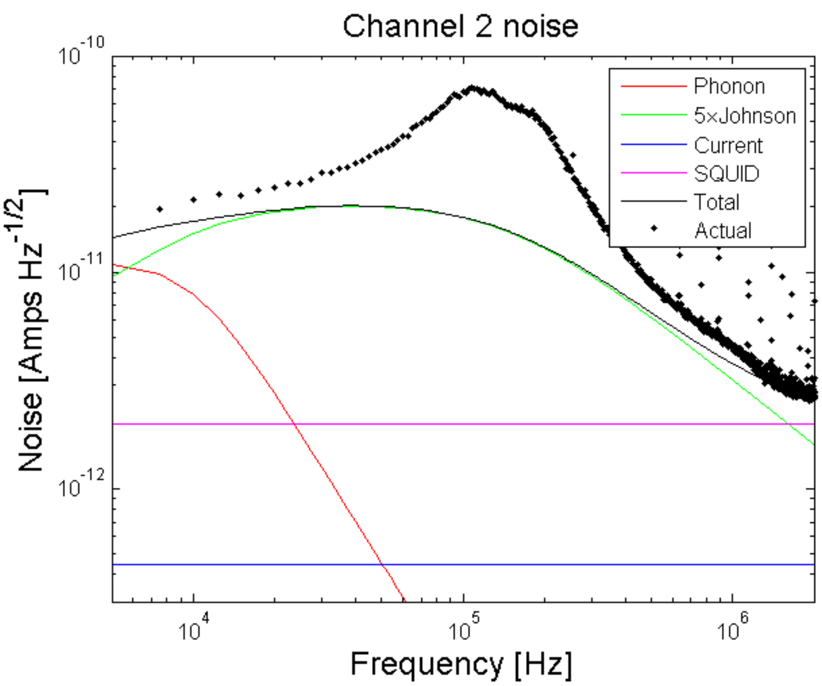

Figure 5.13: 1×2 TES, channel 2 noise with excess Johnson noise. There is better agreement when a 5×Johnson noise term is used. The bump at ∼110 kHz is believed to be due to resonances in the SQUID. Re-biasing the SQUID could eliminate or reduce this feature, but was not done.

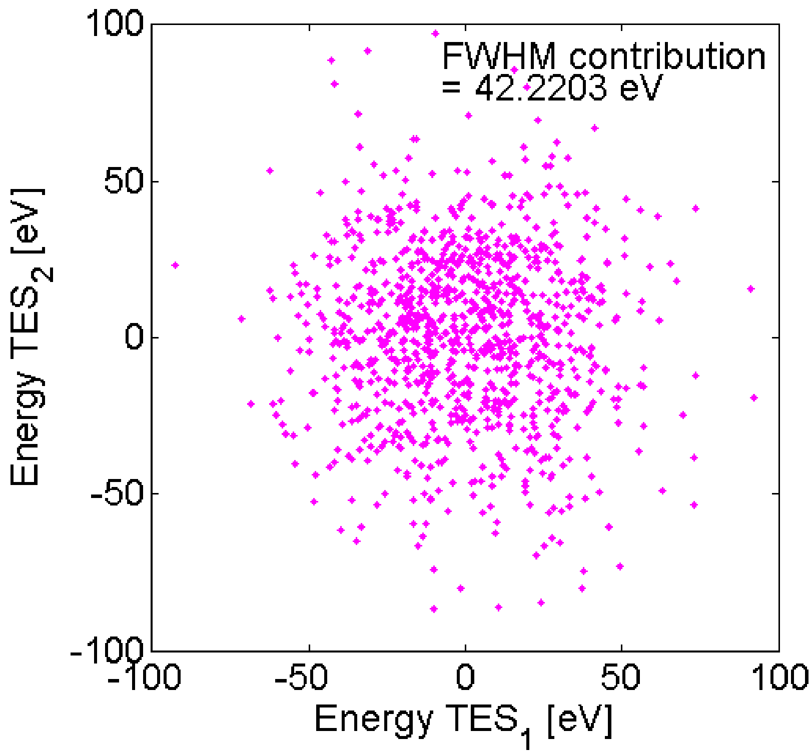

Figure 5.14: 1×2 TES noise partitioning. The noise traces are analyzed like X-ray pulses with the first ∼18% of the trace used for baseline subtraction. The baseline noise contributes a ∼42 eV effect towards the FWHM.

5.3.3 X-ray Pulses and Spectra

Sample pulses are shown in Figures 5.15 and 5.16. Since it is the sum of energy from channel 1 and 2 that is a constant for the K_α and K_β bands, we do not expect the pulses to be exactly uniform. However, visually we can see that the rise and fall time-constants are (visually) the same for all events. We see that there are two fall time constants, short and long, which are constant in all the pulses. The transition is perhaps due to phase-separation in the detector (see Appendix B). The energy difference is likely due to position effects in the detector. We also note that 2 $\times$ the half-width-half-maximum (HWHM) is $\sim$100 eV at 5.9 keV. We expect this value to be less dependent on position effect pathologies and thus be a better gauge of detector performance capability.

Generally, the first plot (see Figure 5.17) made shows how energy is partitioned between the two TESs for each X-ray event. The total energy absorbed in the two TESs is $\sim$49% of the incident energy. The wrapping in the lower right part of the plot is due to events which occur close to the detector edge, allowing more energy to escape through the connecting bridges. A slight misalignment of the collimator allows this wrapping to happen on only one side of the detector. The darkened points in the partition plot will be used for determining a spectrum since these events occur near the center of the detector. The gain between the two channels has been adjusted so that the selected points lie on a 45° line. It is then a trivial matter to rotate the previous plot to create a position vs. energy plot (see Figure 5.18) and obtain our ultimate goal: creating an energy spectrum (see Figure 5.19). The improvement in this detector is easily seen. The K_α and K_β lines are clearly distinguishable and a 152 eV FWHM at 5.9 keV is determined.

It is noticed in the energy histogram that the high energy side is noticeably sharper than the low energy side (see Figure 5.19). To be clear, the fitting is not affected by the low energy tail as the low event rates do not make much of a contribution to χ^2. It is believed that the broadening of the low energy side is due to our inability to resolve the other direction and apply cuts. Benefit should be found by making a detector in which we can resolve both directions.

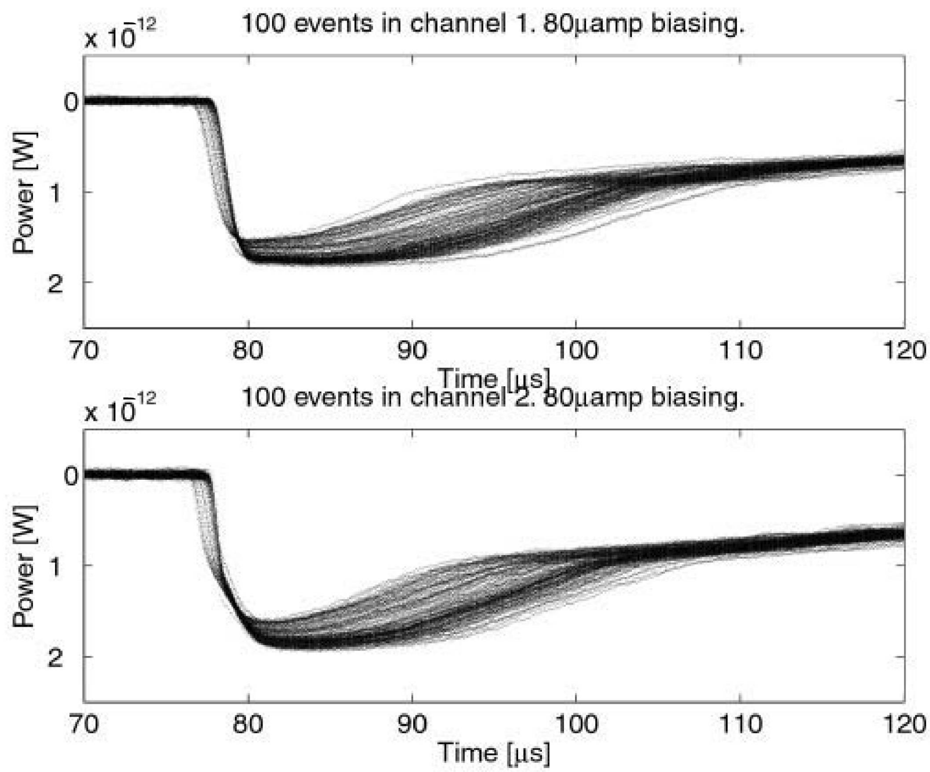

Figure 5.15: 1×2 TES X-ray traces. Since it is the sum of energy from channel 1 and 2 is a constant for the K_α and K_β bands, we do not expect the pulses to be exactly uniform. However, visually we can see that the rise and fall time-constants are (visually) the same for all events.

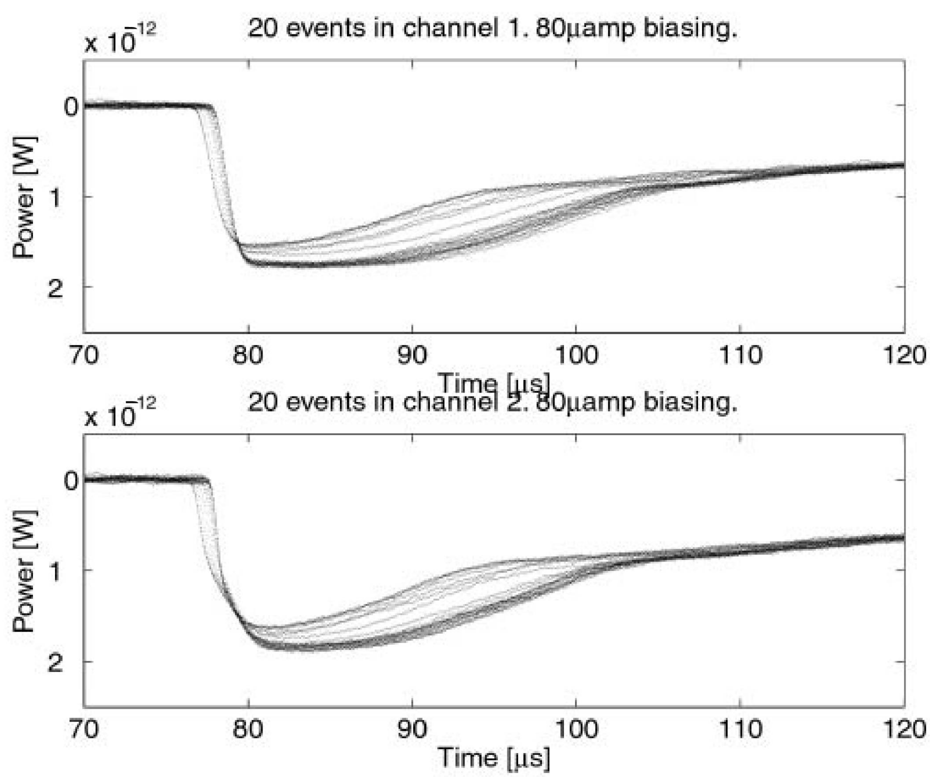

Figure 5.16: 1×2 TES K_α traces. Again, the sum of energy from channel 1 and 2 that is a constant for the K_α and K_β bands, we do not expect the pulses to be exactly uniform. However, visually we can see that the rise and fall time-constants are (visually) the same for all events.

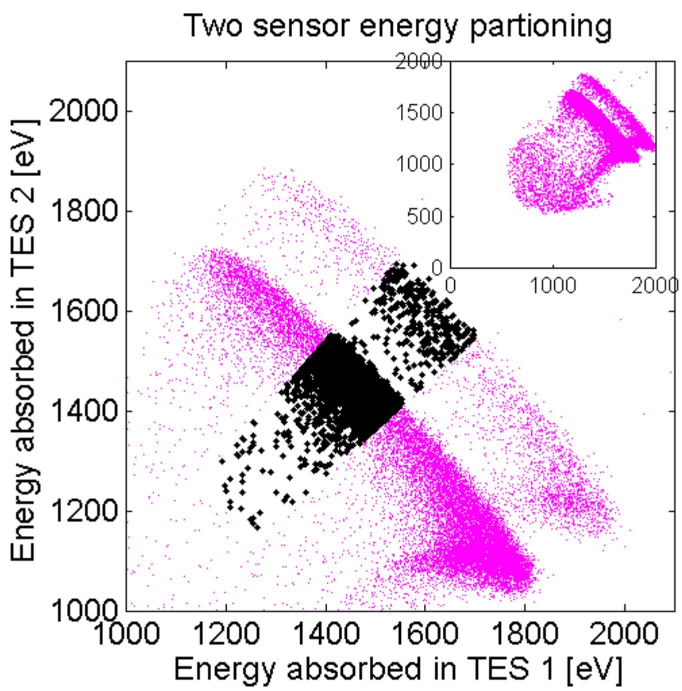

Figure 5.17: 1×2 TES energy partitioning plot. The wrapping in the lower right part of the plot is due to misalignment of the collimator with the device which causes x-rays to be incident on the trench walls and floor. The darkened points will be used for determining a spectrum. The gain between the two channels has been adjusted so that the selected points lie on a 45° line. The K_α and K_β lines are clearly resolvable and well separated.

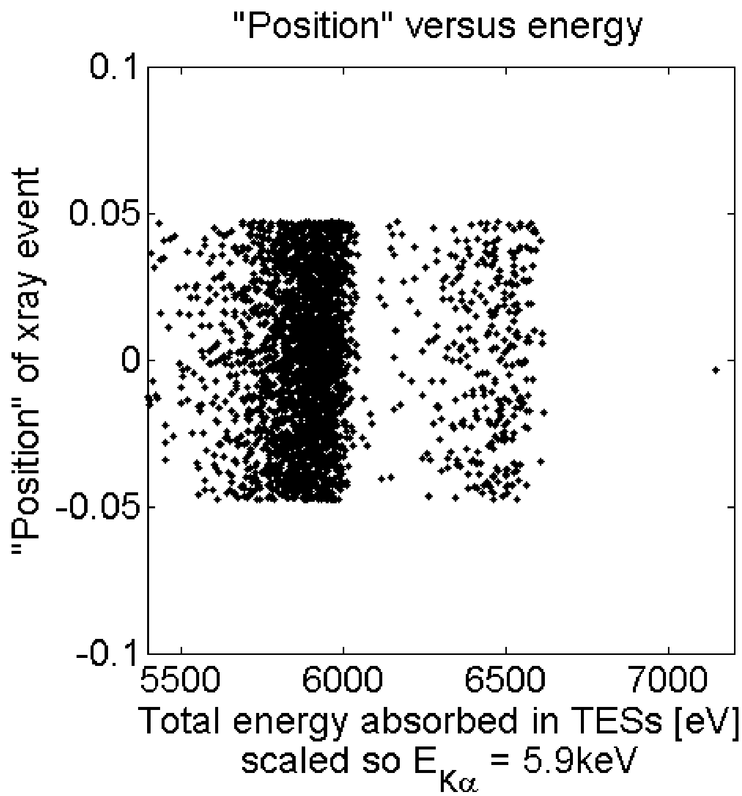

Figure 5.18: 1×2 TES position vs. energy plot. The position is given in arbitrary units. This view helps us to ensure that the relative TES gains are adjusted correctly as can be seen by the line's vertical orientation. Also, the overall gain has been calibrated such that K_α is at 5.9 keV.

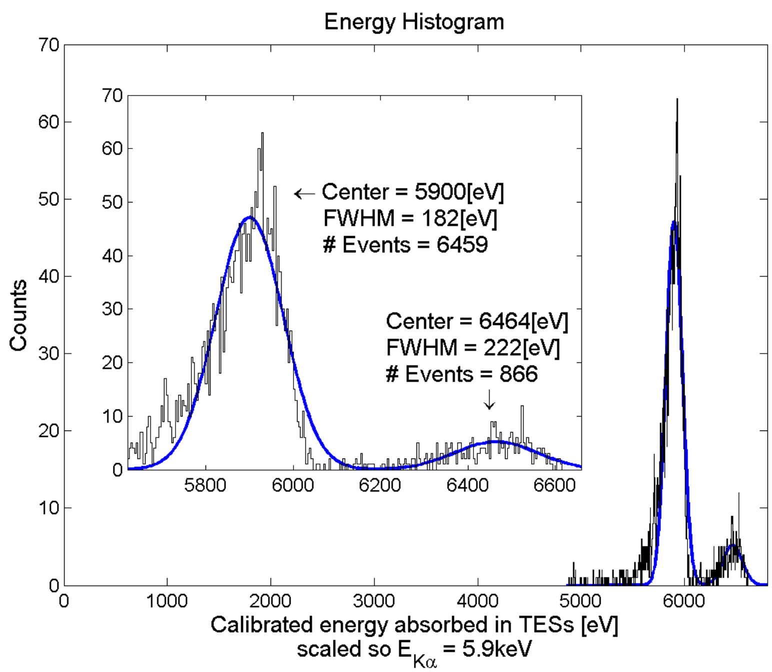

Figure 5.19: 1×2 TES energy histogram plot. The K_α and K_β lines are resolvable and a 152 eV FWHM at 5.9 keV is determined.

Chapter 6

2-d Detector

6.1 Introduction

Based on the successes seen in the previous 1-d resolving detectors we are encouraged to continue developing 2-d resolving detectors. The design is almost identical, each TES is simply split in half (see Figure 6.1). Fortunately these were fabricated along with the 1-d detector that was just discussed. A benefit of producing these on the same wafer is that the trenching and other fabrication issues will be the same (or as similar as possible), allowing a proper side-by-side comparison of the two designs which can rule out fabrication details if any improvement (or worse, degradation) is seen. The detector is mounted as usual on a G-10 board with a collimator and ^{55}Fe source (see Figure 5.1). This setup is then connected to the KO-15's mixing chamber and the LED is added (see Figure 5.2). Like the 1-d detector analysis, we acquire noise traces by randomly triggering the DAQ 6.2. The baseline noise provides a 37 eV effect in this case. This noise is again quite large and we have wondered if the spontaneous emptying of charge-traps, which would generate phonon and couple to our TESs, could be contributing.

The data analysis procedure is similar to the 1-d detector. A total of 2.92 keV from the K_α band is absorbed into the TESs. This value represents 49.5% of the initial energy, which agrees well with the 49% absorbed in the trenched 1-d detector. One notable difference between the two detectors is seen when looking at the X-ray traces (see Figure 6.3). The traces shown are the sum of the four channels and the events are from a relatively small region in the center of the detector. What is notable about these is their single decay time. Compared to the 1-d detector, the TESs were split such that current travels only 1/2 the distance, reducing the opportunity for phase separation.

Partition plots are again created (not shown) to aid in initially adjusting the four channels' gains. Position corrections are then applied. Since we are working in two dimensions, a trial and error method for adjusting gains (like that used for the 1-d detector) is too inefficient. To apply the corrections, first a total energy E_i and position (x_i, y_i) for each event is determined:

$$E_i = E_{TES_1,i} + E_{TES_2,i} + E_{TES_3,i} + E_{TES_4,i},$$

$$x_i = \frac{(E_{TES_1,i} + E_{TES_2,i}) - (E_{TES_3,i} + E_{TES_4,i})}{E_{TES_1,i} + E_{TES_2,i} + E_{TES_3,i} + E_{TES_4,i}}$$

and

$$y_i = \frac{(E_{TES_2,i} + E_{TES_3,i}) - (E_{TES_1,i} + E_{TES_4,i})}{E_{TES_1,i} + E_{TES_2,i} + E_{TES_3,i} + E_{TES_4,i}}.$$

The corrections can be made to any order; 0 would result in no correction, 1 in a linear correction, 2 in a quadratic correction, etc... I have generally favored even ordered corrections and an order greater than four seems to be unhelpful. For a second order correction we setup the matrix

$$A = \begin{pmatrix} 1 & x_1^2 & x_1 y_1 & y_1^2 & x_1 & y_1 \\ 1 & x_2^2 & x_2 y_2 & y_2^2 & x_2 & y_2 \\ & & \vdots & & & \\ 1 & x_n^2 & x_n y_n & y_n^2 & x_n & y_n \end{pmatrix},$$

where there are a total of n X-ray events to be analyzed.

Next, we setup the array

$$b = \begin{pmatrix} E_1 \\ E_2 \\ \vdots \\ E_n \end{pmatrix}.$$

The position correction parameters $\tilde{x}$ are then found, in a least squares sense, by solving the equation

$$A\tilde{x} = b + \varepsilon,$$

where ε represents an error vector. An algebraic solution is given by $\tilde{x} = (A^T A)^{-1} A^T b$, where A^T is the transpose of A.

The "fitted energy" (not to be confused with the corrected energy; what we are ultimately solving for) E_{fit} is given in vector form

$$E_{fit} = A\tilde{x}.$$

The corrected energy $E_{corrected}$ is then given by

$$E_{corrected,i} = E_i / E_{fit,i} \times \tilde{x}_1,$$

where $\tilde{x}_1$ contains the average energy of the analyzed events.

A position plot (see Figure 6.4) is then created. For this plot we make a bold leap and try to *estimate* the position of the X-ray events in real units (μm). To make this determination, we first have to make a reasonable guess about the portion of the detector that is being illuminated. We are using a $\sim$250 μm diameter collimator however, it is spaced slightly off of the detector. With the resulting solid angle leakage, we expect that we are exposing almost all of the detector surface. From there we assume that in a 200 μm $\times$ 200 μm region of the 500 μm $\times$ 500 μm detector that we should see $(200/500)^2 = 0.16\%$ of the total events. The K_α and K_β bands are well separated and quite sharp.

Finally we can produce our desired energy histogram (see Figure 6.5). There is obviously a large advantage in using the 2-d detector, with its ability to make position

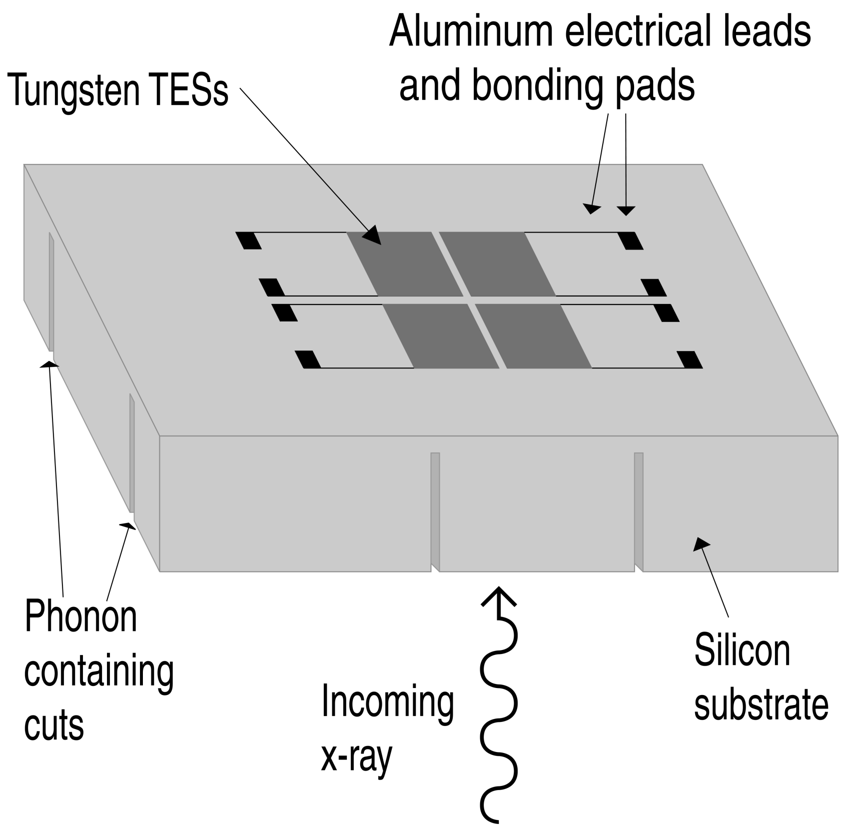

Figure 6.1: 2×2 TES cartoon. X-rays are absorbed on the "backside" of the detector via the photoelectric effect. These either recombine producing phonons which propagate to the TESs or are absorbed on the crystal surface. The trenches keep the phonons in a region where they can be absorbed by the TESs. The four TESs allow position cuts and corrections to be made in the two resolvable directions.

cuts and corrections in both directions, as the energy resolution (FWHM = 80 eV at 5.9 keV) is improved by over a factor of two. The next step will be in limiting energy losses in the detector with the assumption that if there are less losses then there should be less statistical fluctuation in those losses between X-ray events.

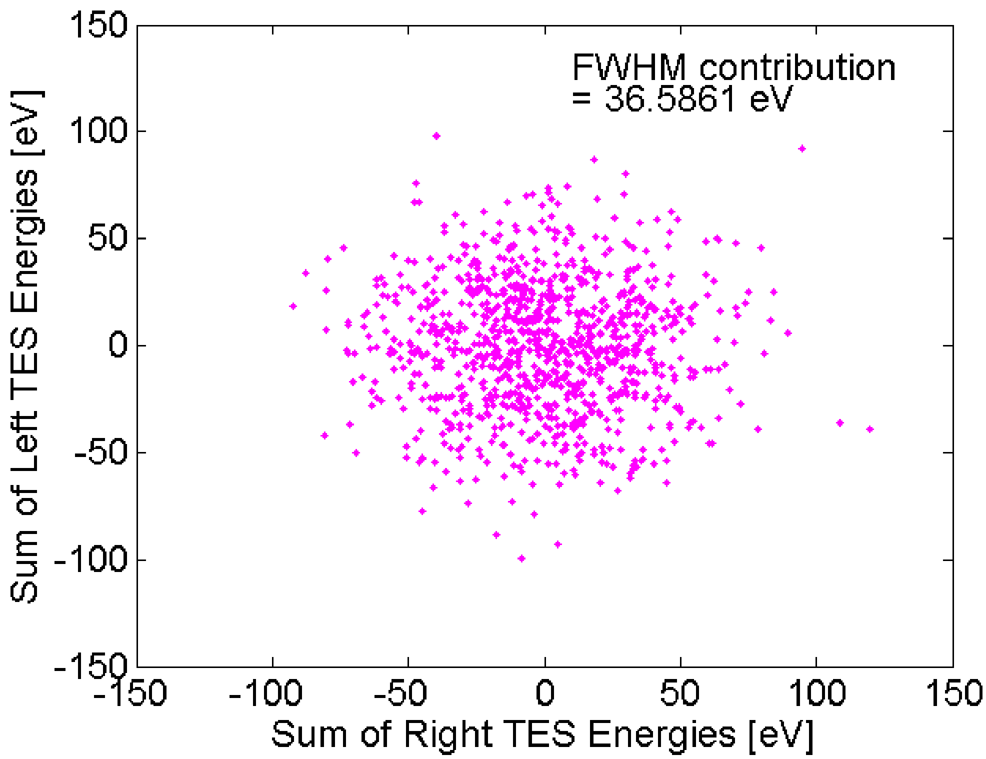

Figure 6.2: 2×2 TES noise partitioning. The noise traces are analyzed like X-ray pulses with the first ∼18% of the trace used for baseline subtraction. The baseline noise contributes a ∼37 eV effect towards the FWHM.

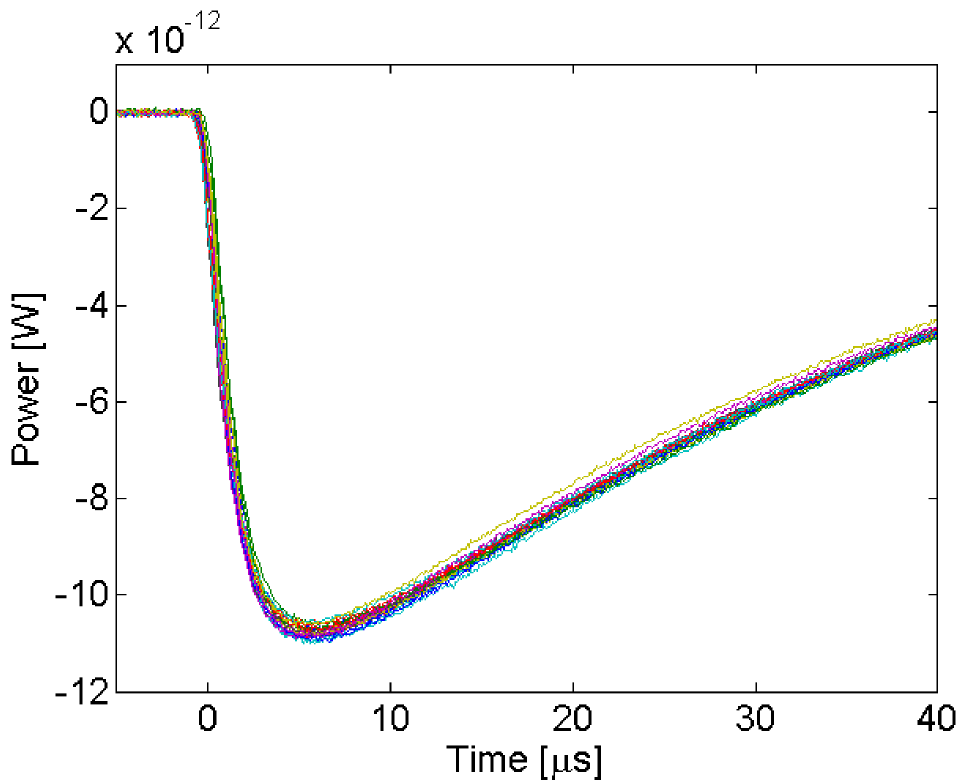

Figure 6.3: 2×2 TES detector K_α traces. The traces show good uniformity but there are obviously different energies hitting the detector. From simulations we expect the energy is absorbed into the TESs in $\sim$1 μsec. These combined suggest that it is position effects and not (visually obvious) long-lived phonon sources that effect energy resolution.

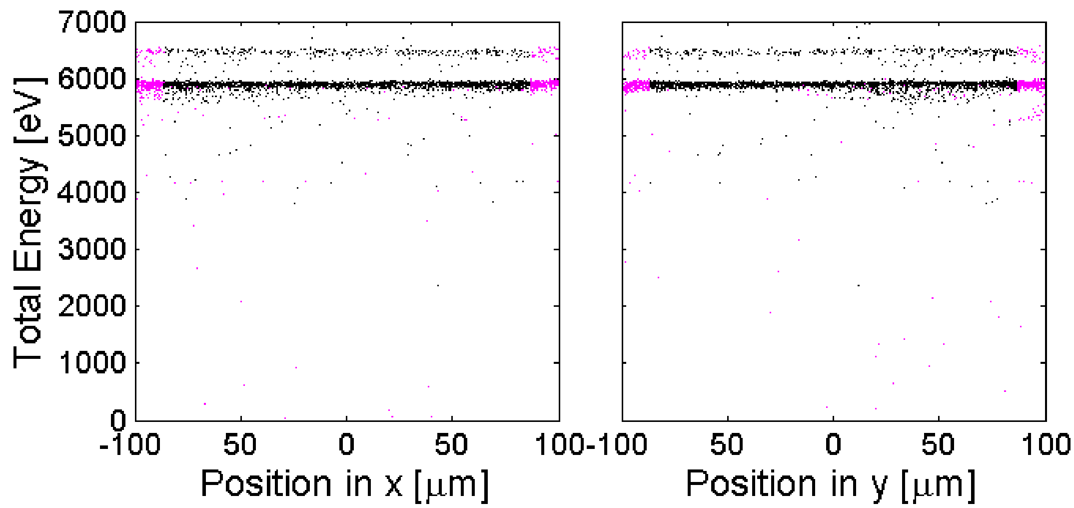

Figure 6.4: 2×2 TES detector position plot. An attempt is made to give the position in real units of μm. The scale was made by considering the spatial distribution of events. This view helps us to ensure that the relative TES gains are adjusted correctly, as can be seen by the line's vertical orientation. Also, the overall gain has been calibrated such that K_α is at 5.9 keV.

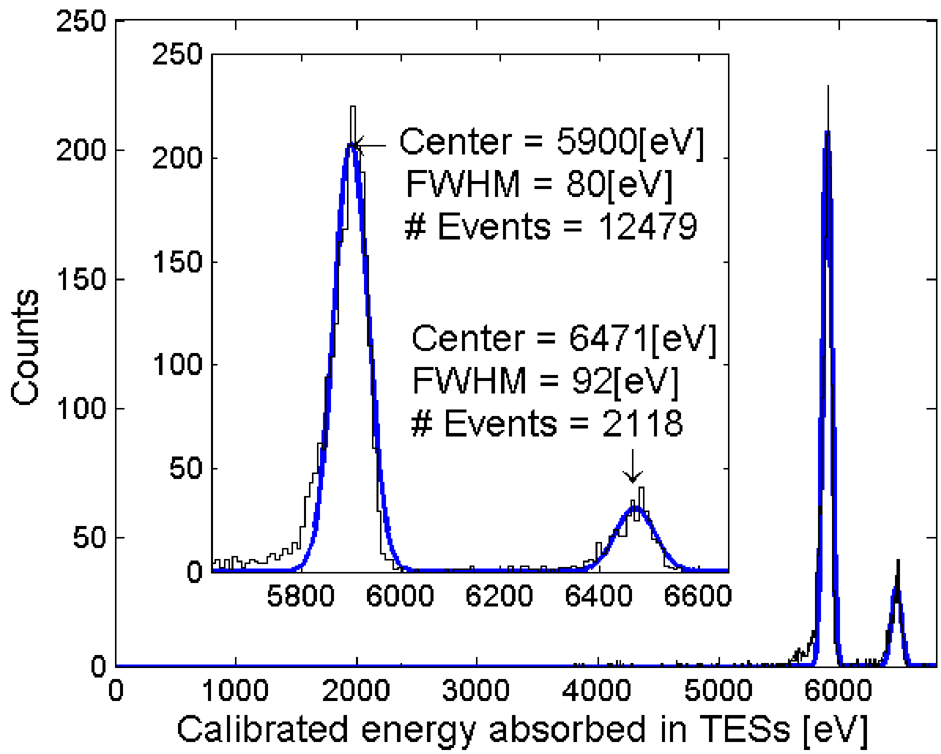

Figure 6.5: 2×2 TES detector histogram. The K_α and K_β lines are resolvable and an 80 eV FWHM at 5.9 keV is determined.

Chapter 7

2-d Detector With Deep Trenches

7.1 Introduction

The search continues for understanding the energy line width and improving the energy resolution. At least two loss mechanisms are obvious. The first is that some loss is occurring in the bulk, most likely due to electron-hole pair losses. Another possibility involves losses through the trenches, either phonons or electron-hole pairs that diffuse out of the active part of the detector before recombining.

Simulation and simple numerics suggest that the loss is in the bulk, but losses due to the trenches are easier to reduce.

Effects that we interpreted to be phase separation were seen in the previous detector. Since the length scale that phase-separation occurs at scales like $l \sim T_c^{-3/2}$, we can make the TESs shorter to prevent phase-separation. One method of effectively shortening the current path length is "splitting" the TESs (see Figures 7.1 and 7.2). Unfortunately, the T_c in our new detectors was ~125 mK, compared to ~87.5 mK. If the new TESs had a length ~0.59 of the previous one then we would not expect any benefit. These TESs have a length 1/2 of the previous one so we only expect a small improvement.

Other notable differences are the wide transition ~10 mK compared to ~1 mK in the previous detector (it is not known whether this wide width will effect energy resolution). And also, the lack of gold deposition on the inactive area of the detector, which was done on the previous detector to improve thermal contact with the mixing chamber. It was considered unimportant and avoided in this detector, but may in fact be an important process (as discussed later).

The summed traces are not ideal (see Figure 7.3) as the K_α and K_β bands are not well separated through out the pulse recovery. If the four TES's pulse shapes vary then upon adding them, we could see variations such as these. The pulse-peaks can be fit to polynomials and cuts and corrections can be applied. Cuts are applied uniformly with respect to the initial X-ray position. Therefore it is unlikely that variations in pulse shape are causing this effect.

If we ignore these flaws, and perform the analysis as similarly as possible to that in Chapter 6 then we are left with a 103 eV FWHM (see Figure 7.4), compared to 80 eV in the previous case. This detector performs significantly worse! If however, we do perform cuts and corrections on the pulse shape then the line width is improved to a 72 eV FWHM (see Figures 7.5 and 7.6).

A total of 4.10 keV from the K_α band is absorbed into the TESs. This value represents 69.6% of the initial energy. It must be stressed in this analysis though that the four TES responses had some variation. During the analysis, gains of 1, 1, 1.19 and, 1.88 else were applied to the four TESs. Part of this variation can be explained by using SQUIDs 1, 2, 4 and, 5. The first three have shunt resistors of value $R_{shunt} = 20$ mΩ while for the last, $R_{shunt} = 5$ mΩ. The small deviation in the third channel's gain is likely due to a feedback resistor that was repaired. So, we assume the non-one gain values are legitimately correcting for known effects and the total absorbed energy is accurate.

At any rate, we can take the percentage of energy deposited in this detector and the 220 μm deep trenched detector and linearly extrapolate to determine that 75.6% of energy would be absorbed in a detector that was completely trenched. This discrepancy might suggest that the detector is incorrectly calibrated and in fact, we are absorbing more energy into the TESs than we think we are which could be possible for example if the shunt resistor values were not well known. Or it could suggest some loss mechanism elsewhere in the detector. At this point however, it is simply easiest (and most honest) to acknowledge that the linear extrapolation is not necessarily

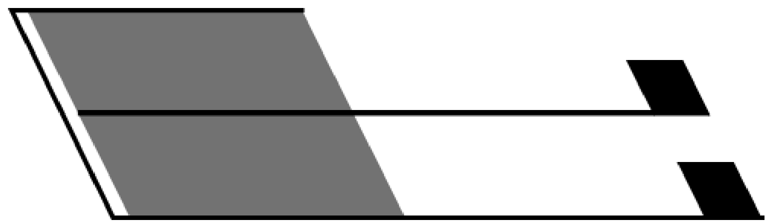

Figure 7.1: A "split" TES where the TES is biased from both the left and right side and the ground line runs down the center of the TES. This scheme results in a TES more stable against superconducting-normal phase-separation.

justified.

7.2 Fluorescence

We have also invoked a fluorescence scheme which will allow us to shine lower energy X-rays onto the detector. When an X-ray is absorbed photoelectrically in a material, it does so by kicking out an electron. This electron is then replaced by another electron which fills the vacancy, releasing energy. As the electron orbitals have discrete energies associated with them, a discrete X-ray line is produced. Auger effects also occur, so not all absorbed X-rays produce fluorescence. The fluorescence yield is given by $\omega_i = Z^4/(A_i + Z^4)$ where A_i is $\sim 10^6$ and $\sim 10^8$ for K shell and L shell X-rays respectively [45]. Obviously we are more interested in K-shell X-rays due to their larger abundance. The K-shell fluorescence yields for calcium, potassium, chlorine, phosphorous and aluminum are 0.163, 0.140, 0.097, 0.063 and 0.039 respectively [46].

The lower energy X-rays are beneficial since they have a shorter attenuation length and are absorbed more closely to the crystal surface (see Figure 7.7). This shorter attenuation length would naturally reduce the dependence on the "irresolvable" dimension on energy resolution. The major drawback with this scheme is that X-rays are not directly incident on the detector (see Figure 7.8) and therefore their count rate is significantly reduced. This problem of course can be remedied by using a stronger source.

The first detector that I ran with this setup was slightly different, the width and

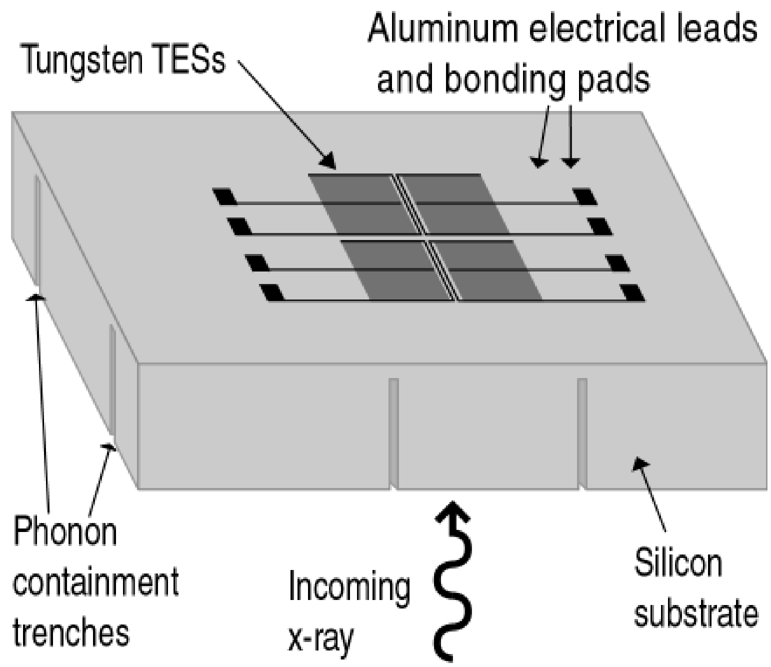

Figure 7.2: A 2×2 "split"-TES detector. The TESs are more stable against superconducting-normal phase-separation.

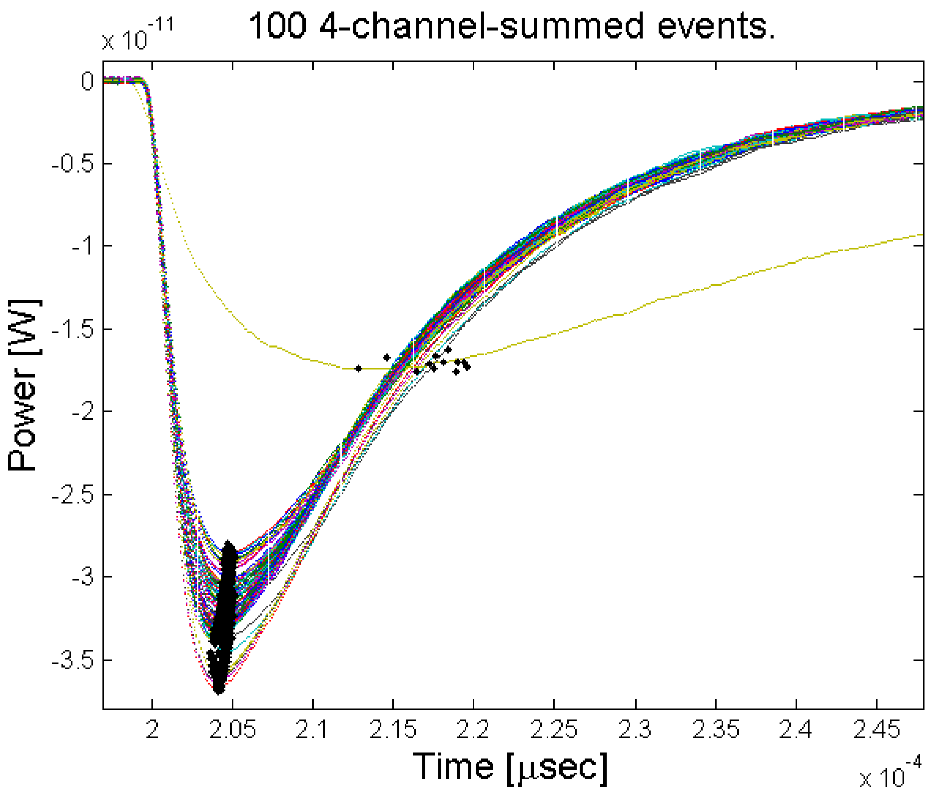

Figure 7.3: 2×2 "split"-TES X-ray pulses. The K_α and K_β bands are not well separated through out the pulse recovery.

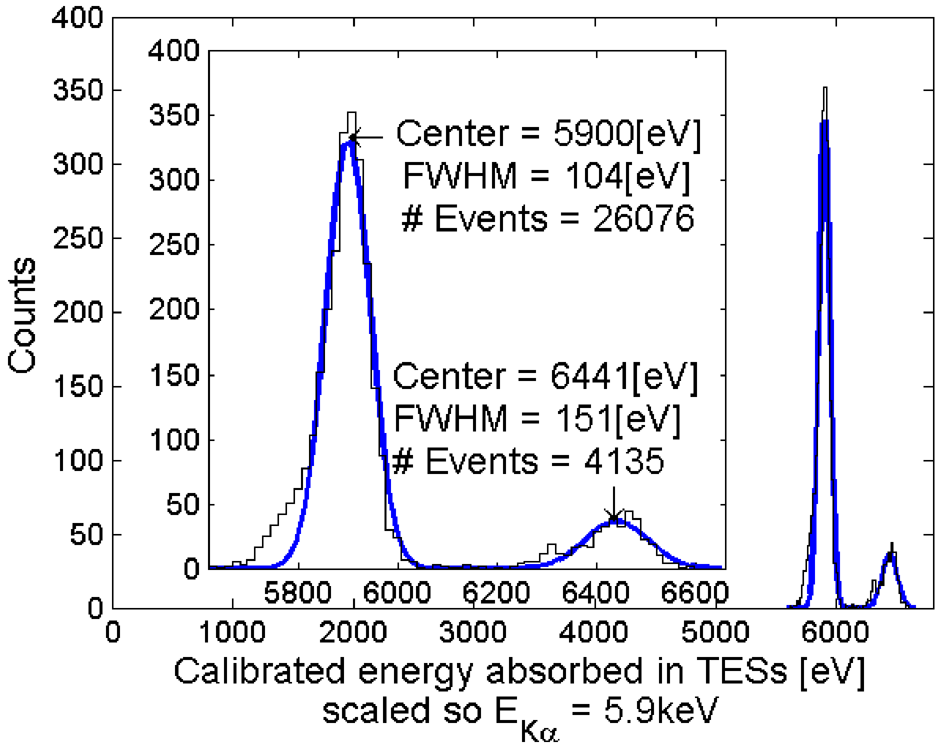

Figure 7.4: 2×2 "split"-TES histogram. Pulse shape cuts and corrections have not been applied.

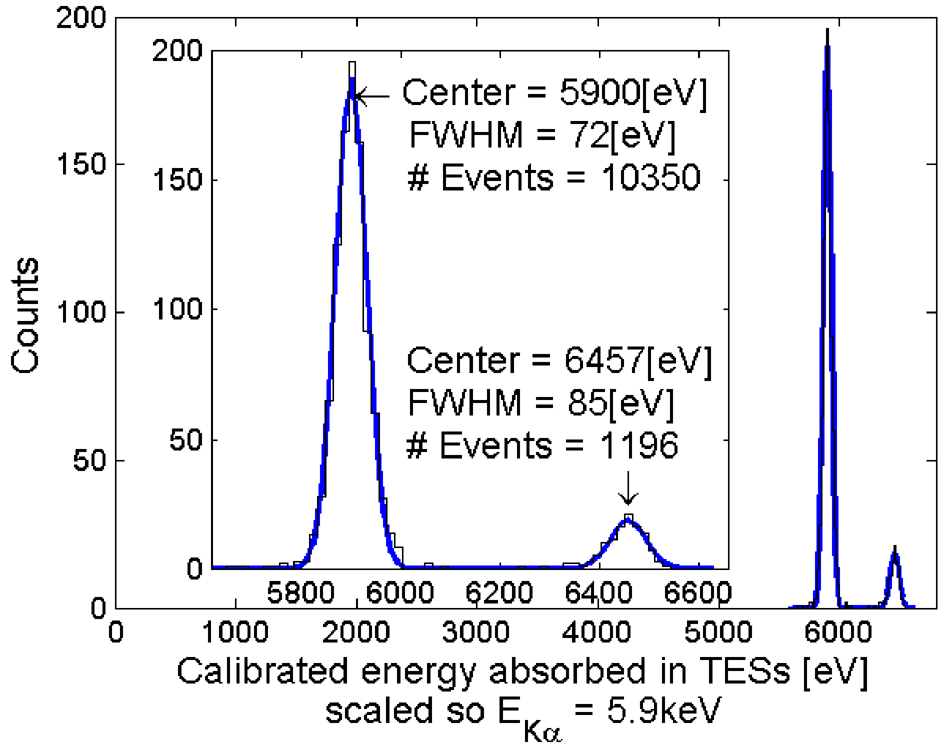

Figure 7.5: 2×2 “split”-TES histogram. Pulse shape cuts and corrections have been applied.

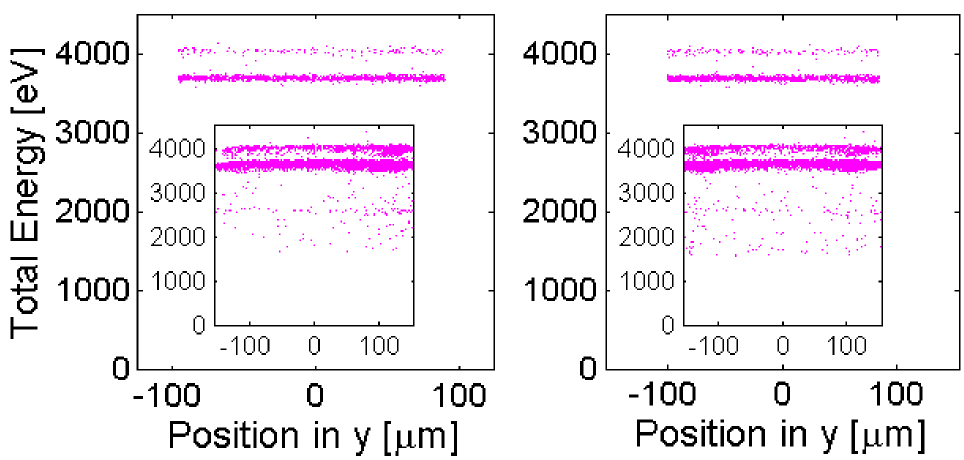

Figure 7.6: 2×2 "split"-TES X-ray position. The inset shows the data before cuts and corrections are applied and the silicon escape peak is clearly evident.

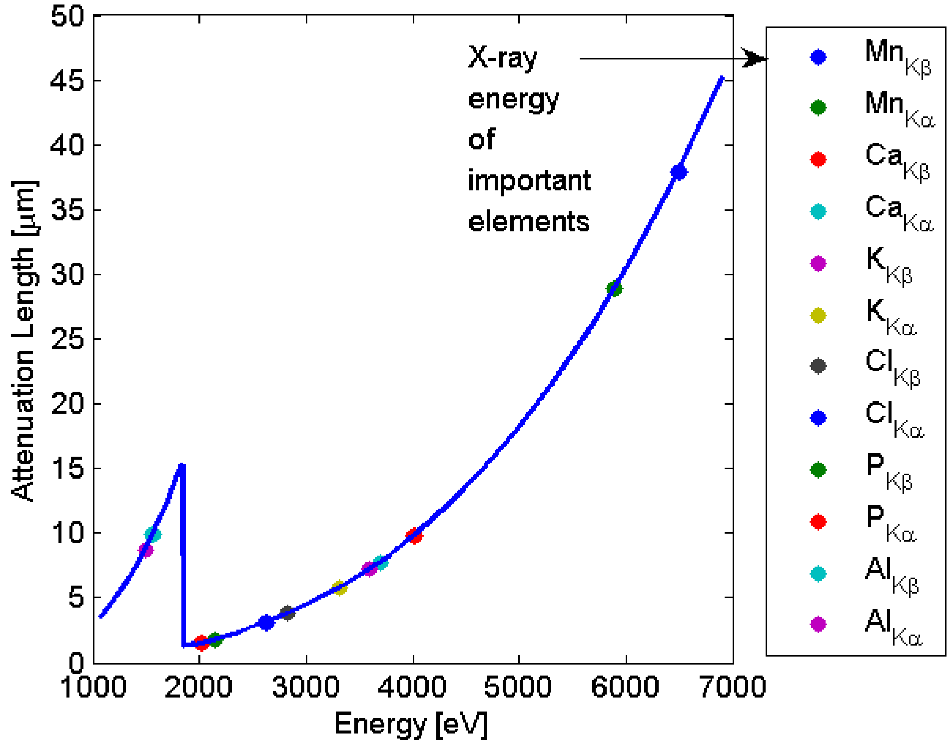

Figure 7.7: X-ray attenuation length in silicon for fluorescing materials. Shown is the general curve and selected points for those lines in our fluorescence scheme. The jump at 1.74 keV corresponds with the silicon K-edge.

height were only 250 μm (compared to the 350 μm height. This aspect ratio of course will make position determination less precise and position corrections will be less helpful. While the energy resolution left something to be desired, we were able to perform stoichiometry on a vitamin supplement (see Figure 7.9). The potassium and chlorine ratios are correct within $\sim$ 10%. A base component of the pill, calcium phosphate seems to have the stoichiometry Ca_2P. Amusingly, this supplement is sold as potassium chloride; the calcium phosphate seems to be more dominant.

We see that we are in a good position to continue on with this fluorescence scheme. A wider detector has been $^{56}Fe^{+}$ implanted to reduce phase separation and will be run soon.

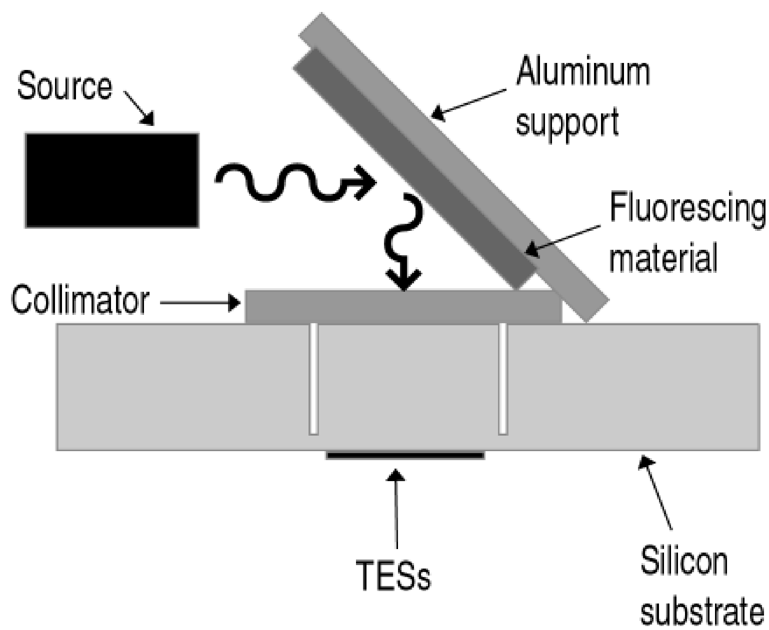

Figure 7.8: Fluorescing scheme setup. X-rays are incident on fluorescing material which produces lower energy lines. The increased distances from the source to the detector along with the low probability of fluorescing necessitates a stronger source to maintain count rate.

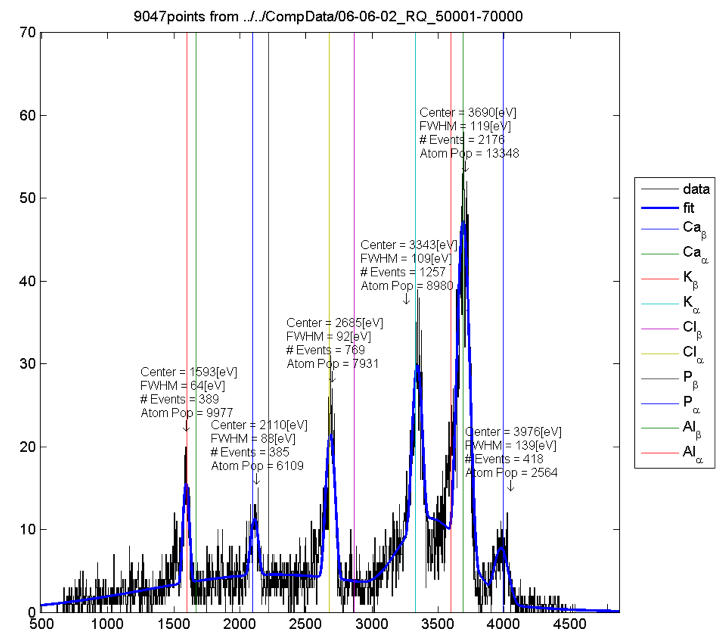

Figure 7.9: Fluoresce stoichiometry for a potassium chloride vitamin supplement. The potassium and chlorine ratios are correct within $\sim 10\%$. A base component of the pill, calcium phosphate seems to have the stoichiometry Ca_2P.

Chapter 8

Discussion of Energy Resolution

I conclude this thesis with a discussion of energy resolution and propose a next generation detector that might perform better.

8.1 Electron-Hole Contribution

As a review, when X-rays are absorbed, electron-hole pairs are produced (this description is incredibly abbreviated and skips many of the fundamental processes, see Section 2.6 for a more detailed discussion). They require on average 3.81 eV [4] of energy for their production. Their fluctuation however is not Poisson, but modified by the Fano factor [47] and is given by

$$\sigma = \sqrt{FE/\epsilon_0},$$

where E is the absorbed energy, ε_0 is the quantization energy and F is the Fano factor. These electron-hole pairs shed phonons until they reach the velocity of sound in the crystal and their gap energy ~1.2 eV dominates. The associated fluctuation in energy is

$$\sigma = 1.2[\text{eV}]\sqrt{FE/\epsilon_0}.$$

For the detectors that have 220 μm deep trenches there is a $\sim$ factor 2 calibration correction in the detector and a factor of $2\sqrt{2 \times \log 2} = 2.355$ to convert to FWHM. The final variation that we expect to see in the electron-hole system is

$$\Delta E_{FWHM} = 2.355 \times 2 \times 1.2[\text{eV}]\sqrt{FE/\epsilon_0}.$$

Given a Fano factor of F=0.116 [48], and an incident energy of E=5.9 keV we obtain

$$\Delta E_{FWHM} = 2.355 \times 2 \times 1.2[\text{eV}]\sqrt{0.116 \times 5900[eV]/3.81[eV]} = 75.8[eV].$$

Obviously this value is very close to what we have seen in the 2-d detector discussed in Section 6. In fact if we consider adding the baseline noise in quadrature with this electron-hole pair statistical variations then we expect

$$\Delta E_{FWHM} = \sqrt{(75.8\ eV)^2 + (36.6\ eV)^2} = 84.1\ eV,$$

higher than the measured variation $\Delta E_{FWHM} = 80\ eV$. There are three reasons that could lead to a lower value being seen in practice. First, the work that we performed could be giving a more accurate, lower value for the Fano factor. The correction would be quite small and value of $F = 0.103$ would be sufficient. A second explanation could come about from reduced phonon noise as the detector's resistance increases (see Section 5.3.2). A reduction of the detector's noise contribution from 36.6 eV to 26 eV would also explain the reduced noise that we see. The third reason is closely related to the second. The excess noise discussed in Section 5.3.2 increases with $\alpha = \frac{T}{R}\frac{dR}{dT}$, which decreases at higher operating resistances. Regardless of the exact reason for seeing a better energy resolution than expected, the two values are in close agreement. The assumption in this model is that none of the electron-hole pairs recombine during the pulse acquisition time. There is some additional evidence to support this idea.

The 220 μm and 330 μm trenched detectors have TES absorption ratios of 49% and 69% respectively. If we extrapolated this absorption ratio to a detector that was completely trenched then we would expect 76% of the energy to be read out by the TESs. This value is close to the 68% that is initially released into the phonon system.

Therefore, the implication is that charges are trapped and not releasing their energy into the phonon system. This is consistent with the charge trap density discussions in Section 2.6. If correct, then it is necessary to recover the electron-hole energy. The simplest solution as suggested in Section 2.6 is to use a purer crystal.

8.2 Phonon Contribution

To be complete, I show the contribution that phonons would provide to the energy resolution. The assumption here is that all the initial X-ray energy is released into phonons within the detector's acquisition time. Our detectors have been made on 350 μm thick silicon crystals. Most of the energy is carried in the transverse acoustic phonon modes which have a velocity of 5900 m/s and take $\sim 5.9 \times 10^{-8}$ seconds to propagate across the crystal. If we let $\Gamma = (5.9 \times 10^{-8}[s])^{-1}$ and solve for the frequencies $\Gamma_A = A\nu_A^5$ and $\Gamma_I = B\nu_I^4$ (see Chapter 3) we find $\nu_A = 3$ THz and $\nu_I = 1.6$ THz. From simulation, we expect ~1 THz to be a more characteristic answer, but this approximation will not greatly effect the result. For these purposes we pick the larger quantization energy. Converting to energy $E_\varphi = h\nu$ where $h = 4.1 \times 10^{-15}$ eV s is Planck's constant we find a characteristic energy $E_\varphi = 0.012$ eV. This time the phonon losses would be due to losses to the environment and independent of each other*. The expected energy fluctuation is

$$\Delta E_{FWHM} = 2.355 \times 2\sqrt{E_{loss}\epsilon_0}.$$

Plugging in the numbers $E_{loss} = 3$ keV and $\epsilon_0 = 0.012$ eV we get $\Delta E_{FWHM} = 14$ eV (this value would of course be improved in a detector that had deeper trenches and less phonons escaping to the environment). If we went with the 1 Thz quantization energy this value would be slightly smaller. These rough calculations are in close agree with simulation which shows a ~9 eV effect. The difference due to a more precise

*The assertion of independence is not necessarily correct. If the losses were dominated by a few higher energy phonons then the statistics would change. In this case, a factor analogous to the Fano factor would be introduced into the energy full-width-half-maximum formula. Precise studies like this are complicated however, and are not performed here.

and correct spread in phonon energies. Obviously when considered in quadrature with another noise source, 9 eV is a very small component of the 70–80 eV FWHM that we are seeing. Therefore, it is unlikely that a phonon contribution is the source of the degraded energy resolution.

Chapter 9

Next Generation Detector

Here I propose a next generation detector which could be useful for numerous reasons.

As discussed in Section 8.1, the detector's performance is likely degraded due to electron-hole pairs being trapped and not releasing their gap energy to the phonon system. It is expected that using purer silicon crystals will be a quick and simple way to avoid this loss.

We might, however, find that there are residual position dependent charge and phonon losses in the detector's z direction. We could resolve the X-ray's position in all three dimensions by creating a detector with TESs on both sides of the detector (see Figure 9.1). This scheme would allow position corrections and cuts in all three dimensions. This scheme would become more important if this detector concept were applied to the detection of high energy X-rays. High energy X-rays have a longer attenuation length and are not absorbed in the crystal's surface layer as are low energy X-ray's. Therefore, it will be necessary to make position corrections in all three dimensions.

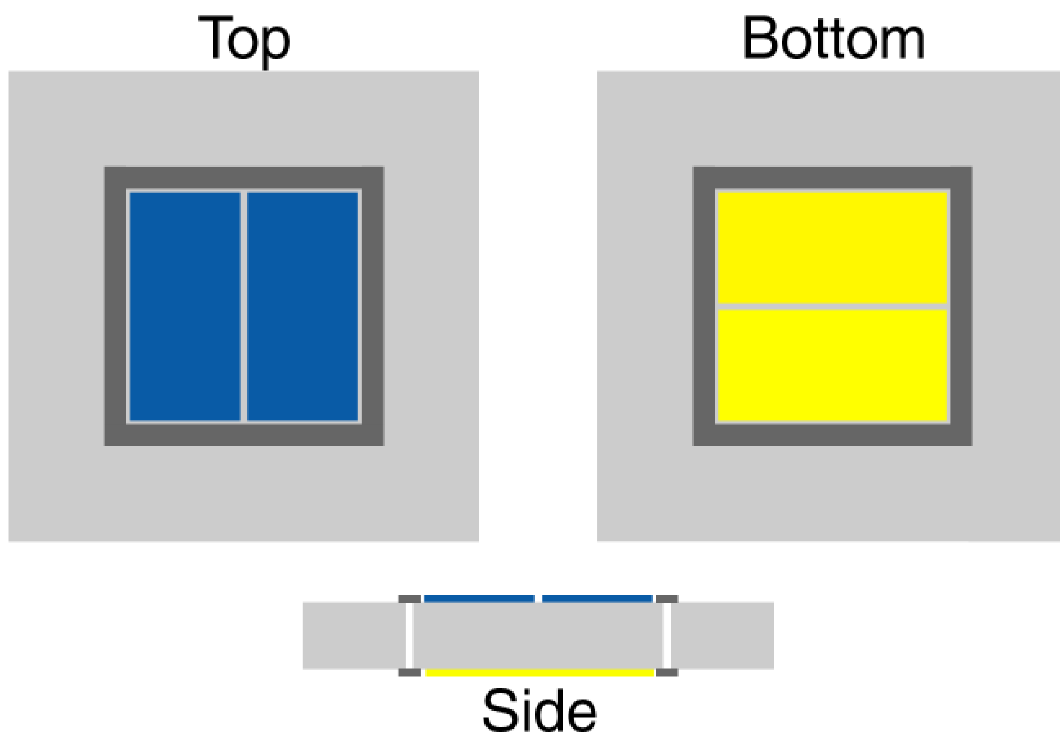

Figure 9.1: A proposed next-generation detector. An electric field could be set up between the top and bottom TESs to sweep charges into the TESs. This detector would also be able to resolve the incident X-ray's position in all three dimensions.

Appendix A

Substrate Temperature Fluctuation Noise

A.1 Introduction

Variations in the substrate temperature while acquiring X-ray data can lead to broadening in line spectra. Of course, the best method for avoiding this degradation is a stable refrigerator. Generally however, I have preferred to run the KO-15 without the use of temperature controlling heaters simply because I do not want them to provide a source of noise during the acquisition. Therefore, as a first step, it is required that the refrigerator is allowed several hours (generally overnight) to settle into its base temperature. Next, it is advisable to limit data acquisition periods to avoid long time period (few hours) fluctuations. In general, neither of these constraints are difficult to satisfy.

A.2 Noise Theory

I haven't seen in a thesis yet where someone derived the theoretical noise contribution from a time varying substrate temperature. The case where the TES is in thermal equilibrium with the substrate is fairly simple... We note the thermodynamic equation

$$P = \frac{V^2}{R(T)} = \frac{dE}{dt} = k\left(T_{TES}^n - T_{substrate}^n\right),$$

where K is a thermal coupling constant. In thermal equilibrium, the relationship between substrate temperature variations and the induced variations in the TES electron system are found by differentiating

$$\frac{V^2}{R(T)} = k\left(T_{TES}^n - T_{substrate}^n\right),$$

to obtain

$$\left(knT_s^{n-1}\right) dT_s = \left(knT^{n-1} + \frac{V^2}{R}\frac{1}{T}\frac{T}{R}\frac{dR}{dT}\right) dT.$$

We now make the typical substitution $\alpha = \frac{T}{R}\frac{dR}{dT}$ and also $k = \frac{V^2}{R}\left(T^n - T_s^n\right)$ to obtain

$$\left(\frac{nT_s^{n-1}}{T^n - T_s^n}\right) dT_s = \left(\frac{nT^{n-1}}{T^n - T_s^n} + \frac{\alpha}{T}\right) dT.$$

This equation can now be rearranged into a more useful form

$$dT = \left(\frac{T_s}{T}\right)^{n-1}\left[\frac{1}{1 + \frac{\alpha}{n} - \left(\frac{T_s}{T}\right)^n \frac{\alpha}{n}}\right] dT_s.$$

That was step one, next we need to find how power varies with substrate temperature variations by differentiating

$$P = k\left(T_{TES}^n - T_{substrate}^n\right),$$

to obtain

$$dP = kn\left(T_{TES}^{n-1} dT - T_{substrate}^{n-1} dT_s\right).$$

We can now use the previous result relating dT and dT_s in addition to making the substitution $k = \frac{P}{T^n - T_s^n}$ to obtain

$$\frac{dP}{P} = n\left(\frac{T_s}{T}\right)^{n-1}\left[\frac{1}{1 - \left(\frac{T_s}{T}\right)^n}\right]\left[\frac{1}{1 + \frac{\alpha}{n} - \left(\frac{T_s}{T}\right)^n \frac{\alpha}{n}}\right]\frac{dT_s}{T}.$$

And last but not least, we substitute $\frac{dE}{E} = \frac{dP}{P}$.

$$\frac{dE}{E} = n\left(\frac{T_s}{T}\right)^{n-1}\left[\frac{1}{1-\left(\frac{T_s}{T}\right)^n}\right]\left[\frac{1}{1+\frac{\alpha}{n}-\left(\frac{T_s}{T}\right)^n\frac{\alpha}{n}}\right]\frac{dT_s}{T}$$

A.3 Simulation

The equation above can be verified with a quick simulation. A time varying substrate temperature is randomly generated. The physical model is a substrate coupled to a fixed temperature bath with some conductance G_{sb}. The substrate temperature is then randomly kicked (in both positive and negative directions). The magnitude of the kick determines the deviation in substrate temperature, while the C/G time constant determines how rapidly the substrate return to the bath temperature. In practice, the substrate temperature kick is found by trial and error such that the standard deviation in T_s is what is desired.

The output of a sample run at 20 mK is shown (see Figure A.1). The plot is not very insightful but if we find random, non-overlapping intervals to perform integration over power, we can calculate both the mean and variance in the detector's Joule energy. We can vary the substrate temperature and repeat the process to see that the theory and simulation agree (see Figure A.2). The simulation and theory used a 1 mK variation in the substrate temperature. There is good agreement between the two except at higher substrate temperatures. This disagreement is due to the TES saturating and therefore its resistance does not vary with the varying substrate temperature. Also, a constant α (determined at T_s =35 mK) was assumed in the theory, which is not true at higher temperatures.

One may wonder if the noise contribution is due to the temperature fluctuations during the energy integration or due to variations in the current baseline. These two effects are easy to separate in simulation (see Figures A.3 and A.4). We can tell by comparing simulation against theory that in fact the noise is due to the varying baseline. This observation of course is to be expected since the variation in substrate temperature is relatively small during the integration window.

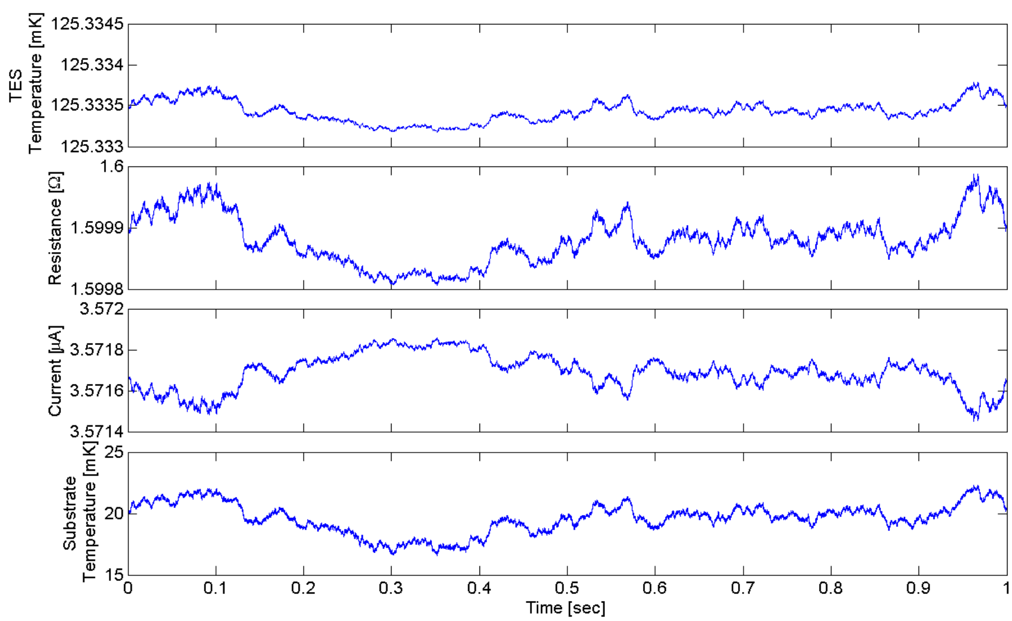

Figure A.1: Time varying substrate temperature with 20 mK baseline. The substrate temperature has a standard deviation of 1 mK. Shown are the TES's temperature, resistance and current along with the substrate temperature. The TES's time constants are short compared to the substrate temperature's long time constant.

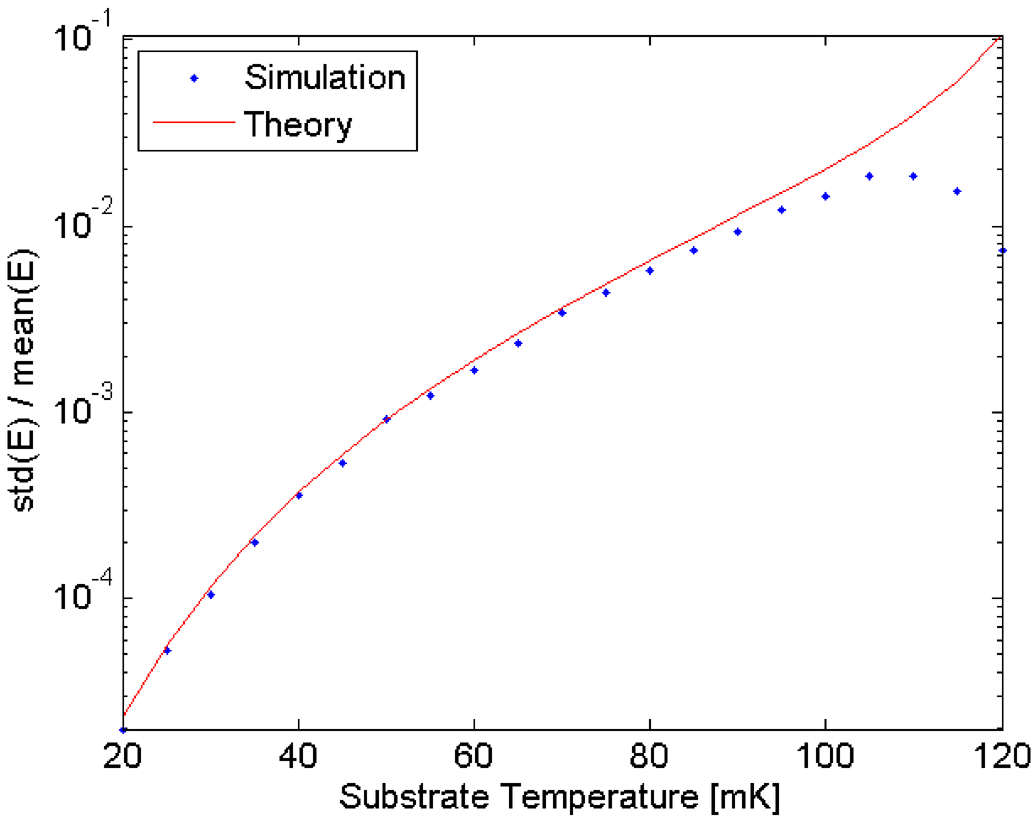

Figure A.2: Substrate temperature fluctuation contribution to thermal equilibrium TES noise. The simulation and theory used a 1 mK variation in the substrate temperature. There is good agreement between the two except at higher substrate temperatures. This disagreement is due to the TES saturating and therefore its resistance does not vary with the varying substrate temperature. Also, a constant α (determined at T_s =35 mK) was assumed in the theory, which is not true at higher temperatures.

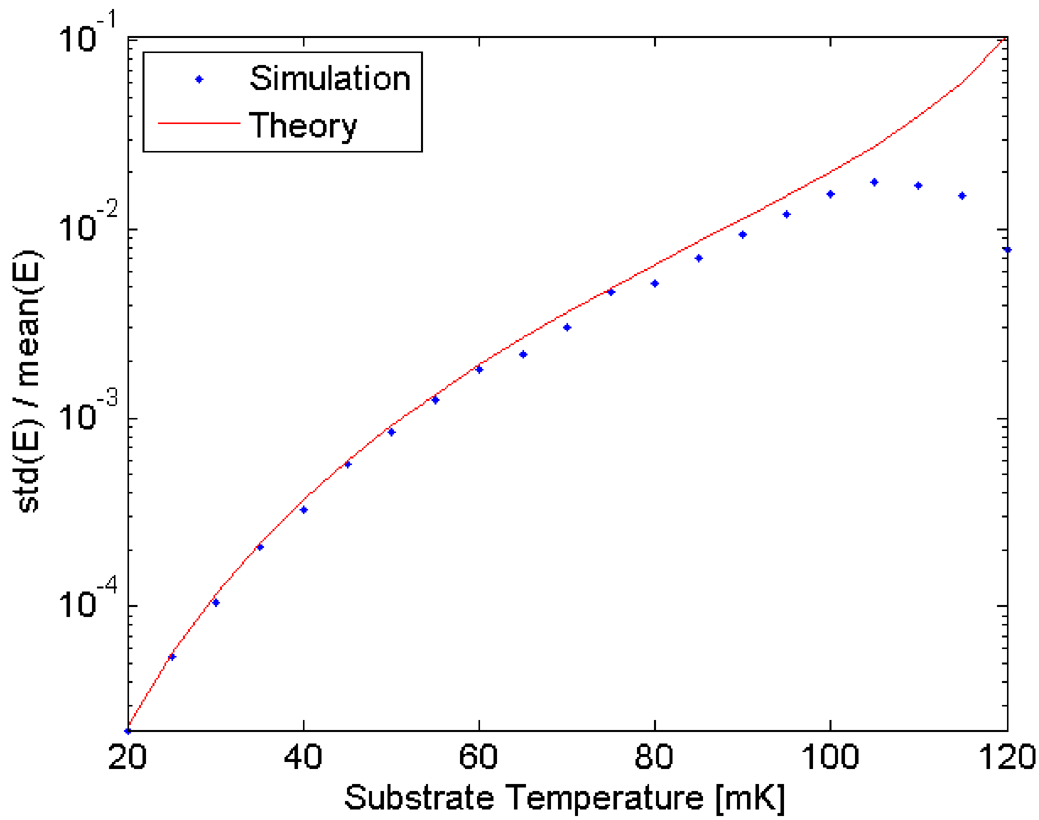

Figure A.3: Substrate temperature fluctuation contribution to thermal equilibrium TES noise. The substrate temperature was held fixed during the integration window. This restriction ensured that only the current baseline could vary. The agreement between simulation and theory is good showing that the baseline variation is what contributes to the noise.

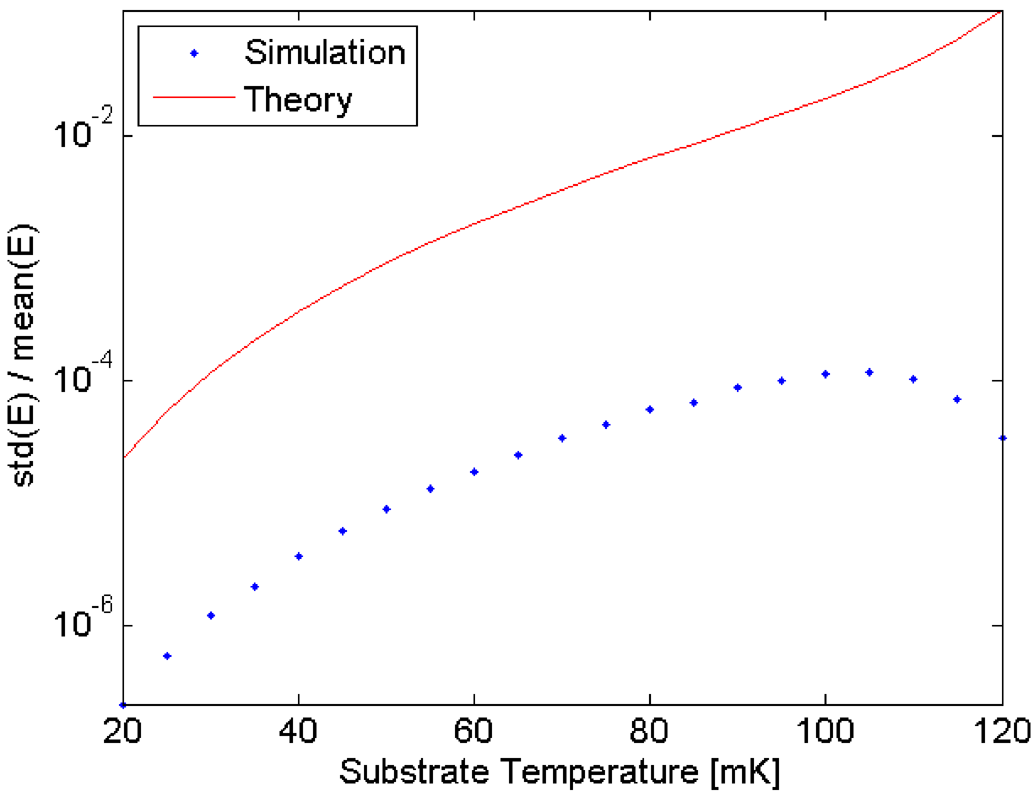

Figure A.4: Substrate temperature fluctuation contribution to thermal equilibrium TES noise. In the simulation, the substrate temperature is returned to the mixing chamber temperature well before the integration window. The substrate temperature is then allowed to vary during the integration window. This restriction allows the substrate temperature to vary only slightly between different integration windows. The poor agreement between simulation and theory confirms our assumption that this effect is not the dominant source or noise.

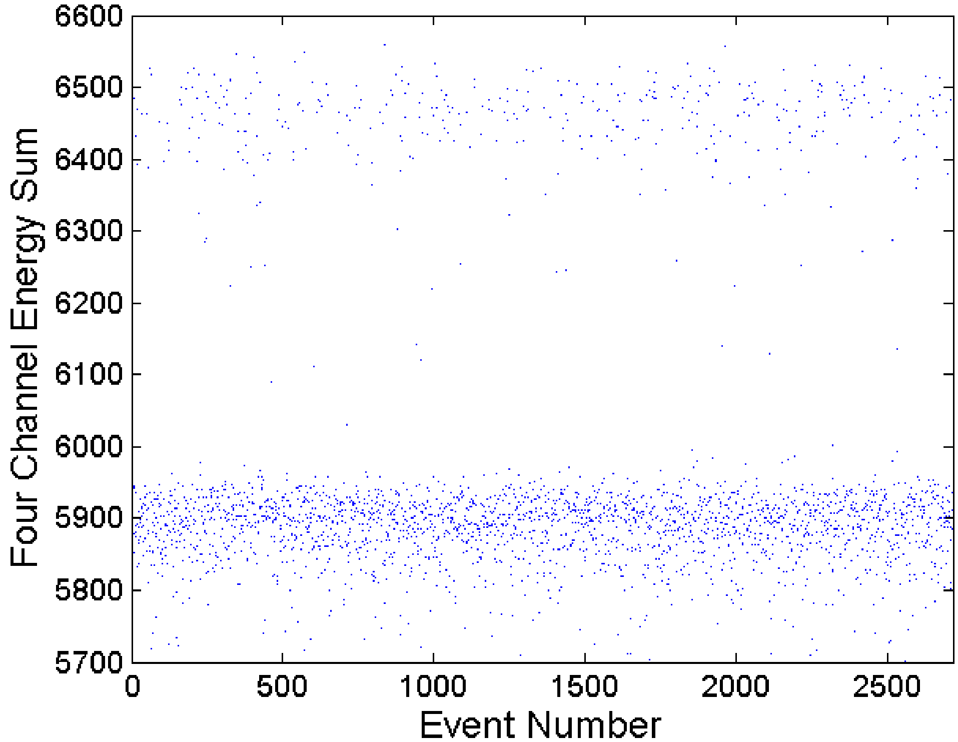

Figure A.5: 2 × 2 TES four-channel summed energy vs. time plot. This is the same data that produced Figure 6.5. We see can clearly distinguish the K_α and K_β lines. The line-width and mean energy do not vary with time.

A.4 Data

Finally, we can see that in practice this effect does not contribute significantly to our detector setup. Shown in Figure A.5 is the four-channel-sum collected energy versus time for the 2 × 2 detector discussed in Chapter 6.

Appendix B

Phase Separation

B.1 Introduction

Some X-ray and heat pulses show kinks or wiggles during pulse recovery that cannot be explained with a mean field approximation for the TES temperature and resistance. The studies in this section were motivated by trying to understand if these features could explain the energy degradation in the detector but we quickly decided that this explanation was unlikely. However, I continued the study this out of personal interest. Regardless of the reason, I present this work in hope that it will be of value to a reader who is trying to understand such features in their traces.

We start by running the X-ray detector. By changing bias conditions, electrothermal oscillations can be ruled out. Inter-pixel cross talk and other electronics ringing are also quickly ruled out. The wiggle intensity seems to be correlated with substrate temperature. To solve this mystery, simulations are run and partial phase separation could provide an explanation for this effect.

This phase-separation study was performed in two dimensions while previous studies in our group were restricted to one dimension. We will see that phase separation is not suppressed along the current flow direction for a two dimensional TES. It is however avoided in the direction perpendicular to current flow.

B.2 Methodology

The data shown here are for two TESs contained in an X-ray detector like that shown in Chapter 6. The other two TESs did not show interesting features and are not included in this discussion. In general these wiggles can be seen in both X-ray pulses and heat pulses. Also, they are observed in all four SQUIDs during different runs. Here I focus on traces created by heatpulses which can be repeated and varied in a controllable fashion. These heatpulses are sent directly through the TES bias line, increasing its temperature and operating resistance.

B.2.1 Pulse Duration Dependence

First we show traces at a constant mixing chamber temperature and constant bias voltage and vary only the duration of the heatpulse. The first thing that we notice is the change in TES recovery time which is likely due to heating the substrate during the longer duration pulses. We notice that the wiggles occur at roughly 100 μs after the TES leaves the saturated state (see Figures B.1 and B.2). Due to the varying amount of energy injected into the TES, there is a varying amount of time that the TES is in the saturated state. Hence, we can safely rule out a ringing in the generator as a cause of the wiggles. If the generator was ringing and caused the wiggles then we would expect to see it occur at a constant time after the function generator's pulse, not at a constant time in the recovery. By the same explanation, we can rule out any oscillations in the bias or readout circuit due to the sharp leading edge of the traces.

Additionally, we see a combination of both a kink and wiggle in the some of the traces. However we never see a combined total of two of these features. This observation is discussed in Section B.5.

We also observe that crosstalk induced wiggles are unlikely as the time delay between the channel 4 and channel 3 wiggles are delayed by $\sim$50 μs. More evidence suggesting that the wiggles are not a crosstalk effect is presented in Section B.2.2.

Another very interesting observation is that the wiggle does not occur at the same current in the recovery. This observation rules out any effects that exist purely in the bias and readout circuit. Already it seems unlikely that electrical effects are responsible, which leaves thermal effects.

B.2.2 Pulse Duration Dependence / Reduced Amplitude

Next, we reduce the pulse amplitude compared to the Section B.2.1 data set (see Figures B.3 and B.4). We still notice the increased recovery time that corresponds with longer pulse times. Otherwise, we go through the same procedure of varying the pulse duration while holding the substrate temperature and bias voltage constant. We notice that the wiggles still occur at the roughly the same time in the trace recovery.

The briefly pulsed 900 kHz wiggle in channel 4 is definitely suppressed though. In the previous set (see Section B.2.1), the peak was 95% of saturation and phase separation was evident. With the reduced pulse amplitude, the peak value is only 90% of saturation and the wiggle has been replaced by a less dramatic kink (I am comparing the 900 kHz traces seen in Figures B.2 and B.4). This observation suggests that wiggles and kinks share some fundamental connection and that pulses have to become close to saturation for them to wiggle.

Furthermore, comparison of the data in this section and Section B.2.1 suggests that the wiggles are not due to a crosstalk issue. Consider again the 900 kHz traces in this section and the previous section (see Figures B.1 and B.2) data set. The channel 3 traces look very similar while the channel 4 traces show much (no) wiggling for the large (small) amplitude pulses. If we believed that the channel 4 wiggles were caused by crosstalk, induced by channel 3 then we would expect the wiggle in channel 4 to remain constant, which it does not.

B.2.3 Refrigerator problems

Unfortunately at this point the refrigerator crashed and I was forced to warm up and rerun the devices.

The interesting channels have now switched from channels 3 and 4 to channels 2 and 4. Later I hypothesize a reason for the effect varying on different runs. Let us continue and see what other parameters we can vary and hence learn from.

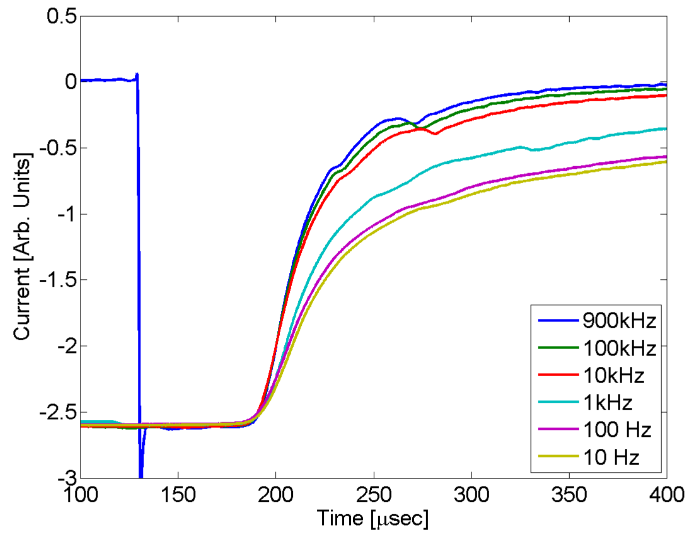

Figure B.1: Pulse duration dependence, channel 2.

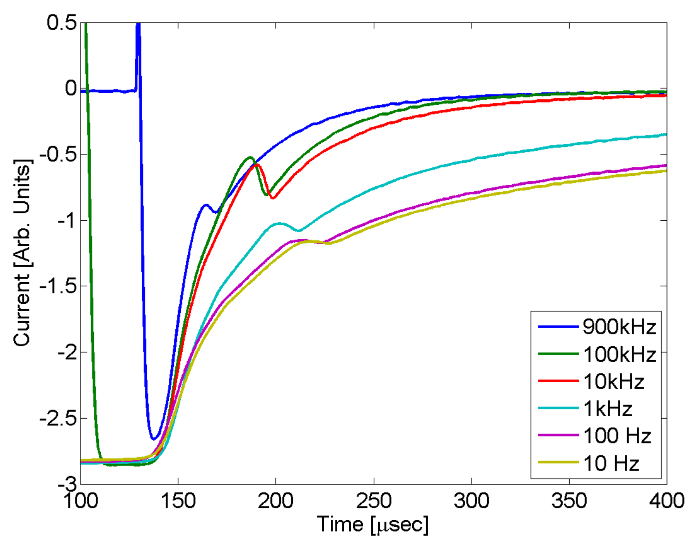

Figure B.2: Pulse duration dependence, channel 4. The wiggles are more dramatic in this TES. The longer decay times for the longer pulse duration is a recurring theme and suggest the substrate has been heated by the longer pulse times. Also, many of the traces show a combination of two kinks / wiggles.

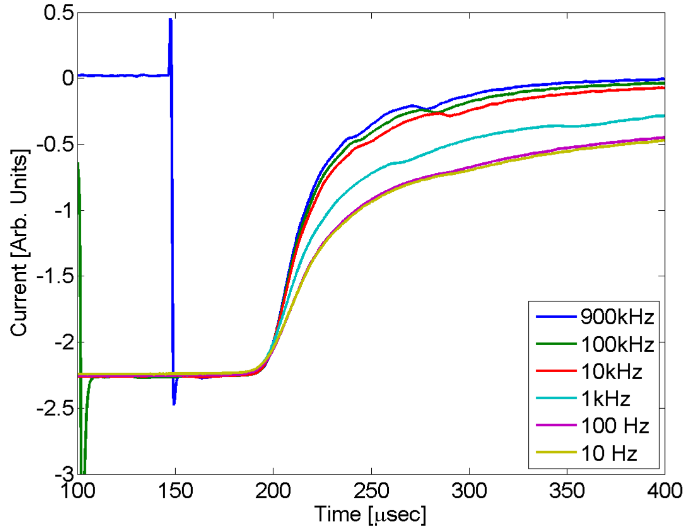

Figure B.3: Pulse duration dependence, reduced bias voltage, channel 3.

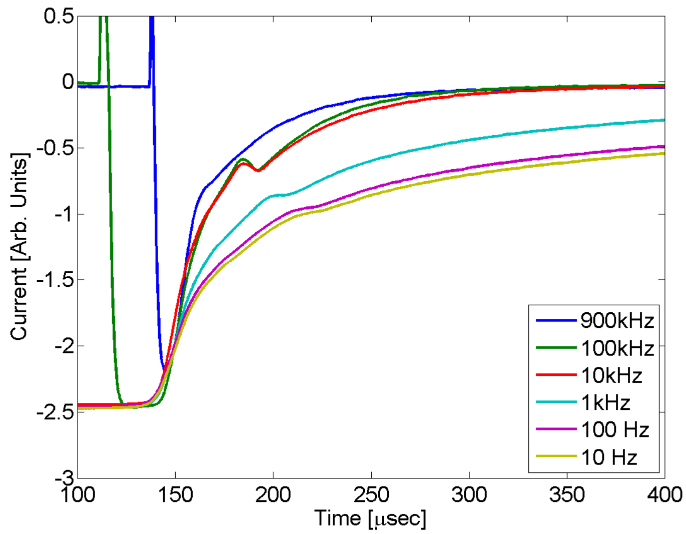

Figure B.4: Pulse duration dependence, reduced bias voltage, channel 4. The same themes are seen here as in Figures B.1 and B.2. It is noticeable that the lower energy (900 kHz) pulse does not show as dramatic an effect as in Figure B.2 which is consistent with the observation that there is a minimum threshold energy required to observe the wiggle / kink effect.

B.2.4 Reversed Polarity

Perhaps one of the most important tests is to reverse both the bias and pulse polarities to see if electrical oscillation is an obvious cause (see Figures B.5 and B.6). Again, the different time constants and wiggles are evident. If the pulse recovery is flipped, but the wiggle direction remains the same, then we would conclude that electrical effects brought about the wiggles. As this effect is not seen, we continue to investigate thermal effects as a source of the wiggles.

B.2.5 Substrate temperature dependence

Next we plot channel 2 and 4 traces while incrementally warming the mixing chamber. The temperatures 39.2, 42.8, 47.0, 52.0, 58.0, 65.4, and 74.6 mK allow a broad range in substrate temperatures. The plots are grouped by heat pulse frequency (see Figures B.7, B.8 (900 kHz), B.9, B.10 (100 kHz), B.11, B.12 (10 kHz), B.13, B.14 (1 kHz), B.15, B.16 (100 Hz), B.17, B.18 (10 Hz) and B.19, B.20 (1 Hz)). The injected heat dependence, at constant temperature, is similar to that shown in Sections B.2.1 and B.2.2 and is not shown for this data set.

The channel 4 traces show very obvious wiggles. However, at 900 kHz (see Figure B.7), the wiggles are not evident. Again it seems that some minimum threshold of energy must be injected before the wiggles are evident. Perhaps it is necessary to raise the resistance beyond some threshold value.

At 100 kHz (see Figure B.9) the injected energy is sufficient to produce wiggles in the low temperature traces. However, we notice that the wiggles are almost suppressed at 65.4 mK and are fully suppressed at 74.6 mK. At 10 kHz (see Figure B.11) we notice that the wiggles start becoming suppressed at 58.0 mK and are fully suppressed at 74.6 mK. At 1 kHz (see Figure B.13) we notice that the wiggles are fully suppressed at 65.4 mK, a trend that continues through to 1 Hz.

The channel 2 traces however do not show these wiggle features. Instead they show kinks which are shown in Section B.3.1 to be related to the wiggles. At lower pulse energies of 900 kHz, 100 kHz and 10 kHz (see Figures B.8, B.10 and B.12) no kinks are evident; the TESs have a single decay-time-constant. This channel

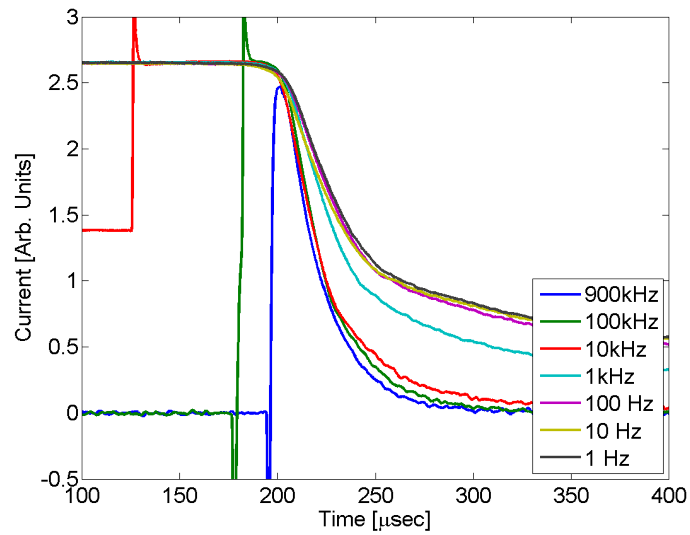

Figure B.5: Reversed polarity, channel 2.

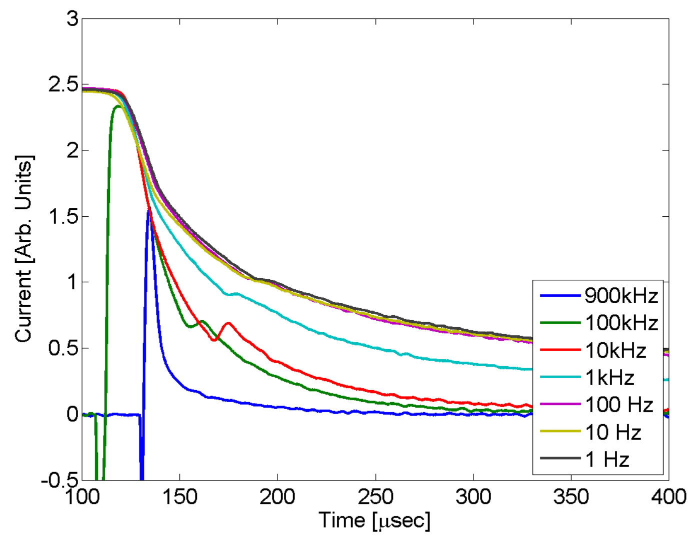

Figure B.6: Reversed polarity, channel 4. The bias and pulse polarities have been reversed to consider electrical effects. The longer decay times are still evident at higher pulse energies. The wiggles are also clearly evident in channel 4. If the wiggles went the opposite direction then an electrical effects would be very suspect.

evidently has a higher threshold energy before wiggles are seen. At higher pulse energies (1 kHz, 100 Hz, 10 Hz and 1 Hz) however there are noticeable kinks in the traces (see Figures B.14, B.16, B.18 and B.20) that are obvious in all traces except possibly those at highest substrate temperature where they are suppressed. The threshold energy required for both the wiggle and kink feature onset along with the change in decay time constants that the wiggles and kinks produce strongly suggests that the effects are very closely related and probably manifestations of the same physical phenomenon.

B.2.6 Bias Voltage Dependence

Next, we explore how the bias voltage changes the wiggle (see Figures B.21 and B.22). We notice the wiggles are suppressed at $\leq$-560 mV (biases in the previous data sets were at -430 and -320 mV and a lower bias results in *more* power being applied at the quiescent mode). Perhaps the suppression is due to the higher bias conditions heating the substrate.

B.2.7 Amplitude Dependence

Now we hold the bias voltage constant and vary the pulse amplitude (see Figures B.23 and B.24). Again, the TES has to have some minimum amount of energy injected before wiggles are evident. There is however some optimal amount of energy for maximizing the wiggles. Beyond that they decrease but are not suppressed.

B.2.8 Use Channel 2 to Heat Substrate

We can keep the bias and injected heat on channel 4 constant and vary the bias of channel 2 to vary the substrate temperature (see Figures B.25 and B.26). No heat pulses are injected into channel 2. Again we see that at high substrate temperatures the wiggle is suppressed. Furthermore, since there was no effect seen in the channel 2 trace that was associated in time with the wiggles in channel 4, it is unlikely that the wiggles are due to an electrical crosstalk issue.

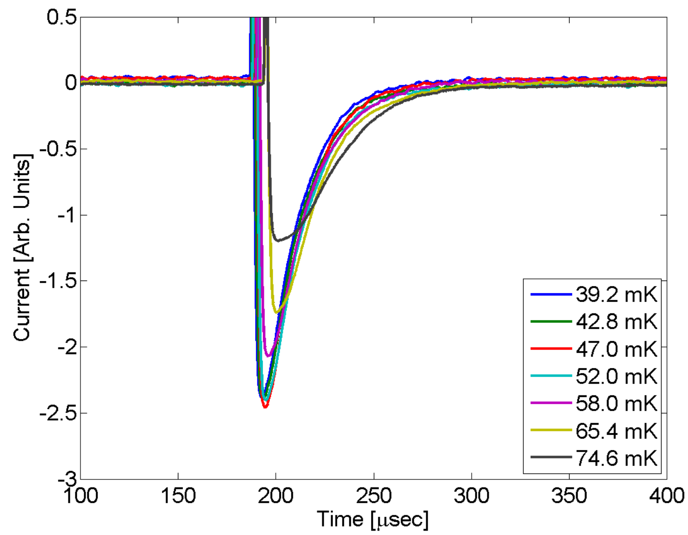

Figure B.7: Substrate temperature dependence, 900 kHz, channel 2.

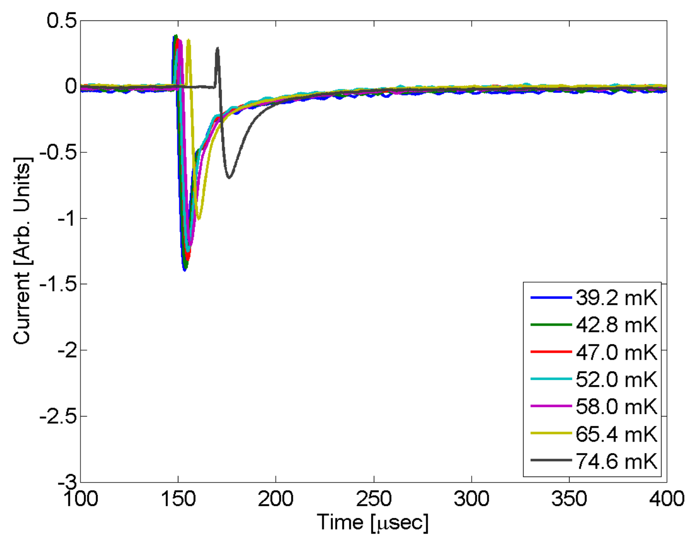

Figure B.8: Substrate temperature dependence, 900 kHz, channel 4. The pulse energy has not surpassed some minimum threshold value. Kinks or wiggle are not evident and there seemingly is one decay time.

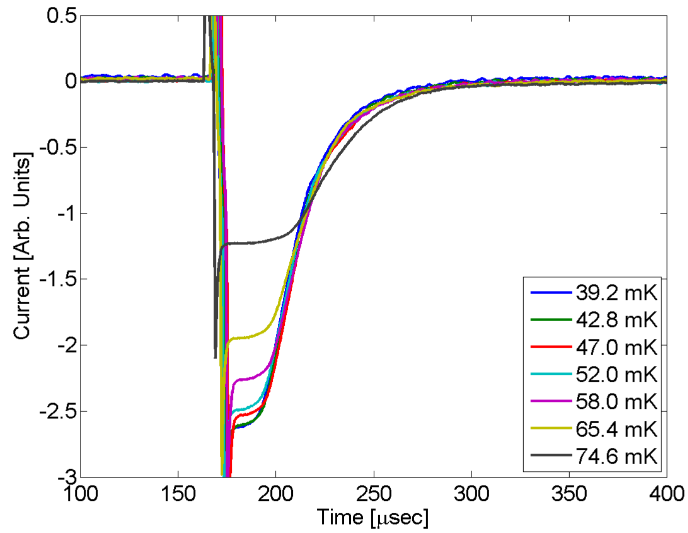

Figure B.9: Substrate temperature dependence, 100 kHz, channel 2.

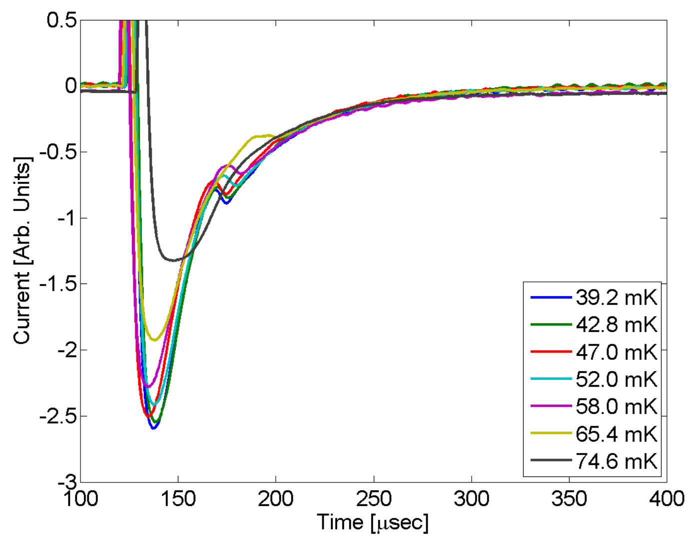

Figure B.10: Substrate temperature dependence, 100 kHz, channel 4. The wiggles become evident in channel 4.

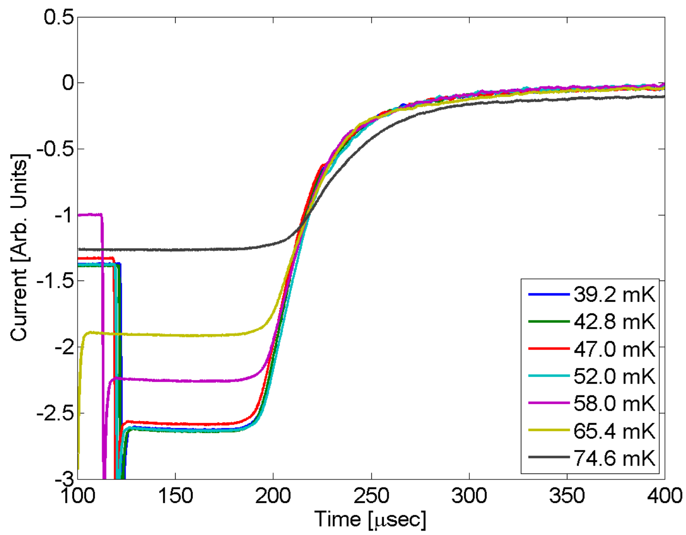

Figure B.11: Substrate temperature dependence, 10 kHz, channel 2.

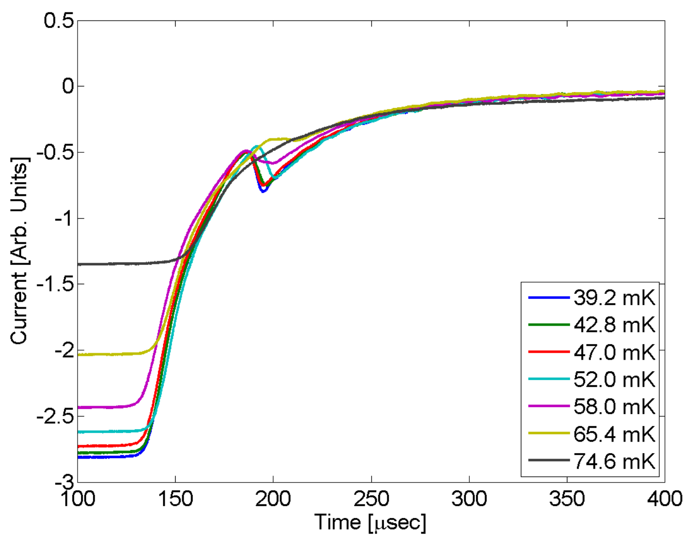

Figure B.12: Substrate temperature dependence, 10 kHz, channel 4. There is no noticeable change from the 100 kHz data.

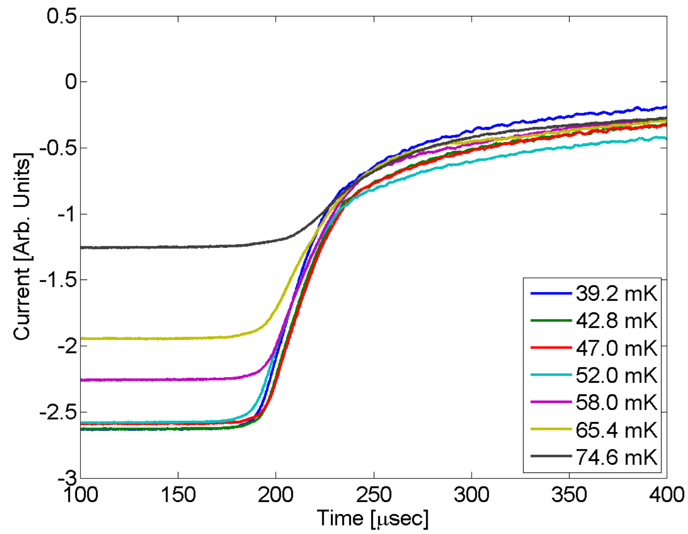

Figure B.13: Substrate temperature dependence, 1 kHz, channel 2. By eye we can see that we now have (at least) two time constants. Hence, a kink at 23 μsec.

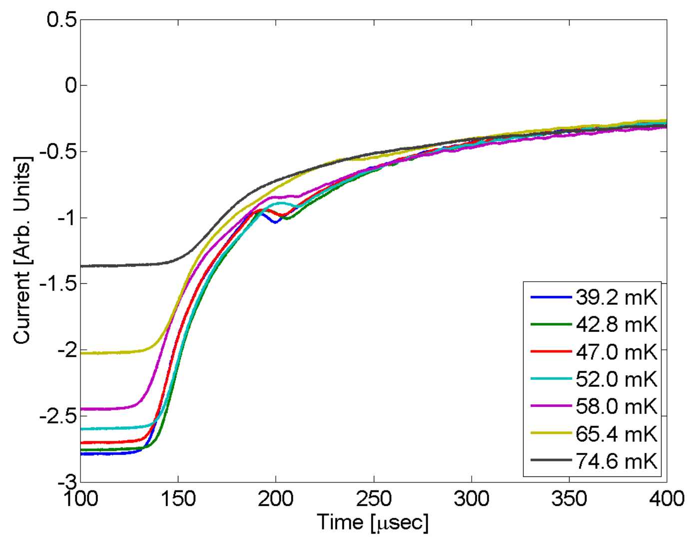

Figure B.14: Substrate temperature dependence, 1 kHz, channel 4. There seems to be a kink $\sim$50 μsec before the wiggle.

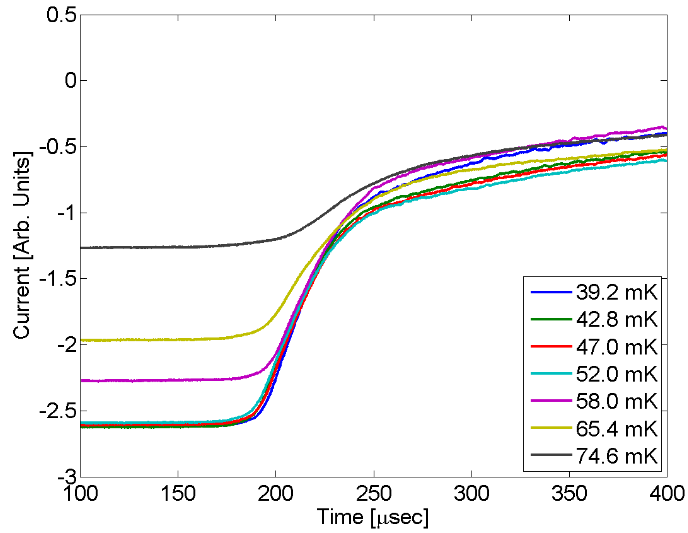

Figure B.15: Substrate temperature dependence, 100 Hz, channel 2.

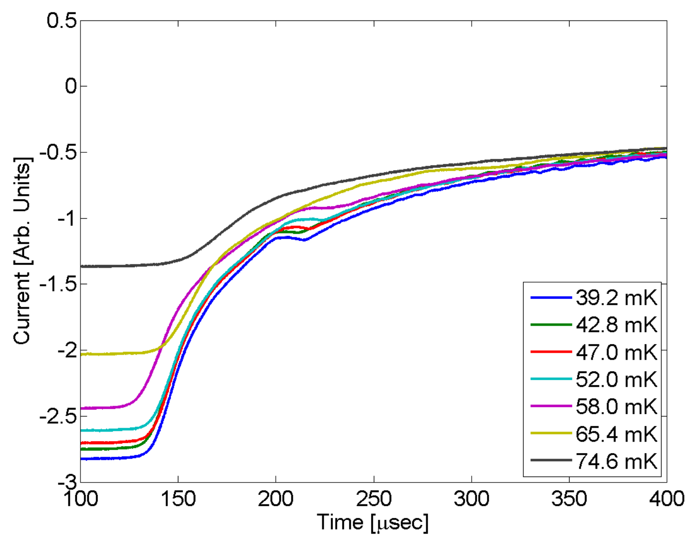

Figure B.16: Substrate temperature dependence, 100 Hz, channel 4. There is no noticeable change since the 1 kHz data set.

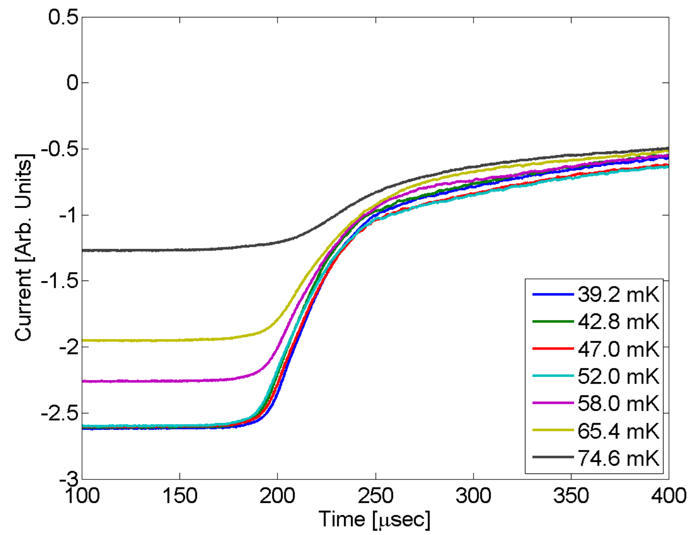

Figure B.17: Substrate temperature dependence, 10 Hz, channel 2.

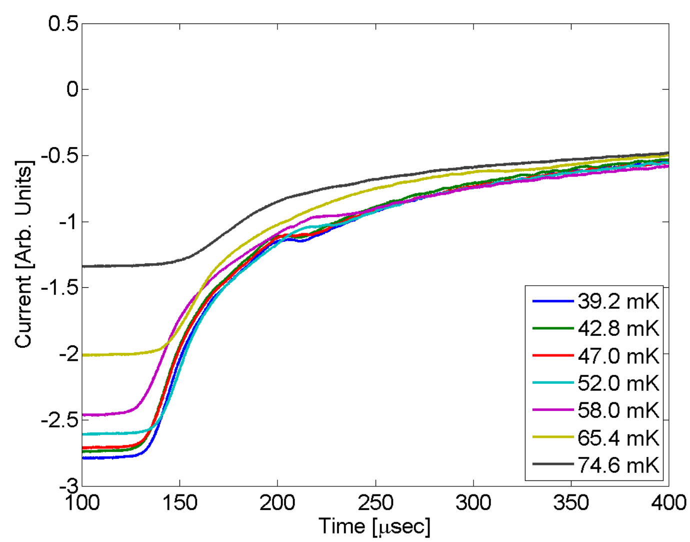

Figure B.18: Substrate temperature dependence, 10 Hz, channel 4. There is no noticeable change since the 1 kHz data set.

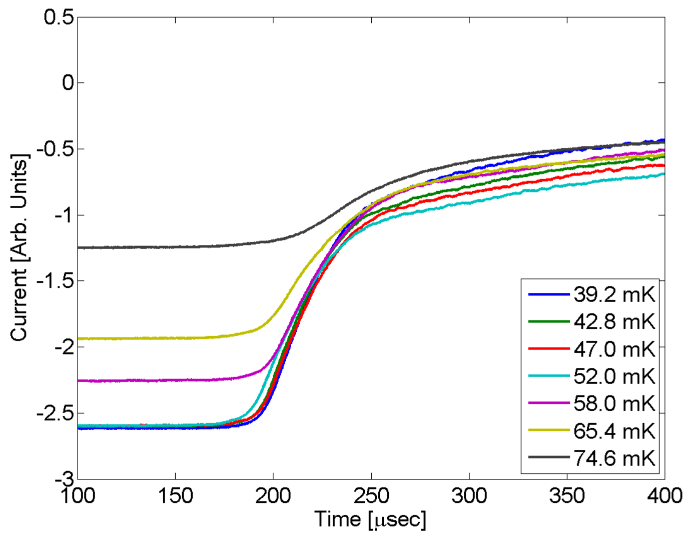

Figure B.19: Substrate temperature dependence, 1 Hz, channel 2.

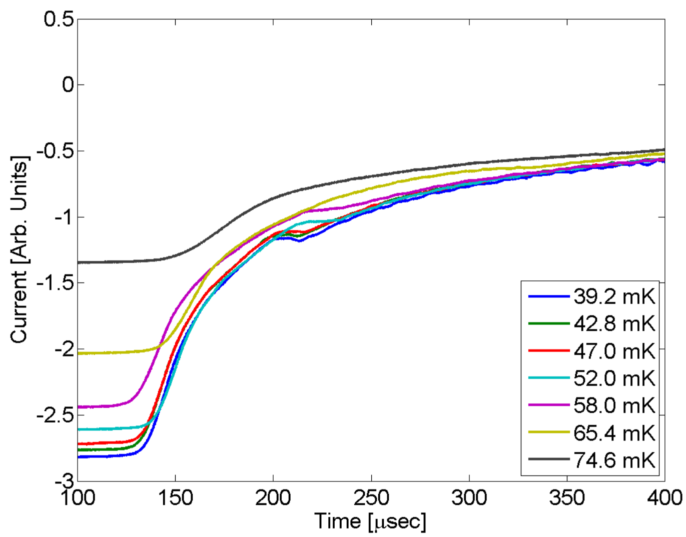

Figure B.20: Substrate temperature dependence, 1 Hz, channel 4. There is no noticeable change since the 1 kHz data set.

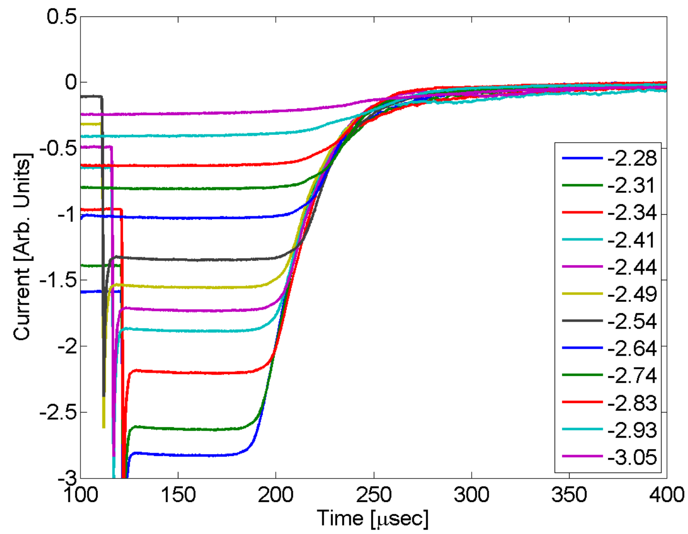

Figure B.21: Bias voltage dependence, channel 2, using 10 kHz heatpulses. The legend indicates the bias voltage. There is no obvious kink or wiggle seen.

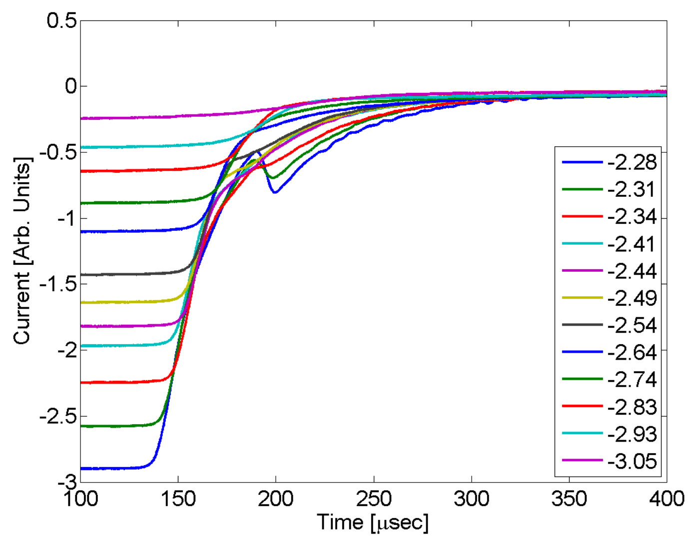

Figure B.22: Bias voltage dependence, channel 4, using 10 kHz heatpulses. The legend indicates the bias voltage. Kinks are seen at the lower bias voltages, but suppressed at the higher voltages.

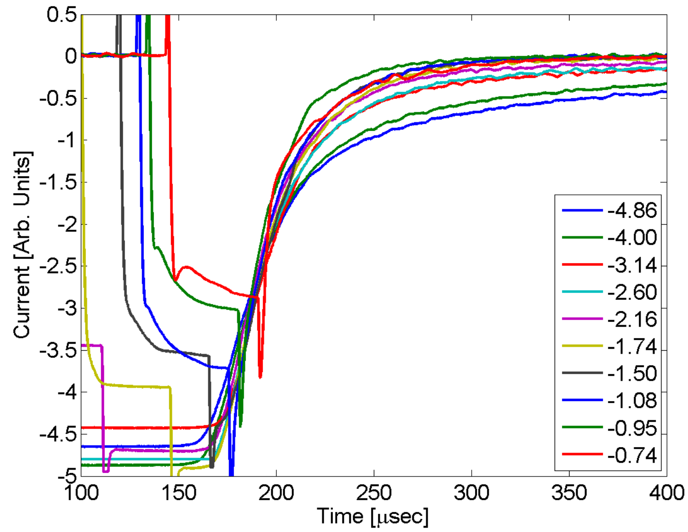

Figure B.23: Pulse amplitude dependence, channel 2, using 10 kHz heatpulses. The legend indicates the pulse voltage amplitude.

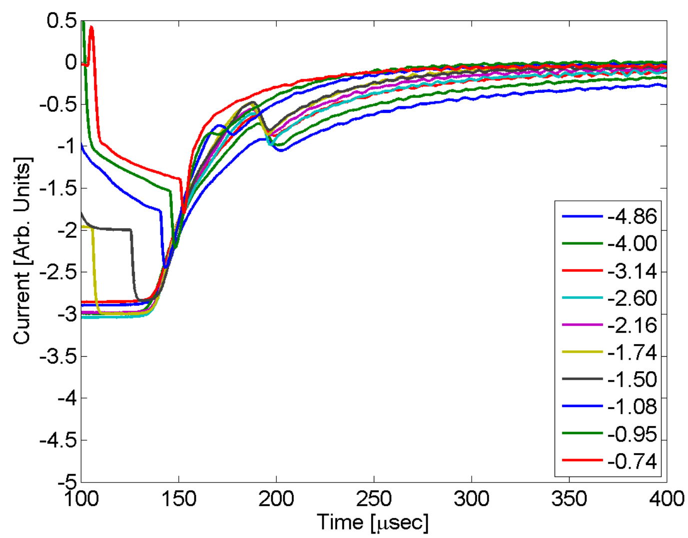

Figure B.24: Pulse amplitude dependence, channel 4, using 10 kHz heatpulses. The legend indicates the pulse voltage amplitude. This channel shows most clearly that a minimum heat pulse energy is necessary to observe the wiggles and that at higher energies they are suppressed. The longer decay time at higher energies again suggests that the substrate is being heated.

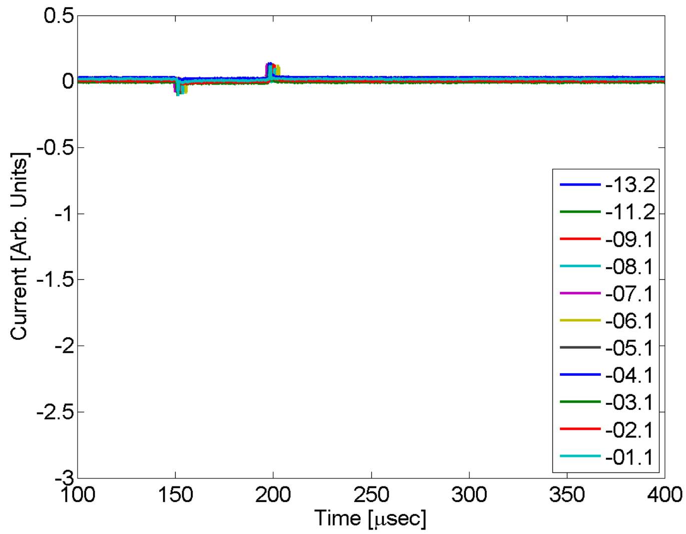

Figure B.25: Channel 2 was used to heat the substrate as its bias voltage was varied. The legend indicates the channel 2 bias voltage. Spikes can be seen when the heatpulse applied to channel 4 was turned on and off. Otherwise, no effect is seen.

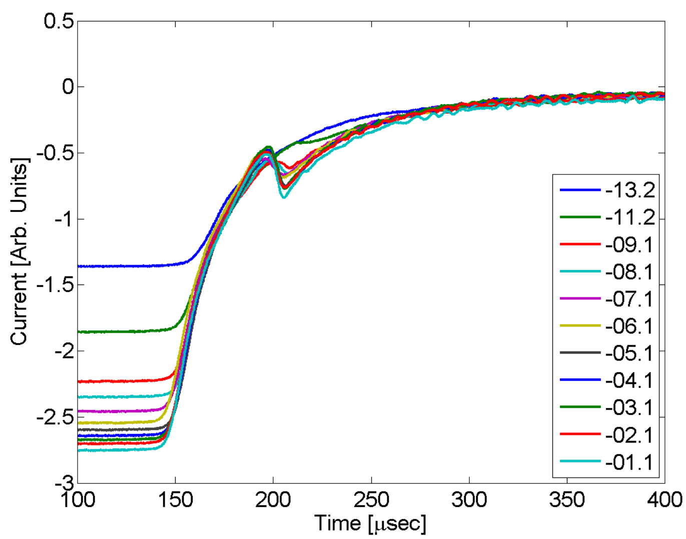

Figure B.26: Wiggles on are seen on channel 4. The legend indicates the channel 2 bias voltage. They are suppressed however when channel 2 is biased at large values.

B.2.9 Use Channel 2 to Heat Substrate. Vary Channel 4 Bias to Maximize Wiggle Height

We again vary the bias of channel 2 to vary the substrate temperature however, this time we also vary the bias on channel 4 to maximize the wiggle as described in Section B.6 (see Figures B.27 and B.28). No heat pulses were injected into channel 2. It is likely that the increase in substrate temperature from channel 2 is canceled out by the reduction in substrate temperature when the channel 4 bias is reduced. This conclusion is motivated by simulation which is discussed in Section B.3.4.

B.2.10 Data Conclusion

Purely electrical effects, either circuit resonances or crosstalk seem to be ruled out.

We notice that high substrate temperature suppresses the wiggle and also that more injected energy (seemingly also due to increased substrate temperature as discussed in Section B.2.1). So, we seek out some effect that can cause a wiggle or kink in traces and is suppressed at higher substrate temperature. One possibility is phase-separation in the TES. In some of the data, a combination of two kinks and or wiggles are seen, likely due to phase separation happening along both of the bias lines.

B.3 Simulations

The TES simulations discussed in Chapter 4 are invaluable in showing that phase-separation could be causing the wiggle / kink features seen in the X-ray and heatpulse data. Movies of the simulation can of course be created* and a picture of the ending state will be shown. In all of the 3-d plots, the x and y axis represent the physical

*For some time movies can easily be added to pdf files such as the electronic version of this thesis. Stanford University however requires that theses are submitted in paper format and with the exception of a flipbook, a movie would not be viewable. Why the technological constraints I don't know, perhaps I should just count my blessings that I don't have to inscribe my thesis into stone tablets before submitting.

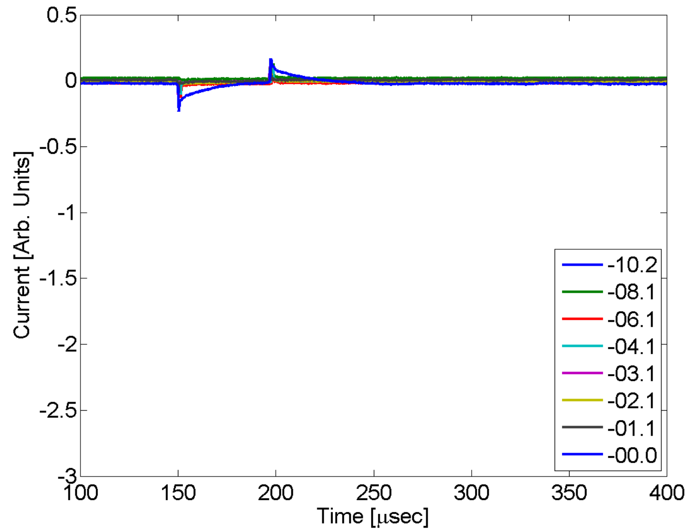

Figure B.27: Channel 2 was used to heat the substrate as its bias voltage was varied. The legend indicates the channel 2 bias voltage. Spikes can be seen when the heatpulse applied to channel 4 was turned on and off. Otherwise, no effect is seen.

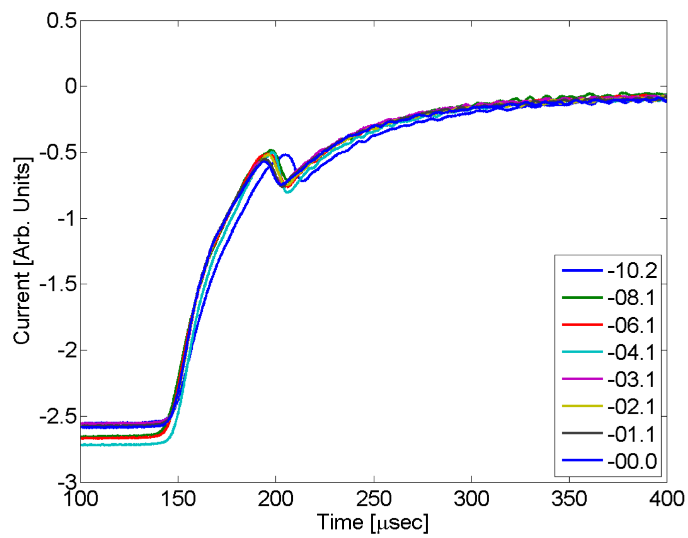

Figure B.28: Channel 4 bias varied to maximize wiggles. The legend indicates the channel 2 bias voltage. The channel 4 bias is however adjusted to maximize the wiggles. They are all recoverable.

extent of the TES. The z axis is then used to represent the resistance at a particular node.

B.3.1 Wiggle / Kink Equivalence

I have suggested before that the wiggle and kink features are manifestations of the same phase separation phenomenon. Indeed, both features show a transition between two decay times in the detector and both appear at a similar point in the trace's recovery.

To demonstrate this equivalence in simulation I setup a simulation where the TES is initially heated non-uniformly such that three strips adjacent to and parallel to the left bias line are slightly hotter than the remaining nodes. Their increase in temperature will be given by T_+ and will increase by one order of magnitude from $T_+ = 10^{-3}$ to 10 mK (see Figures B.29, B.30, B.31, B.32 and B.33). If the initial non-uniformity is small then phase separation will occur at a later time in the pulse recovery. Generally then, the transition from the two modes will be more dramatic and the wiggles more pronounced. In fact, it is very obvious that there are two different quiescent baseline currents for the two different modes. With larger non-uniformity, the TES quickly enters the phase-separated mode and a less dramatic wiggle is seen (see Figure B.33).

This section shows a connection between kinks and wiggles, but I certainly would not want to suggest that such strong non-uniformities are introduced into a real TES when it is heated. In fact, quite the opposite, heat pulses should heat the TES very uniformly. Instead, I would hypothesize that there are fabrication non-uniformities in the transition temperature, transition width and / or heat capacity that lead to regions that more weakly or strongly favor phase-separation.

B.3.2 Substrate Temperature Dependence

One of the nicest things about simulation is that the substrate temperature can be well known and held constant. When running experiments, heat injected into the TES can warm the substrate. In this section, I show simulations where the bias voltage

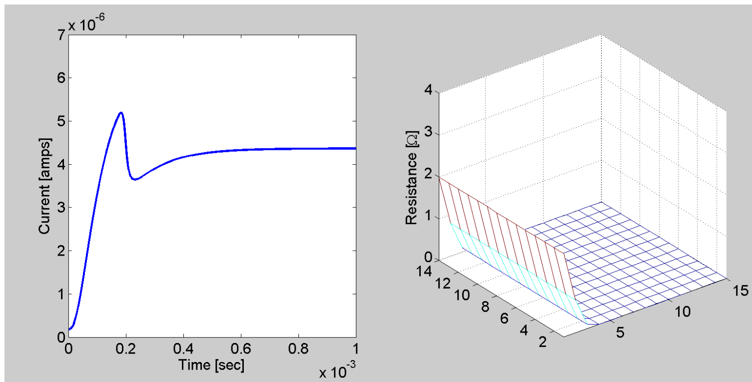

Figure B.29: The smallest non-uniformity $T_+ = 10^{-6}$ K is shown in this trace. The normal to phase-separated transition is quite dramatic as the TES is very cold before the transition. In fact, it is obvious that in the two different modes that there are two distinct baseline currents.

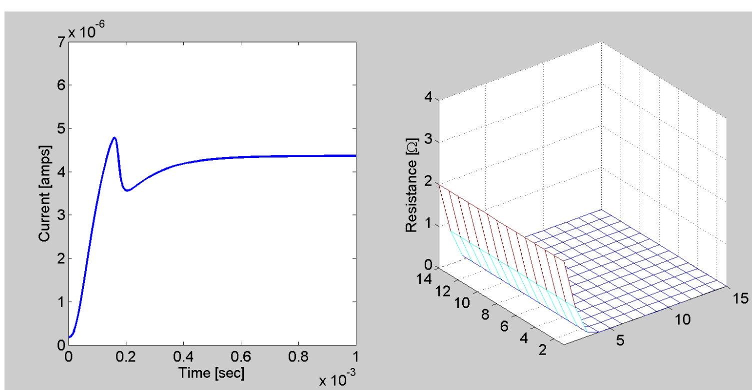

Figure B.30: The temperature non-uniformity is increased to $T_+ = 10^{-5}$ K. The normal to phase-separated transition is still quite dramatic.

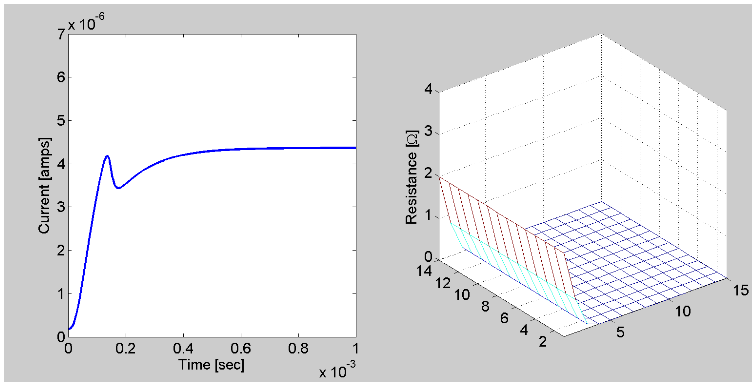

Figure B.31: The temperature non-uniformity is increased to $T_+ = 10^{-4}$ K. The normal to phase-separated transition is still quite dramatic.

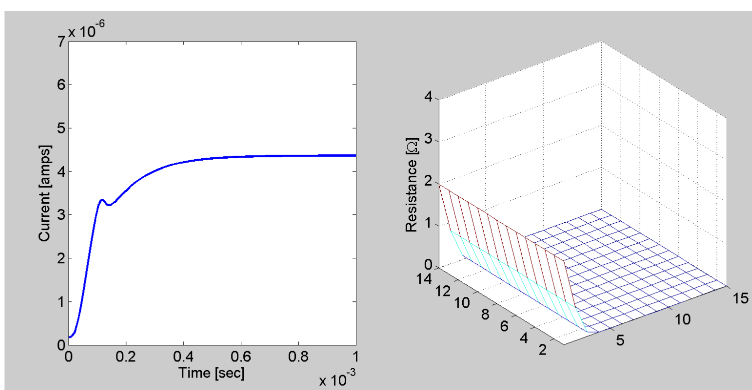

Figure B.32: The temperature non-uniformity is increased to $T_+ = 10^{-3}$ K. The normal to phase-separated transition now appears similar to that seen in the heatpulse traces.

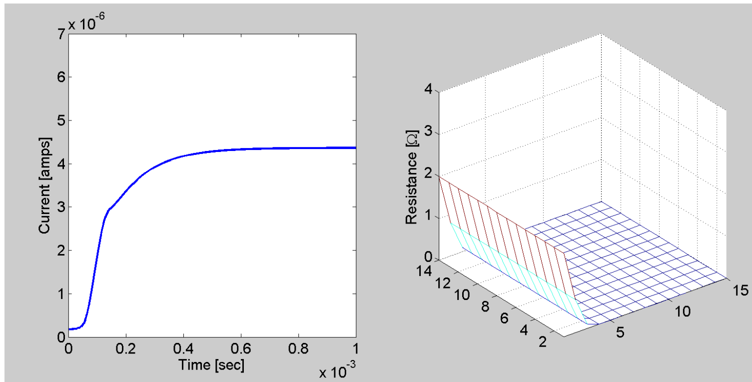

Figure B.33: The temperature non-uniformity is increased to $T_+ = 10^{-2}$ K. Very quickly in the recovery the TES is phase separated and a dramatic transition is suppressed. The normal to phase-separated transition now appears as a kink instead of a wiggle as seen in some of the heatpulse traces.

is held constant but the substrate temperature is increased towards $T_c = 87.5$ mK. I again apply a temperature non-uniformity such that nodes adjacent to one of the bias lines has an increased temperature $T_+ = 1$ mK which promotes phase-separation.

We notice that at high temperature (see Figure B.36) we suppress phase-separation in agreement with the results shown in Sections B.2.5 and B.2.8. The phase-separation is of course suppressed at even higher temperatures.

B.3.3 Bias Voltage Dependence

The data section shows a correlation between bias voltage dependence and the onset and suppression of wiggles / kinks. It is not clear however if this suppression is due to a change in the TES operating parameters such as α or a change in the substrate temperature T_{sub}. I am not sure that simulation is more revealing (see Figures B.37, B.38 and B.39). High bias voltage seem to mask the effects of phase separation and even high bias voltage can suppress the effect.

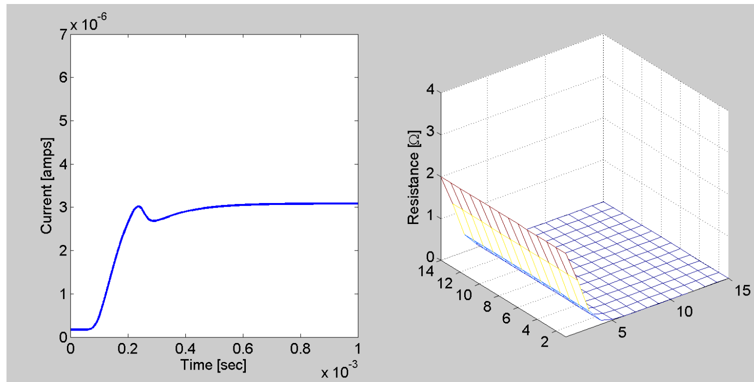

Figure B.34: Substrate Temperature Dependence. T_{sub} = 70 mK.

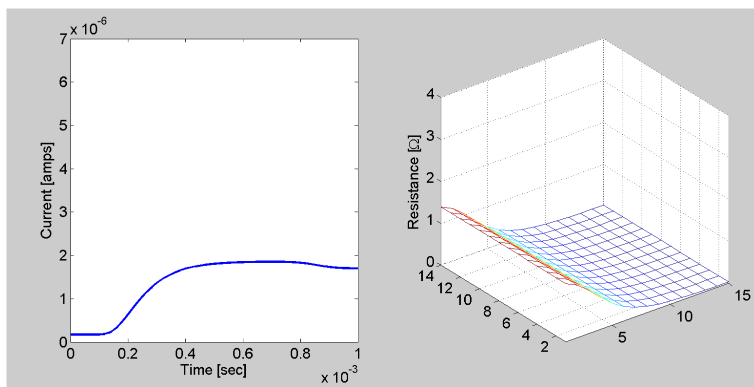

Figure B.35: Substrate Temperature Dependence. T_{sub} = 80 mK.

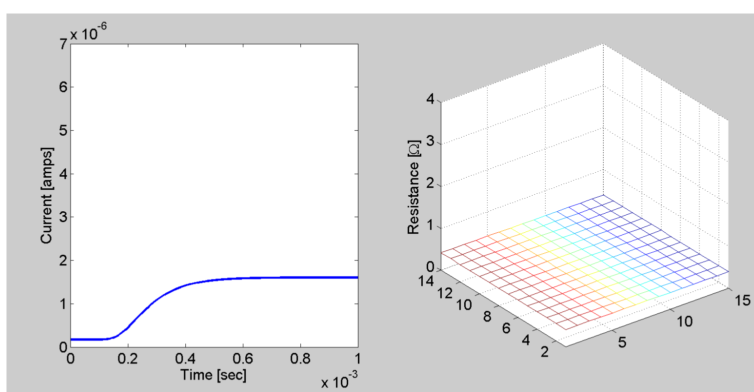

Figure B.36: Substrate Temperature Dependence. T_{sub} = 81 mK.

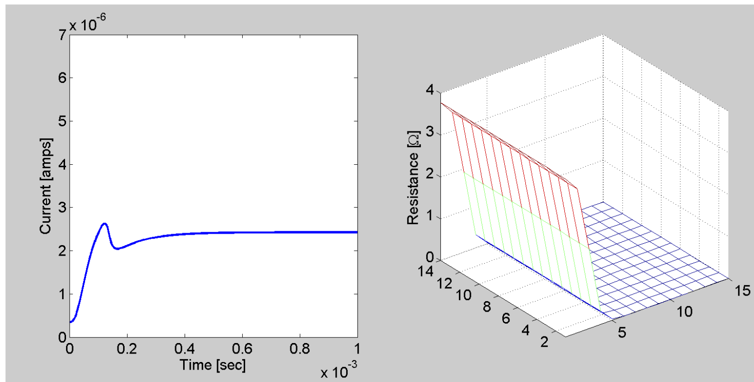

Figure B.37: Bias voltage dependence, V_{bias} = 480 mV. Phase separation is obvious at this biasing condition.

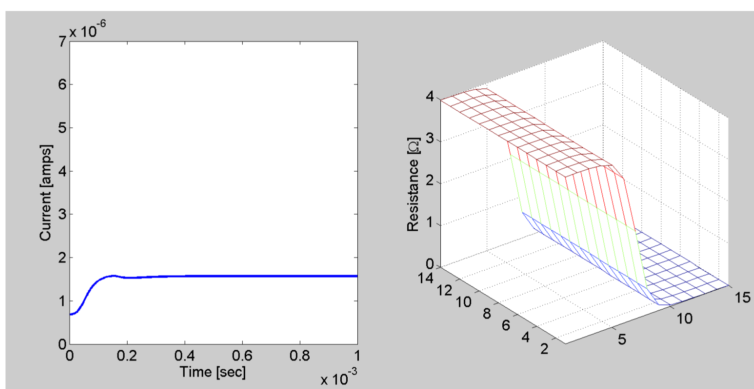

Figure B.38: Bias voltage dependence, V_{bias} = 960 mV. Phase separation occurs as is obvious in the resistance plot. However, the effect may not be obvious when looking at the pulse trace.

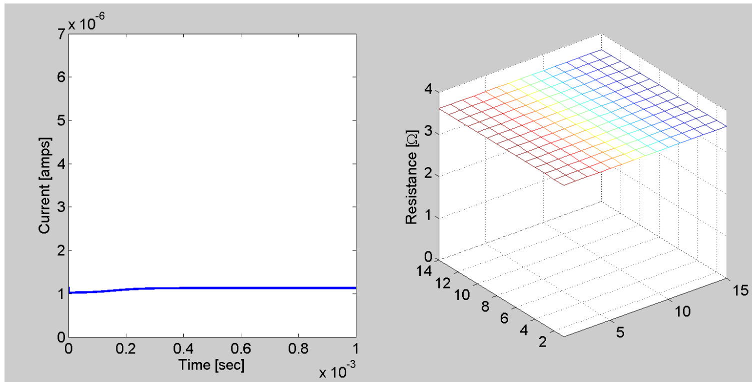

Figure B.39: Bias voltage dependence, $V_{bias} = 1440$ mV. Phase separation is only suppressed at the highest of bias conditions.

B.3.4 Raised Substrate Temperature, Vary Bias Voltage

Finally, raise the substrate temperature T_{sub} to 82 mK, quite near the 87.5 mK T_c and vary the bias voltage to try to recover wiggles as was done in Section B.2.9. Contrary to the results shown in that section, we are not able to recover the wiggles (see Figures B.40, B.41 and B.42). This observation suggests that our ability to recover the wiggles was due to effects on the substrate temperature. In Section B.2.9, lowering channel 4's bias voltage likely lowered the substrate temperature allowing phase separation to occur.

B.4 Theory

The relative strength of two competing thermodynamic effects determine if phase-separation occur in a TES. Thermal diffusion along the current flowing direction helps to keep both sides of the TES at the same temperature limiting the likelihood of phase-separation. On the other hand, Joule heating across the TES *always* tries to pull the TES into a phase separated state. To understand this effect, consider a square TES such that current moves from the left to right. The TES has some macroscopic resistance which leads to a constant current traveling across the TES. The Joule heating condition in this case is $P_J = I^2 R$ in which the phase-uniform

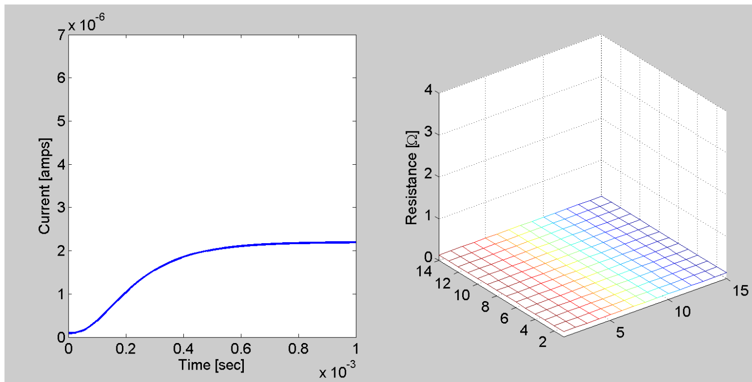

Figure B.40: Bias voltage dependence, V_{bias} = 120 mV. Phase separation is only suppressed at the highest of bias conditions.

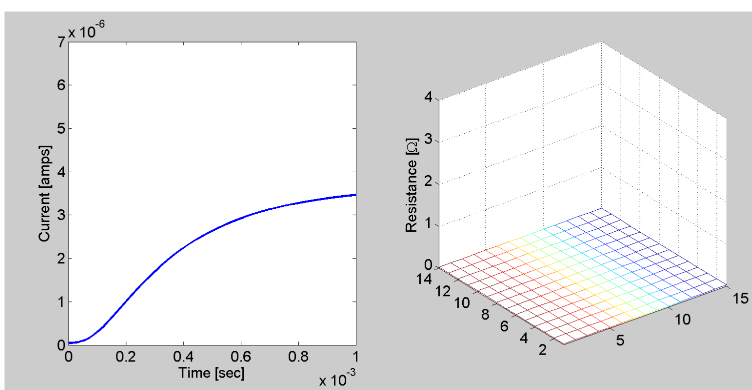

Figure B.41: Bias voltage dependence, V_{bias} = 60 mV. Phase separation is only suppressed at the highest of bias conditions.

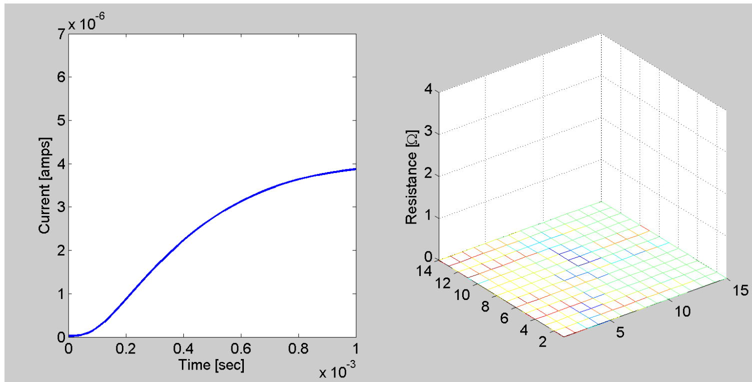

Figure B.42: Bias voltage dependence, $V_{bias} = 30$ mV. Phase separation is only suppressed at the highest of bias conditions.

state is thermodynamically unstable since the resistance R increases with T. This competition between thermal diffusion and Joule heating can be quantified and we find that for TESs longer than

$$l_{max}^2 = \frac{\pi^2 l_{Lor}}{\alpha \Sigma T_c^3 \rho_n} \; [23,\ 49] \tag{B.1}$$

(where, l_{Lor} is a material dependent constant and in tungsten $l_{Lor} = 25$ nWΩ/K^2,
α is defined in Equation 5.1,
Σ is defined in Equation 3.5,
T_c is of course the critical temperature and
ρ_n is the normal state resistivity)
phase separation is favored. One nice aspect of Equation B.1 is that material properties such as l_{Lor} and Σ are used instead of operating conditions like the bias current, temperature and resistance.

Finally, we need to explain the suppression of phase-separation at high temperature. One cooling mechanism that I neglected to describe earlier is cooling from the electron to phonon system (see Equation 3.5). When $T^n_{electron} \gg T^n_{phonon}$ then the cooling is described by Equation 5.2. However, at high substrate temperature, the substrate effectively warms the cold part of the TES reducing the likelihood of it collapsing into the superconducting state. With this effective heating, the phase uniform state is more stable. Obviously this is not a normal operating regime, but it does explain the data shown in this chapter.

B.5 Conclusion

Simulation suggests that the wiggles and kinks are manifestations of the same phase-separation phenomenon. In some of the data, a combination of two kinks and or wiggles are seen. This could perhaps be due to phase-separation occurring near each of the bias lines. It is likely that phase separation enhanced by microscopic variations in the critical temperature T_c. Furthermore, phase-separation seems to come and go from channels after the refrigerator is warmed and re-cooled. I suspect this change is due to cryo-deposits leading to a variation in heat capacity across the TES surface.

This phase-separation study was performed in two dimensions while previous studies in our group were restricted to one dimension. We notice that in two dimensions that phase separation is not suppressed along the current flow direction. It is however avoided in the direction perpendicular to current flow as current flows around localized hot spots in this case.

B.6 Data particulars

This section provides information on various bias voltages, pulse amplitudes, pulse durations and mixing chamber temperatures for the various heatpulse plots that were shown in this chapter.

Heatpulses on channel 3 and 4, varying pulse duration.			
Temperature mK	Bias mV	Heat pulse V	Burst size Hz
39.2	-430	-2.48	900,000
			100,000
			10,000
			1,000
			100
			10

Heatpulses on channel 3 and 4, varying pulse duration.			
Temperature mK	Bias mV	Heat pulse V	Burst size Hz
39.2	-430	-2.3	900,000
			100,000
			10,000
			1,000
			100
			10

Heatpulses on channel, reversed bias and pulse polarity.			
Temperature mK	Bias mV	Heat pulse V	Burst size Hz
39.2	380	2.22	900,000
			100,000
			10,000
			1,000
			100
			10
			1

Heatpulses on channel 3 and 4, 900 kHz pulse burst, varying substrate temperature (the same acquisitions are then repeated with 100 kHz, 10 kHz, 1 kHz, 100 Hz, 10Hz and 1 Hz burst widths).			
Temperature mK	Bias mV	Heat pulse V	Burst size Hz
39.2	-320	-2.3	900,000
42.8			
47			
52			
58			
65.4			
74.6			

Heatpulses on channel 2 and 4, varying bias voltage.			
Temperature mK	Bias mV	Heat pulse V	Burst size Hz
39.2	-420	-2.28	10,000
	-480	-2.31	
	-520	-2.34	
	-560	-2.41	
	-600	-2.44	
	-650	-2.49	
	-700	-2.54	
	-800	-2.64	
	-900	-2.74	
	-1000	-2.83	
	-1100	-2.93	
	-1200	-3.05	

Heatpulses on channel 2 and 4, varying pulse amplitude.			
Temperature mK	Bias mV	Heat pulse V	Burst size Hz
39.2	-360	-4.86	10,000
		-4	
		-3.14	
		-2.6	
		-2.16	
		-1.74	
		-1.5	
		-1.08	
		-0.95	
		-0.74	

Heatpulses on channel 4, vary bias on channel 2 to heat substrate.				
Temperature	Bias Ch 4	Heat pulse Ch 4	Bias Ch 2	Burst size
mK	V	V	mV	Hz
39.2	-400	-2.25	-13.2	10,000
			-11.2	
			-9.1	
			-8.1	
			-7.1	
			-6.1	
			-5.1	
			-4.1	
			-3.1	
			-2.1	
			-1.1	

Heatpulses on channel 4, vary bias on channel 2 to heat substrate, then re-bias channel 2 to retrieve and maximize the wiggle.				
Temperature	Bias Ch 4	Heat pulse Ch 4	Bias Ch 2	Burst size
mK	V	V	mV	Hz
39.2	-340	-2.2	-10.2	10,000
	-360	-2.2	-8.1	
	-390	-2.2	-6.1	
	-400	-2.2	-4.1	
	-410	-2.3	-3.1	
	-420	-2.3	-2.1	
	-420	-2.3	-1.1	
	-420	-2.3	0	

Appendix C

NI PCI-6115 DAQ Code

This code is for use in MATLAB. It requires that the NI PCI-6115 drivers are installed along with MATLAB's Data Acquisition Toolbox.

C.1 Trace Acquisition Manager

```
%
% TraceAcqMan.m
%
% Trace Acquisition Manager for NI PCI-6115
% by Steve Leman
%
% I allow a nice shutdown of the DAQ in case if it hangs up.
% Run me from MATLAB's command prompt.
%

try
    TraceAcq
catch
    disp('DAQ CONTROLLER FAILED ABNORMALLY!!!')
    lstErrr = lasterror;
```

```
    disp(lstErrr.message)
    disp(lstErrr.identifier)
    disp(lstErrr.stack)
    disp('Shutting down objects')
    disp(' ')
    stop(plotTimer)
    disp('Plot timer stopped')
    stop(ai)
    disp('DAQ stopped')
    delete(ai)
    disp('DAQ pointer deleted')
    disp(' ')
    disp('Shutdown complete')
end
```

C.2 Trace Acquisition

```
%
% TraceAcq.m
%
% Trace Acquisition Routine for NI PCI-6115
% by Steve Leman
%
% Saves data first in .bin format then converts to .mat after
% acquisition is complete. This speeds acquisition rate.
%
% This should be run from TraceAcqMan.m
%

clear
tic

% Set traces start number and number of traces to acquire
startEvent = 1;
eventTotal =  1000;
eventPerFile = 100;
fileTemp = 'f:\06-06-15\RawData\06-06-27';
fileFinal = 'f:\06-06-15\TraceData\06-06-27';

% Device operating parameters are stored in the
% acquisition files.
biasResistor = [7000 7000 7000 7000];
currentBias = -2/7000 * [1 1 1 4];
currentTESBaseLine = [-3.7E-6 -3.7E-6 -3.7E-6 -3.7E-6];
feedResistor = [1000 1000 1100 1000];
inductance = [250E-9 250E-9 250E-9 250E-9];
```

```
preTrigX = -preTrigger;
sRS = [100 100 100 100];
secPerPoint = 1/sampleRate;
shuntResistor =[0.02 0.02 0.02 0.005];


% First test for existing files to prevent overwritting.
disp('Testing for existing files.');

overwriteFlag = 0==1;
for fileTestNum = startEvent:eventPerFile:startEvent+eventTotal
    try
        load([fileFinal, '_', num2str(startEvent)]);
        overwriteFlag = 1==1;
        break
    catch
    end
end
if overwriteFlag
    beep
    disp(' ');
    disp('A file exists and will be OVERWRITTEN!!!')
    disp('Do you want to continue? Type "yes" to continue.')
    disp('Any other entry will terminate the program.')
    overwriteTest = input('','s');
    if ~strcmp('yes', overwriteTest)
        disp(' ')
        break
    end
end
disp(' ')
```

```
% Input ranges available
% -50 to +50 V
% -20 to +20 V
% -10 to +10 V
% -5 to +5 V
% -2 to +2 V
% -1 to +1 V
% -500 to +500 mV
% -200 to +200 mV
inRange = 5*[-1 1];

% Voltage at which hardware triggers
hardTrig = -1;

% Summed traces are used to cut small (or large) energy events
softTrigHigh = -100; % a large negative # allows many events
softTrigLow = 100; % a large positive # allows many events

% Set the number of points in the pretrigger
preTrigger = -2000;

% Set the channels to acquire from 0 - 3
chanIn = [0:3];
traces = length(chanIn);

% Set the trigger channel
trigChan = 1;

% Number of points in the acquisition.
sampleLength = 1E4;
```

```
% Acquisition time in seconds.
windowTime = 1E-3;

% Sampling rate in 1/sec. DAQ limited to 1e7 Hz.
sampleRate = min(sampleLength / windowTime,1E7);

% Pass operating parameters to NI PCI-6115
ai = analoginput('nidaq');
ch = addchannel(ai,chanIn);
set(ai,'SampleRate',sampleRate)
set(ai,'SamplesPerTrigger',sampleLength)
set(ai,'TriggerChannel',ch(trigChan))
set(ai,'TriggerType','Software')
set(ai,'TriggerCondition','Falling')
set(ai,'TriggerDelayUnits','Samples')
set(ai,'TriggerDelay', preTrigger)
set(ai,'TriggerConditionValue',hardTrig)
set(ai,'TriggerRepeat',eventPerFile)
set(ai,'Timeout',1)
set(ai.Channel,'InputRange', inRange)
set(ai,'DataMissedFcn',@DoNothing)
set(ai,'RuntimeErrorFcn',@DoNothing)

daqStatus = get(ai);

% Start DAQ before allocating memory
start(ai)

% Allocate MATLAB memory
data = zeros(eventPerFile,sampleLength,traces);
```

```
timeRelTrig = zeros(eventPerFile,1);
timeTrig = zeros(eventPerFile,6);
dataTemp = zeros(eventPerFile,sampleLength,traces);
timeRelTrigTemp = zeros(eventPerFile,sampleLength);
timeTrigTemp = zeros(eventPerFile,6);

% Set up and start plot timer which regularly updates display
event = 0;
eventsRec = 1;
plotHandle = figure(1);
plotTimer = timer('TimerFcn',@DataAcqPlot, 'ExecutionMode',...
    'fixedSpacing', 'Period', 3.0, 'UserData',...
    {squeeze(data(eventsRec,:,:)), event, inRange, plotHandle});
start(plotTimer);

%
% Acquire data
%
totalFiles = ceil(eventTotal / eventPerFile);
bufferedDataFlag = 0;
for fileNum = 1:totalFiles
    eventsRec = 0;
    while eventsRec < eventPerFile
        if bufferedDataFlag == 0;
            wait(ai,10);
            trigExec = get(ai,'TriggersExecuted');
            for eventInTrig = 1:trigExec
                wait(ai,10);
                try
                    [dataTemp(eventInTrig,:,:),...
                        timeRelTrigTemp(eventInTrig,:),...
```

```
                    timeTrigTemp(eventInTrig,:)] =...
                    getdata(ai);
            catch
                trigExec = trigExec - 1;
            end
        end
    wait(ai,10);
    start(ai)
    else
        trigExec = samplesSaved;
        bufferedDataFlag = 0;
    end

    % Sum traces and apply cuts
    for eventInTrig = 1:trigExec
        if eventsRec<eventPerFile
            [yMin, xMin] =...
                min(squeeze(dataTemp(eventInTrig,:,:)));
            avgX = round(mean(xMin));
            avgMin = sum(dataTemp(eventInTrig,avgX,:));
            if avgMin >= softTrigHigh & avgMin <=...
                    softTrigLow
                eventsRec = eventsRec + 1;
                data(eventsRec,:,:) = ...
                    squeeze(dataTemp(eventInTrig,:,:));
                timeRelTrig(eventsRec) = ...
                    timeRelTrigTemp(eventInTrig,1);
                timeTrig(eventsRec,:) = ...
                    timeTrigTemp(eventInTrig,:);
            end
        else
```

```
                samplesSaved = trigExec - eventInTrig + 1;
                dataTemp([1:samplesSaved],:,:) = ...
                    dataTemp([eventInTrig:trigExec],:,:);
                timeRelTrigTemp([1:samplesSaved],:) = ...
                    timeRelTrigTemp([eventInTrig:trigExec],:);
                timeTrigTemp([1:samplesSaved],:) = ...
                    timeTrigTemp([eventInTrig:trigExec],:);
                bufferedDataFlag = 1;
                break
            end
        end


        event = (fileNum-1)*eventPerFile + eventsRec;
        if event >= 1 & eventsRec>=1
            set(plotTimer,'UserData', ...
                {squeeze(data(eventsRec,:,:)), event, ...
                inRange, plotHandle});
        end
    end
    % Save data in .bin format
    fileName = [fileTemp, '_', ...
        num2str((fileNum-1)*eventPerFile+startEvent)];
    fid = fopen([fileName,'.bin'],'wb');
    fwrite(fid,data,'float32');
    fwrite(fid,timeRelTrig,'float32');
    fwrite(fid,timeTrig,'float32');
    fclose(fid);

    disp(['Saved file... ',fileName, '.bin at time ', ...
        num2str(toc)])
```

```
end

% Acquisition complete. Shutdown DAQ and notify user.
stop(plotTimer)
stop(ai)
delete(ai)
%
disp('Stopped DAQ.')
disp('Stopped plot timer.')
setpref('Internet','SMTP_Server','smtp.stanford.edu');
setpref('Internet','E_mail','Data@Acq');
mailMessage = ['Data Acquisition Complete ', ...
    num2str(startEvent), ' - ', ...
    num2str(startEvent + eventTotal)];
sendmail('swleman@stanford.edu',mailMessage,mailMessage)
sendmail('6503845209@mmode.com',mailMessage,mailMessage)
disp('Sent "DAQ Complete" email.')
%
wavData = 100*wavread('ringout')';
wavplay(wavData, 11025)
wavplay(wavData, 2 * 11025)
wavplay(wavData, 11025 / 2)
wavplay(wavData, 11025)
wavplay(wavData, 2 * 11025)
wavplay(wavData, 11025 / 2)
wavplay(wavData, 11025)
wavplay(wavData, 2 * 11025)
wavplay(wavData, 11025 / 2)

% Convert files to .mat format and delete old .bin files
disp('Begin converting file types.')
```

```
for fileNum = 1:totalFiles
    fileNameLoad = [fileTemp, '_', ...
        num2str((fileNum-1)*eventPerFile+startEvent)];
    fid = fopen([fileNameLoad,'.bin'],'rb');
    [dataMatrix,count] = ...
        fread(fid,traces*sampleLength*eventPerFile,'float32');
    timeRelTrig = fread(fid,eventPerFile,'float32');
    timeTrig = fread(fid,6*eventPerFile,'float32');
    fclose(fid);

    data = ...
        reshape(dataMatrix,[eventPerFile,sampleLength,traces]);
    timeTrig = reshape(timeTrig,[eventPerFile,6]);

    fileNameSave = [fileFinal, '_', ...
        num2str((fileNum-1)*eventPerFile+startEvent)];
    save(fileNameSave, 'data', 'timeRelTrig', 'timeTrig', ...
        'biasResistor', 'currentBias', 'currentTESBaseLine',...
        'feedResistor', 'inductance', 'preTrigX', 'sRS',...
        'secPerPoint', 'shuntResistor');
    system(['del ', fileNameLoad, '.bin']);

    disp(['Saved file... ',fileNameSave, ' at time ', ...
        num2str(toc)])
end

% Notify user that all is good and well.
setpref('Internet','SMTP_Server','smtp.stanford.edu');
setpref('Internet','E_mail','Data@Acq');
mailMessage = ['File Conversion Complete ', ...
    num2str(startEvent), ' - ', ...
```

```
    num2str(startEvent + eventTotal)];
sendmail('swleman@stanford.edu',mailMessage,mailMessage)
sendmail('6503845209@mmode.com',mailMessage,mailMessage)
disp('Sent "File Conversion Complete" email.')
disp('Done.')
wavplay(wavData, 11025)
wavplay(wavData, 2 * 11025)
wavplay(wavData, 11025 / 2)
```

C.3 Do Nothing Function

Yes, this really is necessary.

```
function [] = DoNothing(varargin)

%
% DoNothing.m
%
% A dummy function for for NI PCI-6115
% by Steve Leman
%
```

C.4 Data Acquisition Figure Updater

```
function DataAcqPlot(varargin);

%
% DataAcqPlot.m
%
% Data Acquisition Plotter for NI PCI-6115
% by Steve Leman
%
% Updates MATLAB figure
%

sentData = varargin{1}.UserData;
plotHandle = sentData{4};

set(0, 'CurrentFigure', plotHandle)

plot(sentData{1})
ylim(sentData{3})
title(['Event ', num2str(sentData{2})]);
drawnow
```

Bibliography

[1] R. Cen and J. P. Ostriker, "Where Are the Baryons?," *The Astrophysical Journal* **514**, pp. 1–6, Mar. 1999.

[2] M. Fukugita, C. J. Hogan, and P. J. E. Peebles, "The Cosmic Baryon Budget," *The Astrophysical Journal* **503**, pp. 518–530, Aug. 1998.

[3] D. N. Spergel, R. Bean, O. Dore', M. R. Nolta, C. L. Bennett, G. Hinshaw, N. Jarosik, E. Komatsu, L. Page, H. V. Peiris, L. Verde, C. Barnes, M. Halpern, R. S. Hill, A. Kogut, M. Limon, S. S. Meyer, N. Odegard, G. S. Tucker, J. L. Weiland, E. Wollack, and E. L. Wright, "Wilkinson Microwave Anisotropy Probe (WMAP) Three Year Results: Implications for Cosmology," *ArXiv Astrophysics e-prints* , Mar. 2006.

[4] R. H. Pehl, F. S. Goulding, D. A. Landis, and M. Lenzling, "Accurate determination of the ionization energy in semiconductor detectors," *Nuclear Instruments and Methods* **59**(1), pp. 45–55, 1968.

[5] B. Cabrera, B. L. Dougherty, A. T. Lee, M. J. Penn, J. G. Pronko, and B. A. Young, "Prompt phonon signals from particle interactions in si crystals," *Journal of Low Temperature Physics* **93**(3-4).

[6] C. Kittel and H. Kroemer, *Thermal Physics*, W.H. Freeman and Company, 1980.

[7] N. W. Ashcroft and N. D. Mermin, *Solid State Physics*, Harcourt Collee Publishers, 1976.

[8] M. Tinkham, *Introdution to Superconductivity*, Krieger Publishing Company. see page 117.

[9] B. A. Young, T. Saab, B. Cabrera, A. J. Miller, P. L. Brink, and J. P. Castle, "Effect of implanted metal impurities on superconducting tungsten films," *Journal of Applied Physics* **91**(10), 2002.

[10] K. D. Irwin, "An application of electrothermal feedback for high resolution cryogenic particle detection," *Applied Physics Letters* **66**(15), 1995.

[11] A. J. Miller, *Development of a Broadband Optical Spectrophotometer using Superconducting Transition-Edge Sensors*. PhD thesis, Stanford Universiy, 2001.

[12] D. McCammon, W. Cui, M. Juda, J. Morgenthaler, J. Zhang, R. Kelley, S. Holt, G. Madejski, S. Moseley, and A. Szymkowiak, "Thermal calorimeters for high resolution X-ray spectroscopy," *Nuclear Instruments and Methods in Physics Research A* **326**, pp. 157–165, 1993.

[13] J. N. Ullom, W. B. Doriese, G. C. Hilton, J. A. Beall, S. Deiker, K. D. Irwin, C. D. Reintsema, L. R. Vale, and Y. Xu, "Suppression of excess noise in Transition-Edge Sensors using magnetic field and geometry," *Nuclear Instruments and Methods in Physics Research A* **520**, pp. 333–335, Mar. 2004.

[14] M. Galeazzi, F. Zuo, C. Chen, and E. Ursino, "Intrinsic noise sources in superconductors near the transition temperature," *Nuclear Instruments and Methods in Physics Research A* **520**, pp. 344–347, Mar. 2004.

[15] M. A. Lindeman, S. Bandler, R. P. Brekosky, J. A. Chervenak, E. Figueroa-Feliciano, F. M. Finkbeiner, T. Saab, and C. K. Stahle, "Characterization and reduction of noise in Mo/Au transition edge sensors," *Nuclear Instruments and Methods in Physics Research A* **520**, pp. 348–350, Mar. 2004.

[16] M. Bruijn, A. Germeau, H. Hoevers, P. de Korte, J. van der Kuur, and M. Ridder, "Steepness, noise and instabilities in ti/al transition edge thermometers," *Nuclear Instruments & Methods in Physics Research A* **559**, 2006.

[17] M. A. Lindeman, M. B. Anderson, S. R. Bandler, N. Bilgri, J. Chervenak, S. Gwynne Crowder, S. Fallows, E. Figueroa-Feliciano, F. Finkbeiner, N. Iyomoto, R. Kelley, C. A. Kilbourne, T. Lai, J. Man, D. McCammon, K. L. Nelms, F. S. Porter, L. E. Rocks, T. Saab, J. Sadleir, and G. Vidugiris, "Percolation model of excess electrical noise in transition-edge sensors," *Nuclear Instruments and Methods in Physics Research A* **559**, pp. 715–717, Apr. 2006.

[18] S. G. Crowder, M. A. Lindeman, M. B. Anderson, S. R. Bandler, N. Bilgri, M. P. Bruijn, J. Chervenak, E. Figueroa-Feliciano, F. Finkbeiner, A. Germeau, H. F. C. Hoevers, N. Iyomoto, R. Kelly, C. A. Kilbourne, T. Lai, J. Man, D. McCammon, K. L. Nelms, F. S. Porter, L. Rocks, T. Saab, J. Sadleir, and G. Vidugiris, "An investigation of excess noise in transition-edge sensors on a solid silicon substrate," *Nuclear Instruments and Methods in Physics Research A* **559**, pp. 721–723, Apr. 2006.

[19] B. Cabrera, "Design considerations for tes and qet sensors," *Nuclear Instruments & Methods in Physics Research, Section A* **444**(1-2), 2000.

[20] R. Welty and J. Martinis, "Two-stage integrated squid amplifier with series array output," *IEEE Transactions on Applied Superconductivity* **3**(1), 1993.

[21] M. J. Penn, *Nuclear-Recoil/Electron-Recoil Discrimination In Cryogenic Silicon Detectors For Use In Dark Matter Searches.* PhD thesis, Stanford Universiy, 1995.

[22] E. F. Feliciano, *Theory and Development of Position-Sensitive Quantum Calorimeters.* PhD thesis, Stanford Universiy, 2001.

[23] T. Saab, *Search for Weakly Interacting Massive Particles with the Cryogenic Dark Matter Search Experiment.* PhD thesis, Stanford Universiy, 2002.

[24] G. F. Knoll, *Radiation Detection and Measurement*, John Wiley and Sons, 1989.

[25] J. Sadlier, S. Bandler, R. Brekosky, J. Chervenak, E. Figueroa-Feliciano, F. Finkbeiner, N. Iyomoto, R. Kelley, C. Kilbourne, J. King, F. Porter, I. Robinson, T. Saab, and D. Talley, "Steepness, noise and instabilities in ti/al transition

edge thermometers," *Nuclear Instruments & Methods in Physics Research A* **559**, 2006.

[26] B. L. Dougherty, B. Cabrera, A. T. Lee, M. J. Penn, B. A. Young, and J. G. Pronko, "Charge-carrier collection by superconducting transition-edge sensors deposited on silicon," *Nuclear Instruments and Methods in Physics Research A* **333**, pp. 464–468, Sept. 1993.

[27] D. Abrams, D. S. Akerib, M. S. Armel-Funkhouser, L. Baudis, D. A. Bauer, A. Bolozdynya, P. L. Brink, R. Bunker, B. Cabrera, D. O. Caldwell, J. P. Castle, C. L. Chang, R. M. Clarke, M. B. Crisler, R. Dixon, D. Driscoll, S. Eichblatt, R. J. Gaitskell, S. R. Golwala, E. E. Haller, J. Hellmig, D. Holmgren, M. E. Huber, S. Kamat, A. Lu, V. Mandic, J. M. Martinis, P. Meunier, S. W. Nam, H. Nelson, T. A. Perera, M. C. Perillo Isaac, W. Rau, R. R. Ross, T. Saab, B. Sadoulet, J. Sander, R. W. Schnee, T. Shutt, A. Smith, A. H. Sonnenschein, A. L. Spadafora, G. Wang, S. Yellin, and B. A. Young, "Exclusion limits on the WIMP-nucleon cross section from the Cryogenic Dark Matter Search," *Physical Review D* **66**, p. 122003, Dec. 2002.

[28] Edited by Robert Hull, *Properties of Crystalline Silicon*, INSPEC, The Institution of Electrical Engineers, 1999.

[29] G. A. Northrop and J. P. Wolfe, "Ballistic phonon imaging in germanium," *Physical Review B* **22**, pp. 6196–6212, Dec. 1980.

[30] S. Tamura, J. A. Shields, and J. P. Wolfe, "Lattice dynamics and elastic phonon scattering in silicon," *Physical Review B* **44**, Aug. 1991.

[31] H. J. Maris and S. Tamura, "Anharmonic decay an the propagation of phonons in an isotropically pure crystal at low temperatures: Application to dark-matter detection," *Physical Review B* **47**, pp. 727–739, Jan. 1993.

[32] S. Tamura, "Monte Calro Calculations of Quasidiffusion in Silicon," *Journal of Low Temperature Physics* **93**, 1993.

[33] J. Maris, "Phonon propagation with isotope scattering and spontaneous anharmonic decay," *Physical Review B* **41**, May 1990.

[34] M. Msall, S. Tamura, S. Esipov, and J. Wolfe, "Quasidiffusion and the Localized Phonon Source in Photoexcited Si," *Physical Review Letters* **70**, May 1993.

[35] S. Tamura, "Quasidiffusive propagation of phonons in silicon: Monte Carlo calculations," *Physical Review B* **48**, Nov. 1993.

[36] S. ichiro Tamura, "Spontaneous decay rates of ta phonons," *Physical Review B* **31**(4), 1985.

[37] S. ichiro Tamura, "Spontaneous decay rates of la phonons in quasi-isotropic solids," *Physical Review B* **31**(4), 1985.

[38] Private correspondence between Blas Cabrera and Shin-ichiro Tamura.

[39] B. Cabrera, "Bolometric sensors for elementary particle detectors," *Nuclear Instruments & Methods in Physics Research A* **370**, 1996.

[40] W. H. Press, S. A. Teukolsky, W. T. Vetterling, and B. P. Flannery, *Numerical Recipes in C: The Art of Scientific Computing, Second Edition*, Cambridge University Press, 1992.

[41] K. Irwin, G.C.Hilton, D.A.Wollman, and J. M. Martinis, "Thermal-response time of superconducting transition-dege microcalorimeters," *Journal of Applied Physics* **83**(8), 1998.

[42] R. L. Burden and J. D. Faires, *Numerical Analysis*, Brooks / Cole Publishing Company, 1997.

[43] Private correspondence with Blas Cabrera.

[44] Private correspondence with Tarek Saab.

[45] M. Miller, *Passive Nondestructive Assay of Nuclear Materials*, ch. X-ray Fluorescence. Los Alamos National Laboratory, 1991.

[46] "http://www.csrri.iit.edu/periodic-table.html."

[47] U. Fano, "Ionization Yield of Radiations. II. The Fluctuations of the Number of Ions," *Physical Review* **72**, pp. 26–29, July 1947.

[48] B. G. Lowe, "Measurements of Fano factors in silicon and germanium in the low-energy X-ray region," *Nuclear Instruments and Methods in Physics Research A* **399**, pp. 354–364, 1997.

[49] S. W. Nam, *Development of Phonon-Mediated Cryogenic Particle Detectors with Electron and Nuclear Recoil Discrimination*. PhD thesis, Stanford Universiy, 1998.